Developing Electroconductive Microcarriers for Cell Manufacturing

by

Aynaz Saket Balgouri

A Thesis Submitted in Partial Fulfillment

Of the Requirements for the Degree of

Master of Applied Science

In the Department of Mechanical Engineering

University of Victoria

Supervisory Committee

Developing Electroconductive Microcarriers for Cell Manufacturing

by

Aynaz Saket Balgouri

Supervisory Committee

Dr. Mohsen Akbari, Mechanical Engineering
Supervisor

Dr. Sravya Tekumalla, Mechanical Engineering
Departmental Member

Abstract

The development of electroconductive biomaterials is critical for engineering functional tissues, particularly those composed of electrically excitable cells such as skeletal muscle, cardiac, and neural tissues. Traditional hydrogels often lack electrical conductivity, limiting their ability to support key physiological processes such as cell proliferation, alignment, and differentiation. This thesis presents the design, fabrication, and biological evaluation of novel electroconductive microcarriers based on gelatin methacryloyl (GelMA), integrated with either choline-based bio-ionic liquids (BILs) or poly(3,4-ethylenedioxythiophene):polystyrene sulfonate (PEDOT:PSS), providing ionic and electronic conductivity, respectively.

Microfluidic flow focusing was employed to fabricate monodisperse microcarriers with controlled size and tunable composition. Material characterization demonstrated that increasing the concentration of either BIL or PEDOT:PSS significantly enhanced the electrical conductivity of the hydrogels. Specifically, conductivity measurements showed a maximum of 0.663 S/m for GelMA hydrogels containing 5% BIL (GB-7-5), and 0.90 S/m at 1 mA and 3.63 S/m at 10 mA for hydrogels containing 2% PEDOT:PSS (GP-7-2), confirming improved conductive performance with higher additive content.

Biological assays using C2C12 murine myoblasts demonstrated that both conductive microcarrier types promoted significantly better cell adhesion and proliferation compared to non-conductive controls. Live/dead, trypan blue/PrestoBlue staining confirmed high viability (>85%) across all formulations. Immunofluorescence imaging revealed elongated nuclei in conductive groups, especially in high-conductivity formulations. Flow cytometry further showed enhanced Myosin Heavy Chain (MyHC) expression, indicating improved myogenic differentiation, with up to a 1.5-fold increase observed in conductive groups.

Overall, this thesis demonstrates that combining ionic and electronic conductive strategies with GelMA-based microcarriers offers a flexible, biocompatible, and functional platform for engineering electro-responsive tissues. To the best of our knowledge, this is the first report of monodisperse electroconductive microcarriers fabricated from GelMA-based conductive microgels- using both an ionic (GelMA-BIL) and an electronic (GelMA-PEDOT:PSS) strategy- produced via microfluidic flow-focusing. Beyond materials development, we systematically demonstrated that these microcarriers are biocompatible, support robust C2C12 adhesion and viability, and, crucially, *accelerate myogenic maturation* as evidenced by elongated nuclei and a ~1.5-fold rise in MyHC-positive cells. Taken together, the study establishes a scalable, dual-mode platform that bridges microcarrier bioprocessing with the electrical cues required for muscle-tissue engineering . The results lay the groundwork for future integration with dynamic electrical stimulation systems and suggest broad potential for applications in muscle regeneration, bioelectronic medicine, and cell manufacturing platforms.

Keywords: Electroconductive biomaterials, Gelatin Methacryloyl (GelMA), PEDOT:PSS, Bio-Ionic liquid, tissue engineering, microcarriers, myogenic differentiation, regenerative medicine.

Table of Contents

List of Tables

List of Figures

List of Abbreviations

Table 1 List of Abbreviations.

Abbreviation & Definition	Abbreviation & Definition
BIL – Bio-Ionic Liquid	C2C12 – Mouse Myoblast Cell Line
DMEM – Dulbecco's Modified Eagle Medium	DAPI – 4′,6-Diamidino-2-Phenylindole
EDC – 1-Ethyl-3-(3-Dimethylaminopropyl) Carbodiimide	EthD-1 – Ethidium Homodimer-1
FDA – Fluorescein Diacetate	FBS – Fetal Bovine Serum
GelMA – Gelatin Methacryloyl	LAP – Lithium Phenyl-2,4,6-Trimethylbenzoylphosphinate
MWCO- Molecular Weight Cut Off	PBS – Phosphate Buffered Saline
MyHC – Myosin Heavy Chain	PEDOT:PSS – Poly(3,4-ethylenedioxythiophene):Polystyrene Sulfonate
PDI – Polydispersity Index	
PFA – Paraformaldehyde	

Unit Abbreviation

Table 2 Unit Abbreviations.

Unit & Definition	Unit & Definition
μm – Micrometer	μL – Microliter
mm – Millimeter	S/m – Siemens per Meter
mL – Milliliter	rpm – Revolutions per Minute
mg – Milligram	mA – Milliampere
kDa – Kilodalton	
w/v – Weight per Volume	

Acknowledgments

We gratefully acknowledge the support of the Mathematics of Information Technology and Complex Systems (Mitacs), RepliCel Life Sciences, the Natural Sciences and Engineering Research Council of Canada (NSERC), the NSERC CREATE Training Program in 3D Printing Technology and Materials (3DPTM), Innovate BC (Ignite Award to MA), the Canada Foundation for Innovation (CFI), and the BC Knowledge Development Foundation.

I would also like to express my sincere thanks to Dr. Kristian Dubrawski and his PhD student, Ludwig Paul Cabling, for their assistance with the conductivity measurements using the HACH portable probe. Additionally, I am grateful to Dr. Sravya Tekumalla, her PhD student, Soumya Panda, Dr. Rustom Bhiladvala, and his PhD student, Md Yeashir Arafat, for their valuable support with the four-point probe measurement.

I would like to extend my gratitude to my supervisor and mentor, Dr. Mohsen Akbari, for his invaluable guidance and unwavering support throughout my time at LiME.

I am also thankful to my lab mate, Dr. Mahmood Razzaghi, for his patience and for teaching me the foundational lab skills. My sincere thanks go to Esfandyar Askari for generously sharing his knowledge and insights and for always being willing to answer my questions. I also appreciate the assistance of Hamed Alizadeh Sardroud and Mahdieh Shokrollahi Barough in the cell culture process.

Dedication

I dedicate this to my beloved husband, friend, and soulmate, Navid. Without his unwavering support and motivation, I could not have achieved this.

I also dedicate this to my dear parents, who have always supported me and encouraged me to pursue my goals and dreams.

1 Chapter 1: Introduction

1.1 Introduction: Research Objectives and Overview

This thesis focuses on the development and characterization of novel electroconductive microcarriers for muscle tissue engineering, designed to support the differentiation of electrically responsive cells such as skeletal muscle tissue, cardiac muscle tissue and neural tissue. A key goal is to address the limitations of conventional microcarrier systems, particularly their lack of electrical conductivity, which is crucial for mimicking the native environment of excitable tissues like skeletal muscle, cardiac tissue, and neural networks.

To introduce conductivity, two strategies were employed: ionic conductivity through choline-based bio-ionic liquids (BILs) and electronic conductivity using the conductive polymer PEDOT:PSS. These materials were integrated into a Gelatin Methacryloyl (GelMA) hydrogel matrix, chosen for its biocompatibility, tunable mechanical properties, and proven ability to support muscle cell behavior. To our knowledge, this is the first time such conductive hydrogels- combining BILs and PEDOT:PSS- have been fabricated as microgels using microfluidic techniques. BILs support low-voltage, ion-based signaling similar to natural physiological processes, while PEDOT:PSS provides stable electronic conductivity suitable for bioelectronic applications. The microcarriers were fabricated using microfluidic flow focusing technology, allowing precise control over size and shape, and ensuring monodispersity. This approach overcomes the inconsistencies of traditional batch methods and enables reproducibility, scalability, and tunable composition. Comprehensive characterization of the microcarriers included analysis of swelling behavior, size distribution, and conductivity to confirm their suitability for cell culture.

Biological evaluation involved culturing C2C12 murine myoblasts on both conductive and non-conductive microcarriers. Key factors such as cell viability, attachment, proliferation, and myogenic differentiation were assessed, with Myosin Heavy Chain (MyHC) expression used as a marker of muscle maturation. Results demonstrated how both ionic and electronic conductivity can influence muscle cell development and behavior.

In Chapter 1, we review the background literature on the advantages of microcarriers, the properties of electroconductive hydrogels, and the rationale behind selecting the specific materials used to fabricate the microcarriers. Chapter 2 focuses on the study of GelMA-BIL microcarriers, while Chapter 3 explores the microcarriers composed of GelMA-PEDOT:PSS. Finally, in Chapter 4, we present the conclusions of the study and discuss potential directions for future work.

1.2 Microcarriers in Cell Manufacturing

1.2.1 Role and Advantages of Microcarriers

Microcarriers are small, often spherical particles used as scaffolding platforms to support the growth of anchorage-dependent cells in suspension-based culture systems [3]. These scaffolds are vital for scaling up cell production, particularly in bioreactor-based systems where large quantities of cells are needed for therapeutic applications such as cell therapy, tissue engineering, and vaccine production [4]. Typically ranging in size from 50 to 400 μm, microcarriers offer a high surface-area-to-volume ratio, which facilitates robust cell attachment, proliferation, and differentiation within a compact culture volume [5-7]. Their efficiency in promoting cell expansion is largely attributed to their ability to mimic the in vivo extracellular matrix (ECM) environment, achieved through both physical structure and chemical composition. A wide variety of natural and synthetic materials are employed, including gelatin, collagen, alginate, dextran, chitosan, cellulose, and poly(lactic-co-glycolic acid) (PLGA) [5-8]. These materials influence surface chemistry, stiffness, porosity, and topography, which regulate cell adhesion, spreading, and behavior. Porous microcarriers, for example, enhance mass transport and cell-cell interactions, promoting 3D spheroid formation and tissue-like architecture [9-11].

Advanced fabrication techniques, particularly microfluidic technologies, have expanded the functional capabilities of microcarriers. These techniques allow for the generation of monodisperse microcarriers with tunable architectures and hierarchical features. Flow focusing and T-junction devices in droplet microfluidics produce particles with less than 2%-5% size variation, a vast improvement over the 20%-40% variation seen in traditional batch methods [12]. These systems can create porous or core-shell microcarriers that emulate native cell niches and support multicellular aggregation. Such designs are especially beneficial in stem cell culture, improving self-renewal and lineage-specific differentiation [9, 13, 14]. For instance, Wang et al. demonstrated the use of a capillary microfluidic system to produce porous microcarriers that promote 3D spheroid self-assembly, protect from shear stress, and enhance viability and physiological function [9].

Microcarrier-based culture systems also allow precise control over process parameters during scale-up in bioreactors. Unlike conventional two-dimensional flasks, microcarrier cultures can be integrated into stirred-tank or wave bioreactors for automated, space-efficient cell manufacturing [6, 15, 16]. Human mesenchymal stem cells (hMSCs) expanded on microcarriers in stirred bioreactors maintained high viability and differentiation potential, achieving clinically relevant cell numbers while preserving immunophenotype and potency [15, 17]. Uniform microcarriers enable precise monitoring and control of culture parameters such as pH, pO2, nutrient concentrations, and metabolite accumulation [18, 19]. This control is crucial for maintaining optimal conditions and minimizing variability across batches in industrial and therapeutic cell-based applications [15]. Consistent microenvironments enhance scalability and compliance, while variations in size and composition can significantly affect cell behavior, highlighting the need for controlled manufacturing [9, 20]. Real-time bioreactor monitoring systems rely on uniform microcarrier suspensions for effective feedback and process control [15, 18].

Despite these benefits, downstream processing of cells grown on microcarriers remains challenging, particularly for efficient cell harvesting without compromising quality. Traditional enzymatic detachment methods (e.g., trypsin) may damage cell surface proteins. To address this, thermo-responsive microcarriers using temperature-sensitive polymers like poly(N-isopropylacrylamide) (PNIPAM) have been developed. These undergo hydrophilic-to-hydrophobic transitions, enabling reversible cell attachment and enzyme-free detachment [21]. Dabiri et al. reported a thermo-responsive system (cytoGel) made from PNIPAM, GelMA, and PEGDA, achieving over 70% detachment efficiency at room temperature [21]. Biodegradable microcarriers provide an alternative by supporting cell expansion and enabling direct transplantation without cell separation. Materials like gelatin, collagen, and PLGA degrade in vivo, facilitating integration into host tissue [5, 7]. Handral et al. highlighted their relevance for allogeneic stem cell therapies requiring high yields, minimal variability, and simplified post-culture processing [7]. These biodegradable microcarriers eliminate the need for enzymatic or mechanical dissociation, thereby simplifying downstream processing and reducing the risk of cell damage during harvest [7, 17]. They also serve dual roles as growth substrates and delivery scaffolds in vivo [7].

Microcarriers are also explored for controlled delivery of bioactive compounds. By incorporating growth factors, cytokines, or drugs, they can release these agents in sustained or stimuli-responsive manners, modulating cell behavior during or after culture [13, 21]. For example, multifunctional microcarriers embedded with pro-chondrogenic factors have been used in cartilage tissue engineering for simultaneous cell expansion and differentiation [5]. In tissue engineering, microcarriers serve as cell-laden building blocks for 3D bioprinting, enabling the construction of complex structures with heterogeneous cell populations and ECM-like features. These bioinks enhance the mechanical integrity of constructs while maintaining cell viability [5, 7]. Cartilage tissue engineering, in particular, benefits from injectable scaffolds that combine encapsulation and delivery functions [5]. Emerging designs such as edible, thermo-responsive, porous, and ECM-mimetic microcarriers broaden their use in cultured meat and organoid development [7, 20, 22]. Microcarriers now play a foundational role in bridging cell manufacturing and therapeutic translation.

1.2.2 Limitations of Traditional Fabrication Methods

Traditional production methods like mechanical stirring, emulsification, and spray drying suffer from polydispersity and scale-up challenges due to heterogeneous shear forces [23, 24]. This variability affects encapsulation efficiency, nutrient diffusion, and degradation rates, as seen in studies noting poor batch consistency and adverse effects on cell environments [12]. Batch methods also hinder real-time monitoring and feedback control, critical for GMP-compliant production [23, 25].

1.3 Microfluidic Technologies for Microcarrier Fabrication

1.3.1 Advantages of Microfluidic Flow Focusing

Microfluidics overcomes these issues by enabling continuous, scalable, and controlled microcarrier synthesis. Mahmoudi et al. used a cross-junction system to fabricate alginate nanogels encapsulating TGF-β3 for cartilage regeneration, achieving high control over size and loading [24, 26]. Liu et al. reviewed microfluidic fabrication of non-spherical microparticles, demonstrating enhanced adhesion and proliferation [24]. The continuous nature of microfluidics supports integration with real-time monitoring and automation, ideal for industrial-scale manufacturing [27, 28]. Shao et al. encapsulated cells into double emulsion droplets for hydrogel-based microcarriers in 3D culture and drug screening [23].

1.3.2 Customization Though Flow Control

Customization is possible by altering channel geometry, flow regimes, or cross-linking chemistry to tune stiffness, degradation, and functionalization [13, 24]. Caldwell et al. engineered microgels with distinct mechanical and biochemical zones to support co-culture systems [13]. Multiple research teams [29-33], including our own [10, 21, 34], have effectively employed microfluidic flow focusing technology to generate microcarriers for a range of biomedical uses.

1.4 Electroconductive Biomaterials for Excitable Tissues

1.4.1 Physiological Role of Electrical Conductivity

Electroconductive biomaterials simulate the native electrical environment of excitable tissues like cardiac, skeletal muscle, and neural tissue. Conductive polymer hydrogels (CPHs), such as those based on PPy, PANI, and PEDOT, offer soft mechanics, high water content, and tunable conductivity for biomedical applications [35, 36]. Their reversible doping behavior enables dynamic electrical modulation at bio-interfaces [36]. Carbon-based nanomaterials (e.g., CNTs, graphene) provide high conductivity and mechanical strength, suitable for biosensing and tissue engineering [37]. For example, CNT-GelMA hydrogels aligned by dielectrophoresis improved gene expression and contractility in cardiac tissues [38]. Electrospun PANI/PLA nanofibers promoted synchronized cardiomyocyte beating in 3D bio-actuators [38].

1.4.2 Conductive Materials and Their Biological Impact

In skeletal muscle tissue engineering, conductive scaffolds enhance alignment and differentiation. Chen et al. used aligned PCL/PANi nanofibers to guide C2C12 myoblasts, improving fusion and maturation indices by 30% compared to controls. The PANi conductivity (~6.36 S/m) promoted electrical coupling and functional muscle fiber formation [39]. Electrical stimulation further enhances cardiomyocyte function, with 1 Hz pacing improving contractility and calcium handling [40]. Gold nanoparticle-incorporated hydrogels also improved viability and synchronous contraction in cardiac models and are adaptable to skeletal muscle [41, 42].

Electroconductive biomaterials promote cardiomyocyte alignment and maturation, improving synchronous contraction [43, 44]. A micropatterned PGS-AT film enhanced elongation and calcium transients in neonatal cardiomyocytes [44]. Dong et al. developed elastic PEGS-aniline pentamer films for skeletal muscle scaffolds, supporting C2C12 proliferation and myotube formation with optimal mechanical and electrical properties [45]. Injectable GT/rGO microcryogels improved stem cell differentiation and regeneration in VML models [46]. Nanofibrous scaffolds with PANI enhanced excitation-contraction coupling and contractility via calcium signaling [47]. Shape-memory polymers further supported myogenesis through mechanical and electrical mimicry [48].

Electroconductive substrates also support peripheral nerve regeneration. Wu et al. developed a conductive polyurethane with aniline pentamer that upregulated neurotrophic factor secretion and myelin gene expression in Schwann cells, enhancing neurite outgrowth [49]. CNT-incorporated PLA scaffolds supported olfactory ensheathing cell proliferation and adhesion [50]. Electroconductive microcarriers serve as active bio-interfaces in neural repair, enhancing neural stem cell differentiation on PEDOT-based scaffolds [47]. Graphene substrates improved action potential firing and synapse formation [51, 52]. Ma et al.'s CS/PDA microcarriers promoted axonal regeneration and functional recovery in a rat sciatic nerve model due to high porosity and conductivity [53].

In skeletal muscle, Dong et al.'s PEGS-aniline pentamer films and Zhang et al.'s GT/rGO microcryogels enhanced myotube maturation and regeneration post-VML injury [45, 46]. In cardiac tissue, Spearman et al. reported that PPy-PCL scaffolds improved calcium wave propagation, while Hua et al.'s PGS-AT elastomers promoted synchronized contraction and functional tissue formation [44, 54]. Electroactive scaffolds and microcarriers thus support cell adhesion, proliferation, and differentiation across excitable tissues, playing an active role in functional tissue regeneration.

1.5 Study Novelty and Research Gap

In this study, we report for the first time the fabrication of conductive microcarriers using two distinct types of conductive components: a choline-based bio-ionic liquid (BIL) and the conductive polymer poly(3,4-ethylenedioxythiophene):polystyrene sulfonate (PEDOT:PSS). The base matrix for both systems is gelatin methacryloyl (GelMA), a photo-crosslinkable derivative of gelatin that possesses excellent biocompatibility, natural cell-adhesive RGD motifs, and matrix metalloproteinase (MMP)-sensitive sequences, all of which support robust cell adhesion, remodeling, and differentiation [55-58]. GelMA's tunable stiffness, photo-crosslinkability, and high transparency also make it highly suitable for generating cell-laden, biomimetic structures via microfabrication [55]. These properties have made GelMA a gold standard for musculoskeletal tissue engineering and an ideal matrix for developing microcarriers [58].

The first conductive additive used was a choline-based bio-ionic liquid (BIL), introduced to impart ionic conductivity to the GelMA microcarriers. BILs can be chemically conjugated into GelMA hydrogels through photo-crosslinking, forming what is referred to as "BioGel," an ionically conductive, soft, injectable hydrogel that supports localized and programmable electrical signaling [2]. BioGels exhibit tunable mechanical and viscoelastic properties and maintain high biocompatibility in vitro and in vivo. Unlike traditional conductive fillers, BILs impart conductivity without adding particulate fillers, preserving the optical clarity, softness, and cell-compatibility of the hydrogel. This makes BILs particularly suitable for creating microcarriers intended for interfacing with soft, electrically active tissues such as muscle [2].

It is important to distinguish ionic conductivity from electrical (electronic) conductivity, as they operate through different mechanisms Electrical conductivity involves the flow of electrons through a material, as seen in metals or conductive polymers like PEDOT:PSS. Electrons hop between the localized sites of the PEDOT:PSS polymer and create electrical conductivity. In contrast, ionic conductivity is based on the movement of charged ions (such as Na^+, K^+, or Ca^{2+}) through hydrated polymer networks, similar to how signals propagate in biological tissues. The choline acrylate-based ionic liquid used in the microgels contains acrylate functional groups that co-polymerize with the methacryloyl groups of GelMA upon light exposure, forming a covalently crosslinked network. In this structure, the choline ion becomes covalently tethered to the GelMA matrix, serving as an immobile “anchor” of positive charge. Upon hydration, the BIL partially dissociates, releasing mobile counter-ions that enable ionic conduction throughout the hydrogel. The resulting matrix contains a mix of ions, including acrylate, bitartrate, and chloride from the BIL itself, as well as extracellular ions such as sodium and potassium from the surrounding cell culture media. In essence, ionic conductivity arises from the mobility of these counter-ions in association with the fixed choline acrylate moieties [2, 59]. In biological systems, ionic signaling plays a pivotal role. For example, during skeletal muscle contraction, an action potential triggers the release of Ca^{2+} from the sarcoplasmic reticulum into the cytosol, where it binds to troponin-C and initiates the cross-bridge cycling responsible for contraction [60, 61]. The intracellular cycling of Ca^{2+} ions- enabled by ion channels and pumps- is essential for contraction and relaxation and must be tightly regulated [62]. Therefore, integrating ionically conductive hydrogels into engineered microcarriers may enable materials to better mimic this physiological behavior and interface with electrically responsive tissues without the risks associated with high-voltage stimulation.

The second conductive component we selected was PEDOT:PSS, a conductive polymer widely studied in tissue engineering and bioelectronics. PEDOT:PSS is known for its high electronic conductivity (~20 S/cm in PBS and up to 40 S/cm in deionized water), excellent mechanical compliance (Young's modulus ~2 MPa), high stretchability (>35%), and superior thermal and electrochemical stability [63]. These properties enable PEDOT:PSS to function as a stable, long-lasting electrical interface within biological systems, where conventional metal electrodes or rigid polymers fail due to mechanical mismatch [63, 64]. In our context, we chose PEDOT:PSS for its ability to form hydrated, soft, and stretchable hydrogels compatible with cell-laden microstructures. PEDOT:PSS has also been shown to enhance neural stem cell differentiation, support long-term neuronal survival, and facilitate the formation of neuron-like morphologies when used as substrates [65]. Moreover, its efficacy in cardiac tissue engineering has been validated in vivo: a collagen-PEDOT:PSS injectable hydrogel was shown to suppress ventricular tachycardia and support hiPSC-cardiomyocyte function following myocardial infarction, restoring calcium handling and contractility [66].

Our decision to integrate both ionic and electronic conductive materials into GelMA-based microcarriers was driven by their complementary advantages and offering different applications based on the different nature of their conductivity. While PEDOT:PSS supports rapid electron-based conduction necessary for signal fidelity and cell stimulation, BILs enable safe, low-voltage ionic signaling compatible with soft tissue environments [2, 63, 67]. Together, they allow for the development of multifunctional microcarriers that are mechanically compliant, biologically interactive, and capable of participating in complex electrophysiological processes across tissue types-from skeletal muscle, where Ca^{2+}-driven contraction is key, to neural and cardiac tissues, where synchronized electrical communication is essential for function.

2 Chapter 2: Electroconductive GelMA-BIL Microcarriers for Skeletal Muscle Tissue Engineering

Note: Submission to a journal is in progress. Immunofluorescence imaging (Figure 13) was generated by Esfandyar Askari. Flow cytometry test and data analysis (Figure 15) was generated by Mahdieh Shokrollahi Barough. All other experiments and analysis were performed by the candidate.

2.1 Introduction

Microcarriers are scaffolding materials that are essential for scalable production of cells [5]. They provide a large surface area for cell attachment and proliferation [21], making them highly effective for expanding cell cultures in bioreactors [15, 17]. In addition to their capacity to support cell growth, microcarriers offer several other advantages, including ease of handling, the ability to control particle size and surface properties, and versatility in material composition [5, 10, 21]. Microcarriers' uniformity enables effective monitoring and regulation of factors like pH, oxygen levels (pO2), and concentrations of nutrients and metabolites. Enhanced control over these parameters results in more consistent cell cultures, which is essential for commercial cell-based applications [6, 9, 22]. Microcarriers can also be designed to be biodegradable, ensuring they do not interfere with downstream applications [7, 13]. Furthermore, their tunable mechanical and chemical properties enable the creation of environments that closely mimic native tissues, making them highly valuable in tissue engineering and regenerative medicine [18, 23].

Microcarriers have traditionally been produced using batch emulsion processes [68, 69]. However, these methods often suffer from limitations such as inconsistent particle size distribution, low production efficiency, and difficulty in scaling up [69]. In contrast, microfluidics offers a continuous, highly controllable production method that addresses many of these limitations [21]. The continuous nature of microfluidic production enables higher throughput, making the process more efficient and amenable to industrial-scale production [28, 70]. Moreover, using microfluidic devices, particularly flow focusing chips, allows for precise control over the size, shape, and monodispersity of microgels, overcoming the variability issues seen in traditional methods [24, 35]. This precision is achieved by manipulating fluid dynamics at the microscale, ensuring uniform particle formation and enhancing reproducibility [26, 71]. Microfluidic systems also offer flexibility in design, as properties can be easily altered by changing flow rates or channel geometries, allowing for rapid prototyping and customization of microgel properties [21]. Furthermore, microfluidics can facilitate the encapsulation of cells or biomolecules with high efficiency [25, 72], supporting their sustained release or providing a protective environment [27, 73].

Electroconductive biomaterials have emerged as promising candidates for enhancing cell processes, function, and maturity [74, 75]. Various conductive materials, including carbon-based nanoparticles [38, 76], gold nanoparticles [42, 43], and conductive polymers [36, 37], have been explored, each offering benefits like high conductivity but also facing challenges like cytotoxicity, cost, and stability [36-38, 42, 43, 76]. These materials facilitate the electrical stimulation of cells, which can promote cell proliferation [39, 40], differentiation [77, 78], and specific functional responses, in cardiac, neural tissue, and muscle tissue [39-41, 44, 49-51, 68, 77-84]. Studies in cardiac tissue engineering, for instance, have shown that substrates with conductive properties improve the alignment [85] and maturation [45] of cardiomyocytes, leading to more synchronized contractions [86] and enhanced tissue function. Muscle tissue engineering also benefits from electroconductive biomaterials, as these substrates promote the alignment [87] and fusion of myoblasts into mature myotubes [48], resulting in enhanced contractility and structural integrity of engineered muscle tissues [88]. Moreover, incorporating conductive scaffolds has been demonstrated to improve myogenic differentiation in skeletal muscle [47], and facilitating the formation of myotubes from C2C12 myoblast cells [46].

In the context of microcarriers, a few studies have demonstrated the feasibility of producing electroconductive microcarriers from chitosan/polydopamine [54] and poly-(3,4-ethylenedioxythiophene):polystyrene sulfonate (PEDOT:PSS) [67] and used them to grow neural cells, L929 mouse, and MRC-5 human fibroblasts. These studies have shown the cytocompatibility of such materials for cell culture applications [54, 67, 89].

Conductive scaffolds mimic the electrophysiological environment of the heart, enabling better integration and communication between cells [90], which is critical for the development of functional cardiac tissue. Similarly, in neural tissue engineering, electroconductive materials have been demonstrated to guide neurite outgrowth [91], and enhance the differentiation of neural stem cells into neurons [92, 93]. These conductive platforms facilitate electrical signaling [52, 53], which is essential for the formation of functional neural networks. Overall, the integration of electrical conductivity into biomaterials provides a dynamic platform that not only supports cell growth but also actively participates in the functional maturation of tissue constructs, making it a key consideration for advancing regenerative medicine.

This study introduces, for the first time, a soft electroconductive microcarrier made of gelatin methacryloyl (GelMA) and choline-based bio-ionic liquid (BIL). GelMA is biocompatible and has tunable mechanical properties that make it an ideal matrix for supporting myoblast adhesion, proliferation, and differentiation [55-58, 94-96]. BIL conjugated hydrogels exhibit a wide range of highly tunable physical properties, remarkable in vitro and in vivo biocompatibility, and high electrical conductivity without the need for additional conductive components [2, 97]. Employing microfluidic flow focusing, we have established a continuous production protocol for monodisperse GelMA-BIL microcarriers. Subsequently, we investigated the viability, proliferation, and differentiation of C2C12 myoblasts cultured on these conductive microgels. Our findings assessed the significant influence of electrical conductivity on cellular behavior and functionality, suggesting the potential of these microcarriers for enhancing myoblast culture and tissue engineering applications.

2.2 Experimental Section

2.2.1 Materials

A high-speed resin 3D printer (Photon Mono 2K, Anycubic, Shenzhen, China) was used to fabricate the 3D-printed microfluidic droplet generator. A clear photopolymer resin (Anycubic 405 nm UV-curing resin, Shenzhen, China) was used for the print. Essential chemicals and reagents were obtained from Sigma-Aldrich (St. Louis, MO, USA), including lithium phenyl-2,4,6-trimethyl benzoyl phosphinate (LAP) (CAS# 85073-19-4), Span 80 (CAS# 1338-43-8), porcine-derived gelatin Type A (CAS# 9000-70-8), phosphate-buffered saline (PBS) tablets, and methacrylic anhydride (CAS# 760-93-0). Additional biological materials, such as fetal bovine serum (FBS) (Cat#16000044), Dulbecco's Phosphate Buffered Saline (DPBS) (Cat#14190144), trypsin/EDTA (Cat#15400054), and Dulbecco's Modified Eagle Medium (DMEM) (Cat#11965118), were sourced from Gibco (Grand

Island, NY, USA). The Live/Dead viability and cytotoxicity kit for mammalian cells (Cat#L3224) was supplied by Invitrogen through ThermoFisher Scientific (Waltham, MA, USA). Furthermore, heavy mineral oil (Cat# 8042-47-5) was procured from Fisher Chemical (Waltham, MA, USA), while a dialysis membrane with a molecular weight cutoff (MWCO) of 12,000–14,000 was acquired from Fisher Scientific. Choline acrylate-based bio-ionic liquid (BIL) (Patent No. 11,605,508 B2) was provided by Noshadi et al. from the University of California, Riverside.

2.2.2 Synthesis of GelMA

GelMA was prepared according to a previously documented protocol [55]. To prepare GelMA, 10 g of porcine skin gelatin was dissolved in 200 mL of phosphate-buffered saline (PBS) at 60 °C, forming a 5% gelatin solution. Methacrylic anhydride (8 mL) was then gradually added dropwise while stirring at 300 rpm for 3 hours to achieve a high degree of methacrylation (DOM). To terminate the reaction, 300 mL of preheated PBS (40–50 °C) was introduced, followed by continuous stirring for 15 minutes.

The resulting GelMA solution was filtered and transferred into dialysis membranes with a molecular weight cutoff (MWCO) of 12–14 kDa. Dialysis was carried out at 40–50 °C for two weeks to remove unreacted methacrylic anhydride and other impurities. During this process, the membranes were immersed in distilled water, stirred at 50 rpm, and the water was replaced twice daily, with the membranes being reversed each time to ensure thorough purification. Finally, the purified GelMA solution was filtered once more and lyophilized to obtain the final solid GelMA product.

2.2.3 Design and High-Resolution Fabrication of the Microfluidic Chip Using 3D Printing

The microfluidic chip (channel dimensions 500 to 750 μm) was designed using SOLIDWORKS™ software (Version 2025 SP0. University of Victoria academic license. Waltham) and manufactured with a resin 3D printer (Photon Mono 2K, Anycubic, Shenzhen, China). The selection of 3D printing was driven by its exceptional precision and capability to create intricate microfluidic structures with high accuracy, ensuring consistent reproducibility and precise control over channel dimensions.

Prior to each printing cycle, both the printer and resin vat were meticulously inspected to remove any contaminants that could compromise print quality. Dust particles were eliminated using compressed air, while impurities in the resin vat were carefully extracted with a pipette.

After printing, the fabricated components underwent a thorough cleaning process with isopropanol to remove residual uncured resin, ensuring the structural integrity of the printed features. The cleaned components were then dried using compressed air and subjected to post-curing in a Kudo3D curing chamber for 30 minutes at room temperature, enhancing the microfluidic chip's mechanical and chemical stability.

2.2.4 Microcarrier Fabrication and Purification via Microfluidic Flow Focusing and Photo-Crosslinking

Microcarriers were generated using a microfluidic flow focusing systems as previously described [21, 34]. For droplet formation, heavy mineral oil containing 10% (w/v) Span-80, a non-ionic surfactant, was used as the continuous phase. Both the hydrogel (dispersed phase) and the continuous phase were loaded into plastic syringes and connected to the microfluidic device using Tygon tubing. The continuous phase was introduced via a 50 mL syringe, while the dispersed phase was delivered through a 3 mL syringe mounted on a syringe pump (Harvard Apparatus PHD 2000, USA). The flow rates for the continuous phase and the aqueous phase were 70 µL/min and 8 µL/min respectively.

Droplets were generated at the flow focusing junction of the microfluidic chip and subsequently passed through a crosslinking module, where exposure to visible light triggered in situ photo-crosslinking. This module was equipped with 20 standard 405 nm LEDs, ensuring effective crosslinking of the microcarriers as they moved through the system.

To eliminate residual oil and surfactants, the crosslinked microcarriers underwent purification through centrifugation, followed by sequential washing steps. The purification process involved two rinses with PBS containing 1% dish soap, two washes with a 50% ethanol/PBS solution, and three final rinses with PBS. The purified microcarriers were then either lyophilized and stored at 5 °C for future applications or immersed in cell culture medium for 72 hours before biological studies.

2.2.5 Microcarrier Size Analysis and Monodispersity Assessment

The formation of microcarriers was further analyzed by measuring their size using a Zeiss Axio Observer microscope (Germany). For this purpose, a drop of the microcarrier suspension was placed between two coverslips and observed under the microscope to capture bright field images. ImageJ software (version 1.54d, National Institutes of Health, USA) was used to determine the microcarrier sizes, enabling the assessment of how variations in flow rates affected the average size. The size distribution of the microgels was plotted with 10 μm intervals, and their monodispersity was quantified by calculating the polydispersity index (PDI) using Eq. 1, where σ represents the standard deviation of microgel sizes and D_m is the mean diameter of the microgels [21].

$$PDI = \frac{\sigma}{D_m} \tag{1}$$

2.2.6 Assessment of Swelling Behavior of Fabricated Microcarriers

To analyze the swelling behavior of the fabricated microcarriers, they were first lyophilized for 24 hours, and their average dry diameter was recorded. Subsequently, the microcarriers were immersed in cell culture media and incubated at 37 °C for 70 hours, during which their diameters were periodically measured. At designated time points, optical microscope images were captured, and the diameters were quantified using ImageJ software (version 1.54d, National Institutes of Health, USA).The swelling capacity was evaluated by calculating the ratio of the swollen diameter to the initial dry diameter, as defined in Eq. 2 [98].In this equation, D_0 represents the microcarrier's diameter in its dry state, while D_t denotes its diameter after swelling in the medium [98].

$$Swelling\ capacity\ (\%)\ = \left[\frac{D_t - D_0}{D_0}\right] \times 100 \tag{2}$$

The diameter of the microcarriers increases until it reaches D_{final}. This final diameter was used to calculate the swelling capacity percentage of each microcarrier group after 70 hours.

2.2.7 Conductivity Measurement of Hydrogel Solutions

The conductivity of the hydrogel solutions was measured using a HACH SL1000 portable parallel analyzer (No. 9430000, HACH, USA). To prevent unintended photo-crosslinking, all measurements were conducted under limited light conditions. The device was calibrated with a sodium chloride standard solution (Cat# 1440042, HACH, USA), and conductivity readings were recorded in mS/cm. For each measurement, 4 mL of the hydrogel solution was transferred into a 10 mL glass vial. The conductivity probe was then inserted into the solution, ensuring a stable reading before recording the final value.

2.2.8 Cell Culture and Seeding on Conductive Microcarriers

To assess the biocompatibility of conductive microcarriers, C2C12 murine skeletal muscle cells (American Type Culture Collection, Manassas, VA, USA) were cultured on the microcarriers under controlled conditions. The cells were maintained in complete growth medium composed of Dulbecco’s Modified Eagle Medium (DMEM) (Gibco), supplemented with 10% fetal bovine serum (FBS) (Gibco), 1% penicillin/streptomycin (Gibco), and 1% GlutaMAX (Gibco). Cultures were incubated at 37°C in a humidified environment with 5% CO_2, using passage 3 cells for all experiments.

Before cell seeding, sterile 96-well plates were coated with a 2% agarose solution (Fisher BioReagents) prepared in phosphate-buffered saline (PBS) under aseptic conditions. The coated plates were then incubated with DMEM at 37°C for 24 hours to optimize the surface for cell culture. Simultaneously, sterile microcarriers were pre-incubated in DMEM for 72 hours at 37°C to enhance their cell-adhesive properties. On the day of seeding, the DMEM was removed from the agarose-coated wells, and 100 μL of pre-incubated microcarriers were added to each well, ensuring even distribution. C2C12 cells were detached using 0.05% trypsin-EDTA (Gibco) for 5 minutes, counted, and seeded onto the microcarriers at a density of 40,000 cells per well. The plates were then incubated at 37°C with 5% CO_2 for 4 hours, with gentle agitation every 15-20 minutes to promote uniform cell attachment. Following this initial adhesion period, fresh culture medium was introduced into each well, and the cells were cultured on the microcarriers for seven days under standard incubation conditions.

2.2.9 Assessment of C2C12 Cell Viability on Conductive Microcarriers Using Live/Dead Fluorescence Staining

The viability of C2C12 cells cultured on conductive microcarriers was evaluated using the Viability/Cytotoxicity Kit for Mammalian Cells (L3224, ThermoFisher) in accordance with the manufacturer's instructions. This assay employs Calcein AM to label live cells and Ethidium homodimer-1 (EthD-1) to identify dead cells.

Before starting the assay, the stock solutions from the live/dead kit were retrieved from the freezer and allowed to equilibrate to room temperature in a dark environment to prevent photobleaching. A 4 µM EthD-1 working solution was prepared by diluting 20 µL of the 2 mM EthD-1 stock solution in 10 mL of sterile, tissue culture–grade DPBS, followed by vortexing to ensure thorough mixing. Next, 5 µL of the 4 mM Calcein AM stock solution was added to the EthD-1 solution, and the mixture was vortexed again for homogeneity.

The microcarriers were removed from the incubator, and the culture medium was aspirated. A 200 µL aliquot of the prepared live/dead staining solution was then added to the microcarriers, ensuring complete coverage. The samples were incubated for 2 hours at room temperature in the dark, allowing dye penetration while minimizing light-induced degradation. After incubation, the staining solution was removed, and the samples were washed by replacing it with DPBS to eliminate excess dye. Fluorescence imaging was conducted using a Zeiss Axio Observer microscope (Germany) to assess the viability of C2C12 cells on the conductive microcarriers. The prepared samples were then analyzed to determine cell viability.

2.2.10 Assessment of Cell Viability Using Trypan Blue Assay

To assess C2C12 cell viability, a trypan blue exclusion assay was performed using Trypan Blue Stain (Gibco, Cat# 15250061, Thermo Fisher Scientific) and a hemocytometer (Thermo Fisher Scientific). Cells cultured on microcarriers were detached using trypsinization. For each well of a 96-well plate, all microcarriers were removed and washed twice with PBS to eliminate residual media and non-adherent cells. Trypsin (0.05%) was added, and the samples were incubated at 37°C for 5-10 minutes to facilitate detachment. Once complete detachment was observed, cell culture media was then added to neutralize the trypsin. Then, the microcarriers were removed using cell sieves, ensuring that only the dissociated cells remained in suspension. After that, the suspension was centrifuged at 300 g for 5 minutes to pellet the cells. The collected cells were resuspended in fresh culture media, and an equal volume of trypan blue stain was added to the cell suspension. The stained cells were loaded into a hemocytometer, and both live (unstained) and dead (blue-stained) cells were counted under a Zeiss Axio Observer microscope (Germany). The percentage of viable cells was calculated using the following formula:

$$Cell\ viability\ (\%) = \left(\frac{Number\ of\ live\ cells}{Total\ number\ of\ cells\ (live + dead)}\right) \times 100 \qquad (3)$$

This method provided a quantitative measure of cell viability, ensuring accurate assessment of the impact of BIL-containing microcarriers on C2C12 cell health.

2.2.11 Assessment of Cell Attachment and Proliferation on Conductive Microcarriers

To assess the attachment efficiency of C2C12 cells on conductive microcarriers, four randomly selected wells were analyzed after 24 hours of incubation. The same procedure was performed as mentioned in section 2.2.10 to detach the cells and count the number of the cells in each well. The attachment percentages were calculated using Eq. 4:

$$Attachment\ (\%) = \left(\frac{Number\ of\ counted\ cells\ after\ 24\ hours}{Number\ of\ seeded\ cells}\right) \times 100 \qquad (4)$$

To evaluate cell proliferation on the microcarriers over time, 50,000 C2C12 cells were seeded onto the microcarriers in agarose-coated 96-well plates under static culture conditions. Cell attachment was quantified on days 1, 3, 5, and 7 using the same detachment and counting procedure described in section 2.10. This approach enabled the monitoring of cell proliferation dynamics on the conductive microcarriers throughout the seven-day culture period.

2.2.12 Immunofluorescence Staining and Morphological Analysis of C2C12 Cells on Conductive Microcarriers

Immunofluorescence staining was conducted to examine the cytoskeletal organization and nuclear morphology of C2C12 cells cultured on conductive microcarriers. F-actin filaments were visualized using fluorescently labeled phalloidin, while DAPI (4′,6-diamidino-2-phenylindole) was employed to stain cell nuclei.

To prepare the samples, microcarriers were washed twice with PBS before being fixed in 4% paraformaldehyde (VWR) at 4°C overnight. The next day, they were washed again with PBS and blocked with 5% (w/v) bovine serum albumin (BSA, VWR) in 0.3% Triton X-100 (BIO BASIC) dissolved in PBS, followed by overnight incubation at 4°C. After blocking, the solution was discarded, and the samples were incubated overnight at 4°C with 4 µg/mL Alexa Fluor™ 488 Phalloidin (Thermo Fisher Scientific) diluted in blocking buffer (1:5 dilution) to stain the actin cytoskeleton. Subsequently, the phalloidin solution was removed, and the samples were incubated with DAPI (4’,6-Diamidino-2-Phenylindole, Dihydrochloride, Thermo Fisher Scientific) for 30 minutes at room temperature in the dark to stain cell nuclei. Following two additional PBS washes, the microcarriers were transferred onto glass slides for fluorescence microscopy analysis to assess cell morphology.

During differentiation, C2C12 cells undergo morphological transitions, shifting from a rounded shape to an elongated, tubular structure as they adhere, elongate, and fuse into multinucleated myotubes [21, 34]. To quantify these morphological changes, ImageJ software (version 1.54d, National Institutes of Health, USA) was used for structural analysis. Nuclear elongation was evaluated by calculating the nuclear aspect ratio, defined as the ratio of the longest to shortest nuclear diameter. Nuclei from randomly selected images across experimental conditions were analyzed to quantify the extent of morphological transformation.

2.2.13 Flow Cytometric Analysis of MyHC Expression for Myogenic Differentiation Assessment

Flow cytometry was employed to analyze the expression of myosin heavy chain (MyHC), a key late-stage myogenic marker, to quantify the proportion of differentiated cells within the population. This technique enables precise single-cell protein expression analysis, providing an accurate assessment of differentiation status [99].

For sample preparation, cells were detached from the microcarriers by washing with PBS, followed by enzymatic dissociation using 0.5% trypsin-EDTA. The resulting cell suspension was passed through a 0.07 mm cell strainer to eliminate microcarrier remnants. Following the established protocol by manufacturer, the cell concentration was adjusted to 5000 cells/μL for subsequent staining. Cells were incubated for 30 minutes in PBS containing 2% BSA, along with a PE-conjugated anti-mouse MyHC antibody (MF20, BD-USA) and a FITC-conjugated anti-mouse MyoD antibody to label myogenic markers. After incubation, the stained cells were resuspended in 500 μL PBS and analyzed using an Attune NXT flow cytometer (Thermo Fisher, USA) to determine the proportion of MyHC+ cells and evaluate the extent of C2C12 differentiation [99]. Flow cytometry data analysis was done using FlowJo software (V X.0- BD USA).

2.2.14 Statistical Analysis

All experiments were conducted in at least three independent replicates, and results were presented as mean ± standard deviation (SD). Statistical analysis was performed using one-way ANOVA followed by Tukey’s multiple comparisons test in GraphPad Prism 7.0 (GraphPad Software, San Diego, CA, USA) to evaluate differences between groups.

Statistical significance was defined as follows: ns (not significant) for $p > 0.05$, * for $p < 0.05$, ** for $p < 0.01$, *** for $p < 0.001$, and **** for $p < 0.0001$. For the nuclei aspect ratio, the analysis was done using unpaired t test, with **** for $p < 0.0001$.

2.3 Results and discussion

2.3.1 Conductive Microcarrier Fabrication

A microfluidic emulsion system was utilized to generate monodisperse conductive microspheres. This method allows for the continuous production of uniformly sized microcarriers with precise control over their dimensions [21]. Unlike conventional emulsion polymerization, which requires post-processing steps such as sieving to achieve uniformity, this approach inherently ensures size consistency. By modulating the flow rate ratios, the microcarrier diameter can be finely tuned, and the formulation can be easily adjusted to achieve the desired material properties [10, 21]. The conductive hydrogel precursor solution comprised Gelatin Methacryloyl (GelMA) (7% w/v), Choline acrylate Bio-ionic Liquid (BIL) at concentrations of 2.5% and 5% w/v, and Lithium phenyl-2,4,6-trimethylbenzoylphosphinate (LAP) (0.3% w/v), serving as the dispersed phase (Figure 1). Detailed formulations and their respective codes are summarized in Table 3.

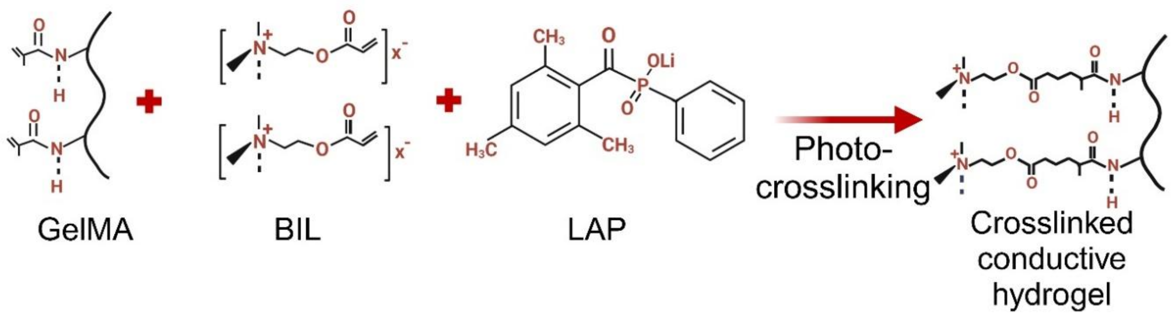

Figure 1 Schematic of photo-crosslinked electroconductive GelMA-BIL hydrogel formed by combining GelMA, BIL, and LAP under light exposure (reproduced with permission [57]).

Table 3 The details of the microgels compositions and their corresponding codes.

BIL concentration (w/v%)	Code
0	GB-7-0
2.5	GB-7-2.5
5	GB-7-5

GelMA forms a biocompatible hydrogel matrix, while BIL contributes ionic conductivity, and LAP functions as a photoinitiator, facilitating the photo-crosslinking of the hydrogel solution. LAP is a water-soluble, cytocompatible Type I photoinitiator commonly employed in the polymerization of hydrogels and other biomaterials for biomedical applications. It is favored over alternatives like Irgacure 2959 due to its superior properties, including higher water solubility, faster polymerization kinetics under 365 nm light, and absorption at 400 nm, which enables polymerization using visible light. These advantages allow for efficient cell encapsulation at lower initiator concentrations and longer wavelengths, minimizing cytotoxicity and enhancing cell viability [100]. A constant concentration of GelMA (7% w/v) and LAP (0.3% w/v), along with varying concentrations of BIL (2.5% and 5% w/v), were dispersed in distilled water as the dispersed phase. This mixture was injected into a solution of mineral oil with Span 80 (continuous phase) to produce the microcarriers (See Figure 2). The experimental section provides a detailed description of the microcarrier fabrication process. Figure 2(i) illustrates the microfluidic setup used for microcarrier production.

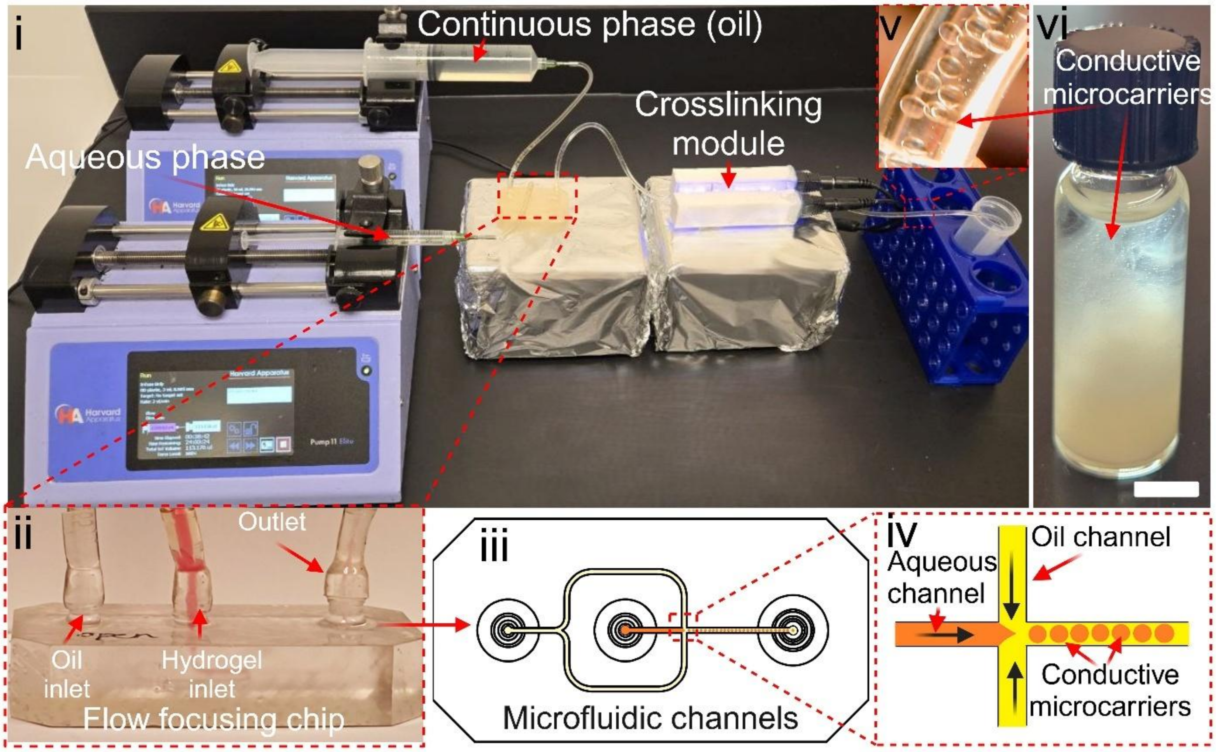

Figure 2 Microfluidic generation of conductive microcarriers. (i) Illustration of the microfluidic droplet generation setup, where a GelMA-BIL solution is emulsified using a flow focusing microfluidic device and subsequently subjected to in situ photo-crosslinking. (ii) Image of the flow focusing droplet generator with designated inlets for the continuous (oil phase) and dispersed (aqueous phase) flows, along with an outlet for collecting the generated microcarriers. (iii) Schematic representation of the microfluidic chip and channels. (iv) Detailed diagram of the droplet formation process within the microfluidic channels, showing the aqueous phase merging with the continuous oil phase to form microcarriers. (v) Image of crosslinked microcarriers going through the tubing after fabrication. (vi) The final crosslinked microcarriers in suspension. Scale bar= 5 mm.

Figure 2(ii) displays the flow focusing chip used for microcarrier generation, while Figure 2(iii) provides an illustration of the same chip. Figure 2(iv) offers a close-up view of the flow focusing junction, highlighting the interaction between the continuous (oil) phase and the aqueous (hydrogel) phase, leading to the formation of conductive microcarriers. These microcarriers then pass through a photo-crosslinking module equipped with 20 standard LEDs (wavelength: 405 nm). As they exit through the output tubing (Figure 2(v)), the fully crosslinked microcarriers are shown in suspension in Figure 2(vi).

The fabricated microcarriers exhibit a homogeneous size distribution, as seen in Figure 3, which presents the microcarrier compositions: GB-7-0 (GelMA 7% w/v), GB-7-2.5, and GB-7-5.

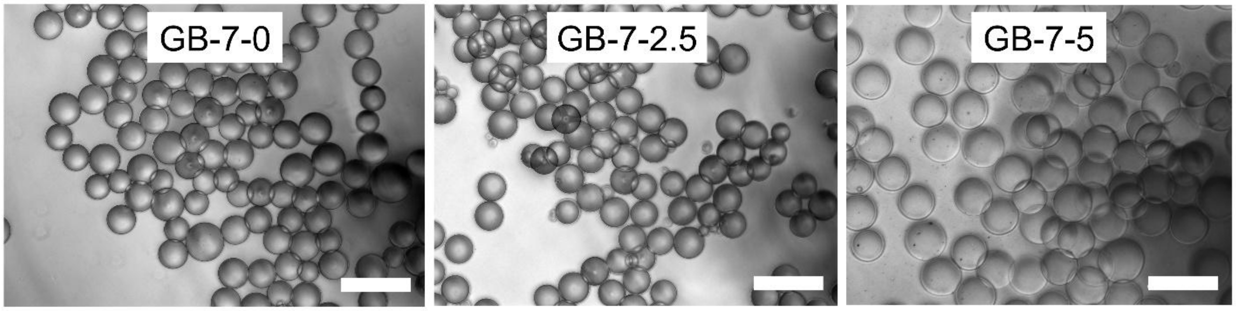

Figure 3 Bright-field microscopy images comparing the size and uniformity of microcarriers: GB-7-0, GB-7-2.5, and GB-7-5. Scale bars = 500 µm.

Figure 4(A) illustrates the size distribution of these microcarriers, with average diameters of 198.77 ± 18.77 µm, 197.76 ± 11.53 µm, and 233.31 ± 18.11 µm, respectively. Figure 4(D) displays the polydispersity index (PDI) for each microcarrier group. The PDI serves as a measure of size uniformity, with higher values indicating broader size distributions within the sample [21]. The calculated PDI values for GB-7-0, GB-7-2.5, and GB-7-5 are 0.094, 0.058, and 0.077, respectively- all below 0.1- indicating a high degree of size uniformity [101].

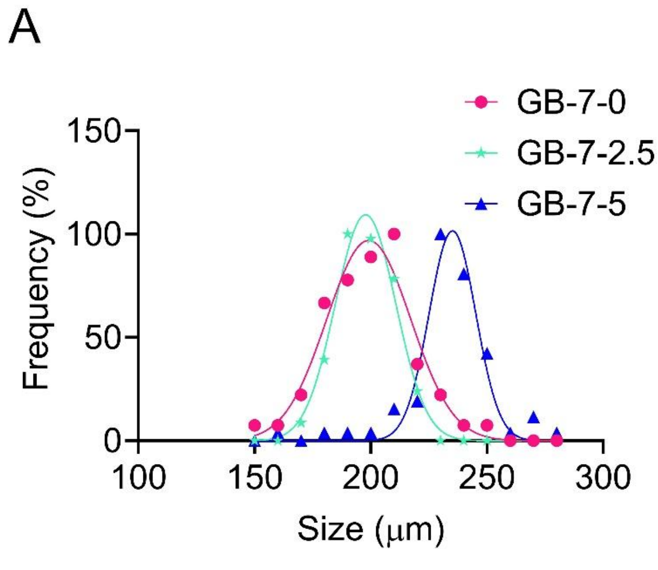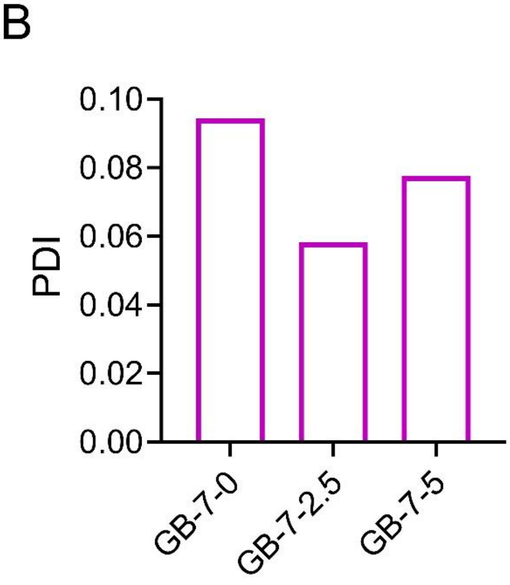

Figure 4(A) Size distribution analysis of the conductive microcarriers fabricated under a fixed flow rate condition (oil phase: 70 μL/min, aqueous phase: 5 μL/min) (n > 100). (B) Polydispersity index (PDI) of the microcarriers (n>100).

2.3.2 Material Characterization

To assess the physicochemical and electrical properties of the fabricated GelMA-BIL microcarriers, a series of characterization experiments were performed. Figure 5 presents the swelling capacity of the microcarriers over a 70-hour period. Based on Eq. 2, GB-7-2.5 and GB-7-5 exhibit significantly lower swelling capacities, measuring 6.81% and 4.69%, respectively, compared to GB-7-0, which reaches 23.49%. This reduction in swelling capacity upon the incorporation of an additive into the GelMA matrix aligns with findings from previous studies, which also report a decrease in hydrogel swelling when additional materials are introduced [1, 102, 103].

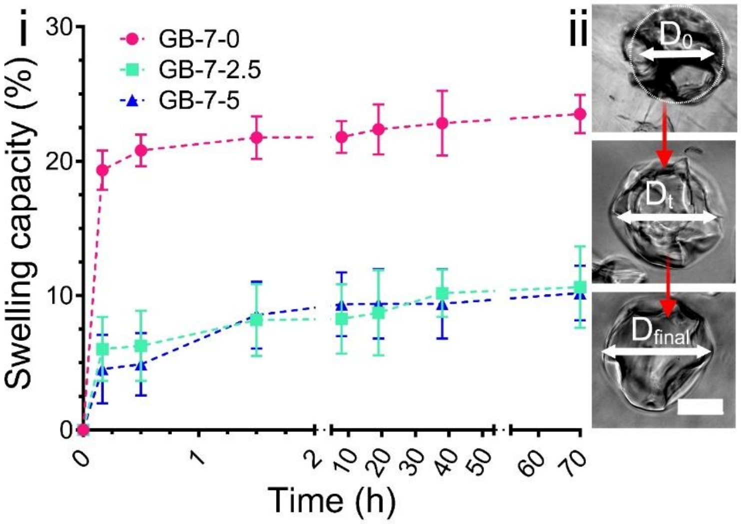

Figure 6 (i) Swelling capacity of microcarriers with different BIL concentrations over 70 hours, showing a significant reduction in swelling with increasing BIL content. Data represent an average of at least seven replicates per time point in each group. (ii) Image of a dried GB-7-5 microcarrier with a diameter of D_0 , absorbing DMEM and swelling through time (D_t) and reach to the final diameter (D_{final}) after 70 hours. Scale bar= 100 µm.

Figure 6 presents a visual comparison of crosslinked GelMA-BIL hydrogels with varying BIL concentrations (0% to 5% w/v). To prepare these samples, 1 mL of each solution was transferred into separate bottles and crosslinked using a Kudo3D chamber for three

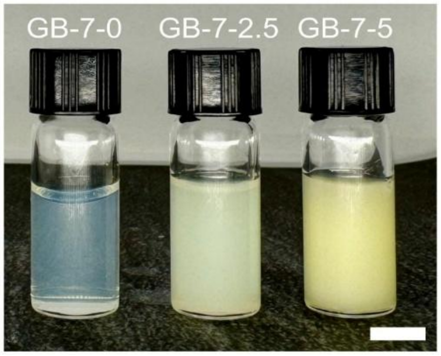

Figure 5 Photographic comparison of crosslinked GelMA-BIL hydrogels containing 0%, 2.5%, and 5% BIL (w/v). The increasing BIL concentration leads to a more pronounced yellow-orange coloration, indicating successful incorporation of the bio-ionic liquid. Hydrogels were crosslinked using a standard LED chamber (405 nm wavelength, 3 minutes).

minutes under 405 nm wavelength light. As the BIL concentration increases, the hydrogels develop a progressively deeper yellow-orange hue, signifying the successful incorporation of the bio-ionic liquid into the hydrogel network. The distinct color variations among the samples demonstrate the tunability of the hydrogel composition, which plays a crucial role in influencing both its physicochemical and electrical properties.

To assess the impact of BIL concentration on the conductivity of aqueous solutions, conductivity measurements for GB-7-0, GB-7-2.5, and GB-7-5 were performed. Measurements were conducted using a HACH SL1000 portable parallel analyzer (Hach Company, Loveland, CO, USA) at room temperature. For each concentration, three independent 4 mL samples were prepared. The conductivity of each sample was measured three times to ensure accuracy, and the readings were averaged to obtain a single value per sample (Figure 7).

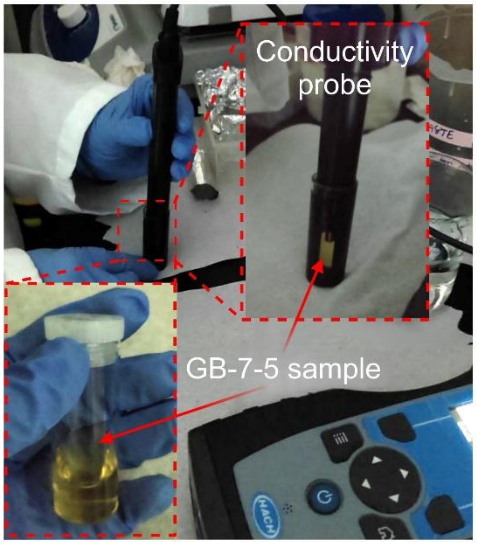

Figure 7 Measurement of aqueous phase conductivity using a HACH conductivity probe, with a zoomed-in view of the GB-7-5 sample prior to measurement.

Figure 8 illustrates the conductivity values measured by the HACH conductivity probe, showing a significant increase in conductivity as the BIL content rises. The mean conductivity values recorded were 0.066 S/m for GB-7-0, 0.347 S/m for GB-7-2.5, and 0.663 S/m for GB-7-5.These results demonstrate a direct correlation between BIL concentration and the conductivity of the aqueous phase, indicating that higher BIL concentrations enhance the ionic conductivity of the solution.

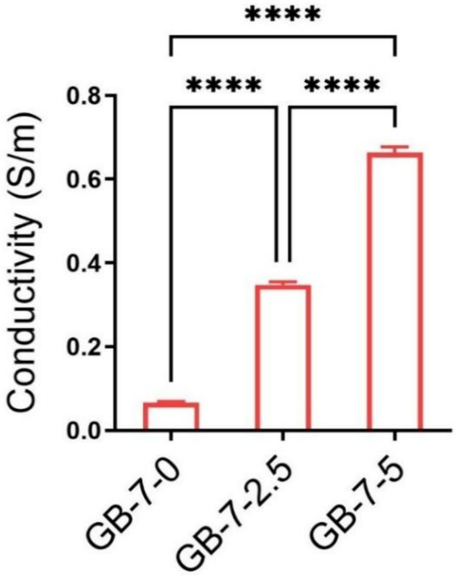

*Figure 8 Conductivity values (S/m) of GelMA (7%) + BIL (0%) (GB-7-0), GelMA (7%) + BIL (2.5%) (GB-7-2.5), and GelMA (7%) + BIL (5%) (GB-7-5), showing a significant increase in conductivity with higher BIL concentrations. Data are based on three replicates per group. Statistical analysis was performed using one-way ANOVA (****p < 0.0001).*

The addition of BIL leads to a notable increase in conductivity, with GB-7-2.5 showing a marked improvement over GB-7-0, suggesting that the bio-ionic liquid effectively introduces charge carriers into the hydrogel network [97]. The conductivity further increases in GB-7-5, where the highest value is recorded, highlighting the crucial role of BIL in enhancing ionic transport. Notably, the conductivity values measured for GB-7-2.5 and GB-7-5 fall within the typical range for skeletal muscle tissue (0.04 to 0.5 S/m) [104], emphasizing their potential biomedical relevance. Statistical analysis using one-way ANOVA confirms that the differences in conductivity among the three groups are highly significant ($p < 0.0001$). The error bars indicate consistency across replicates, strengthening the reliability of these findings.

2.3.3 Evaluating Viability, Attachment, and Proliferation of C2C12 Cells on Electroconductive Microcarriers

Evaluating biocompatibility is essential to confirm that biomaterials effectively support cell adhesion, viability, and proliferation. To assess cytotoxic effects, a live/dead staining assay was conducted on day 7 of cell culture on the microcarriers, distinguishing viable cells (green) from non-viable cells (red). To determine initial adhesion efficiency, a cell attachment assay was performed on C2C12 cells, as adhesion plays a critical role in biocompatibility and tissue engineering applications. Additionally, the Trypan Blue viability test was used to further assess potential cytotoxic effects of BIL. Finally, a proliferation study monitored cell growth over time to investigate whether BIL enhances cellular expansion through bioelectrical interactions.

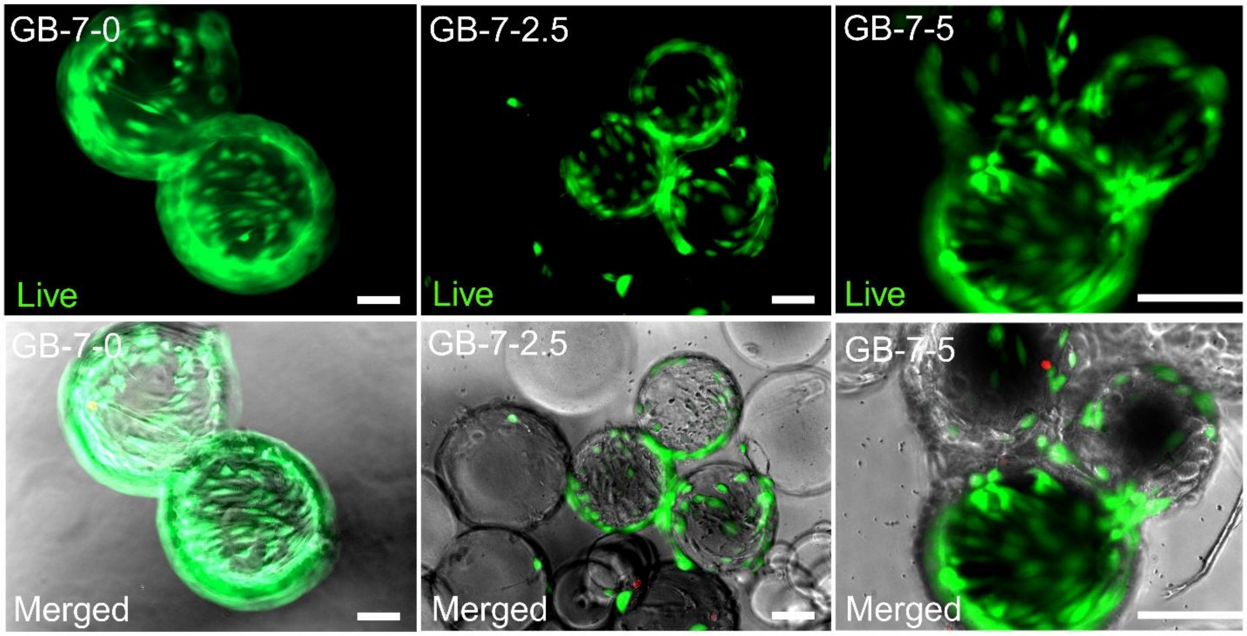

Figure 9 Fluorescent staining of C2C12 cells cultured on microcarriers on day 7: live cell staining: green and merged Live/Dead/Bright-field imaging (live: green, dead: red, bright-field: gray)- Scale bar= 100 µm. Samples were collected from 3 replicates.

Figure 9 displays fluorescent images of C2C12 cells cultured on microcarriers after seven days. Live cells are stained green, while dead cells appear red. The bright-field overlay images further provide structural details of the microcarriers. The images demonstrate that C2C12 cells adhere well to the microcarriers in all conditions, with a high proportion of green-stained live cells. The presence of only a few red-stained dead cells suggests minimal cytotoxic effects across all formulations. Figure 10 quantifies the percentage of cells attached to microcarriers 24 hours post-seeding. The attachment percentage for GB-7-0, GB-7-2.5, and GB-7-5 was 96.7% ± 2.3, 95.5% ± 4.5, and 88.75% ± 8.9 respectively. Statistical analysis of the results shows no significant differences (ns) in attachment efficiency across the three formulations (GB-7-0, GB-7-2.5, and GB-7-5), suggesting that BIL incorporation does not adversely impact initial cell adhesion.

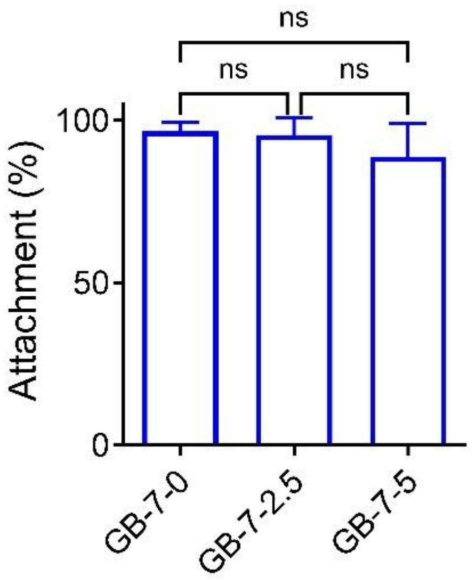

Figure 10 Cell attachment assay showing the percentage of C2C12 cells adhered to microcarriers with varying BIL concentrations (0%, 2.5%, 5%) after 24 hours of incubation. Number of replicates= 4. Statistical analysis was done by one-way ANOVA. (ns :not significant for $p > 0.05$)

Figure 11 presents the percentage of live cells assessed using a trypan blue exclusion assay on days 1, 3, and 7. The viability remains consistently high across all conditions, with no statistically significant differences (ns) observed between groups at any time point.

These results further confirm that BIL-containing microcarriers support cell survival without inducing cytotoxicity over the seven-day culture period. Finally, the proliferation of C2C12 cells cultured on microcarriers with varying BIL concentrations (0%, 2.5%, and 5%) was monitored over seven days to assess the impact of BIL on cell growth.

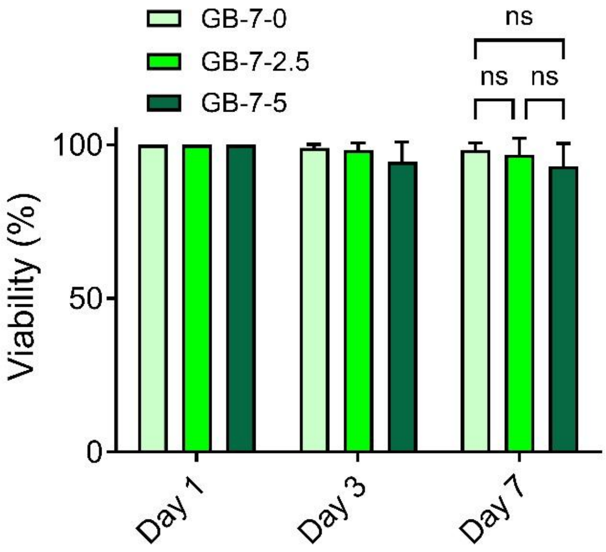

Figure 11 Percentage of live cells on day 1, 3,and 7 using trypan blue assay. Number of replicates= 4. Statistical analysis was done by one-way ANOVA. (ns :not significant for p > 0.05)

Figure 12 illustrates C2C12 cell proliferation over time, measured as total cell count on days 1, 3, and 7. The proliferation trends observed in the plot indicate that all conditions started with similar cell counts on Day 1. By Day 3, slight variations in proliferation emerged, but no statistically significant differences were detected between the groups. However, by Day 7, a clear difference in proliferation became apparent, with GB-7-0 exhibiting the highest cell count, followed by GB-7-2.5, while GB-7-5 showed the lowest proliferation. Statistical analysis confirmed a significant decrease in proliferation for GB-7-5 compared to GB-7-0 ($p < 0.01$), whereas the differences between GB-7-0 and GB-7-2.5, as well as GB-7-2.5 and GB-7-5, remained statistically insignificant (ns).

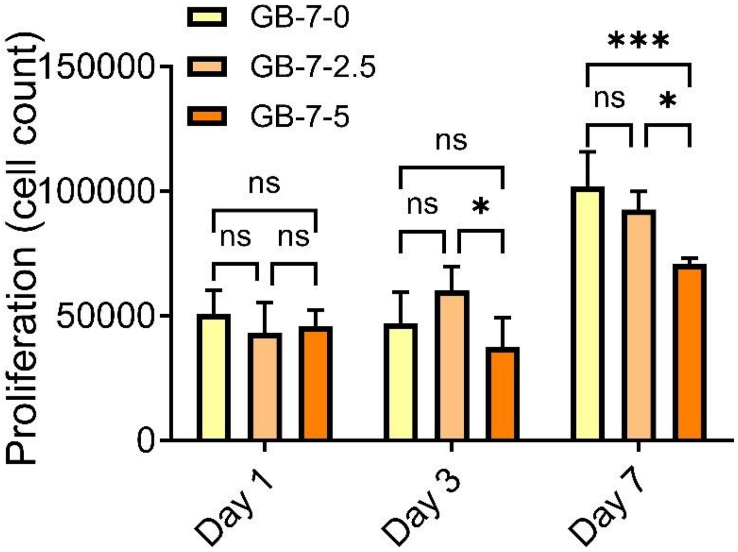

*Figure 12 Cell proliferation assay quantifying C2C12 cell growth on microcarriers with different BIL concentrations on days 1, 3, and 7, highlighting the effect of conductivity on cell proliferation. Number of replicates= 4. Statistical analysis was done by one-way ANOVA. (ns :not significant for $p > 0.05$, ** for $p < 0.01$)*

To better understand the impact of BIL concentration on cell proliferation, the fold increase in cell count from Day 1 to Day 7 was calculated. The results revealed that GB-7-0 exhibited the highest proliferation rate, with a 2.29-fold increase over the culture period. In comparison, GB-7-2.5 displayed a 1.83-fold increase, while GB-7-5 exhibited the lowest proliferation rate at 1.69-fold. These findings suggest that higher BIL concentrations may not necessarily enhance cell growth. This study demonstrates that the incorporation of BIL does not hinder C2C12 cell attachment, indicating that the modified microcarriers provide a suitable surface for initial adhesion. However, long-term cell proliferation is adversely affected in BIL-containing conditions. A possible explanation lies in the natural progression of muscle development, where myoblasts first undergo rapid proliferation before transitioning into differentiation. Once committed to differentiation, these cells exit the cell cycle, fuse, and begin expressing myogenic markers [105, 106]. The observed decline in proliferation in the presence of BIL may be attributed to an accelerated shift toward differentiation, suggesting that BIL could be influencing the transition from a growth phase to a maturation phase, thereby limiting further cell expansion.

2.3.4 Functional Assessment: Impact of BIL on C2C12 Cell Morphology and Myogenic Differentiation

The decline in C2C12 cell proliferation observed in BIL-containing microcarriers, as discussed in the previous section, may be linked to the induction of myogenic differentiation. To explore this possibility, we evaluated two key markers of differentiation: nuclear elongation and myosin heavy chain (MyHC) expression. Nuclear elongation was quantified using the nuclear aspect ratio, a widely recognized morphological indicator of myoblast differentiation. Previous studies by T. M. Watanabe et al. have shown that as C2C12 myoblasts transition into myotubes, their nuclear morphology undergoes significant alterations, characterized by an increase in the nuclear aspect ratio. This shift reflects the transition from a rounded myoblast state to an elongated myotube phenotype, a hallmark of muscle differentiation [107]. The elongation of nuclei is driven by mechanical forces exerted on the nucleus during differentiation, leading to structural reorganization within the nuclear architecture [107]. As a result, the nuclear aspect ratio serves as a reliable morphological marker of C2C12 differentiation [108]. Beyond changes in nuclear shape, C2C12 differentiation is accompanied by broader cellular transformations, including chromatin remodeling and histone modifications, which play a crucial role in regulating gene expression during muscle development. These molecular and structural alterations collectively influence cell fate decisions, further reinforcing the role of nuclear morphology in tracking myogenic differentiation [107].

In this section, an immunofluorescence-based assessment of C2C12 myoblasts cultured on GelMA-BIL microcarriers with varying BIL concentrations (0%, 2.5%, and 5%) is presented. Following the immunofluorescence imaging, two essential markers of myogenic differentiation are evaluated: nuclear elongation and Myosin Heavy Chain (MyHC) expression. These indicators provide valuable insights into the effects of BIL incorporation on muscle cell maturation and differentiation.

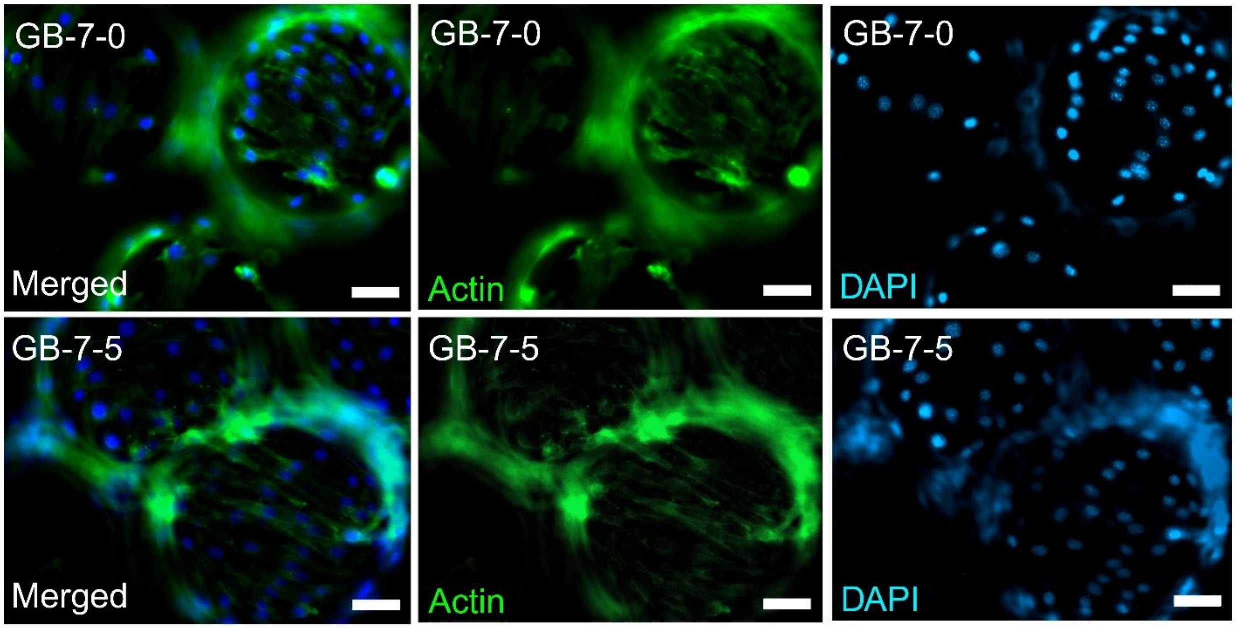

Figure 13 Immunofluorescence staining of C2C12 myoblasts cultured on GelMA-BIL microcarriers with varying BIL concentrations. On the left: Merged images of DAPI-stained nuclei (blue) and actin cytoskeleton (green), In the middle: actin staining, and on the right: DAPI staining. Scale bars: 50 µm.

Figure 13 displays immunofluorescence images showing actin cytoskeleton (green) and nuclei (blue, DAPI-stained) for cells cultured on GB-7-0 (0% BIL) and GB-7-5 (5% BIL) microcarriers. The DAPI-stained nuclei in GB-7-5 appear more elongated, whereas those in GB-7-0 remain rounded, indicating potential differences in cellular maturation. This observation suggests that higher BIL concentrations promote nuclear elongation, a key feature of muscle differentiation. To quantify this observation, nuclei aspect ratio analysis was done on DAPI stained images of both groups of microcarriers. Figure 14 illustrates nuclear elongation by measuring the nuclear aspect ratio. The dot plot shows a significant increase in the nuclear aspect ratio in GB-7-5 compared to GB-7-0. The average nuclear aspect ratio in GB-7-0 was 1.30, whereas in GB-7-5, it increased to 1.49. This increase suggests that nuclei in GB-7-5 are more elongated, a well-established hallmark of myogenic differentiation. Additionally, the distribution of data points in GB-7-5 is broader, indicating greater variability in nuclear shape, whereas GB-7-0 shows a more clustered distribution, suggesting a predominantly rounded nuclear morphology. These findings

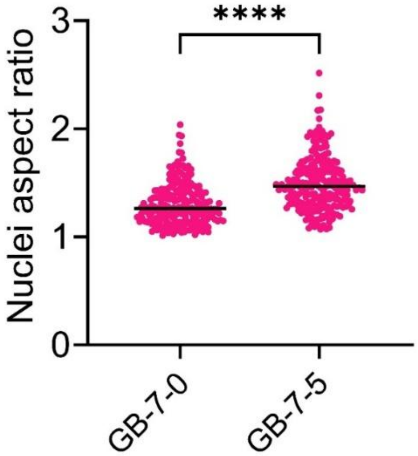

*Figure 14 Results of image processing of the nuclei aspect ratio across two groups done by ImageJ threshold processing (Number of replicates > 230). Statistical analysis was done by one-way ANOVA. (****p < 0.0001)*

support the hypothesis that BIL promotes nuclear elongation, likely due to mechanical forces and cytoskeletal changes that occur during differentiation [107, 108].

Figure 15 evaluates myogenic differentiation by quantifying the percentage of Myosin Heavy Chain-positive (MyHC+) cells, a widely recognized marker of muscle maturation. The data from the flow cytometry analysis (Figure 15A) reveal a progressive increase in MyHC+ cells with increasing BIL concentrations, confirming that BIL promotes myogenic

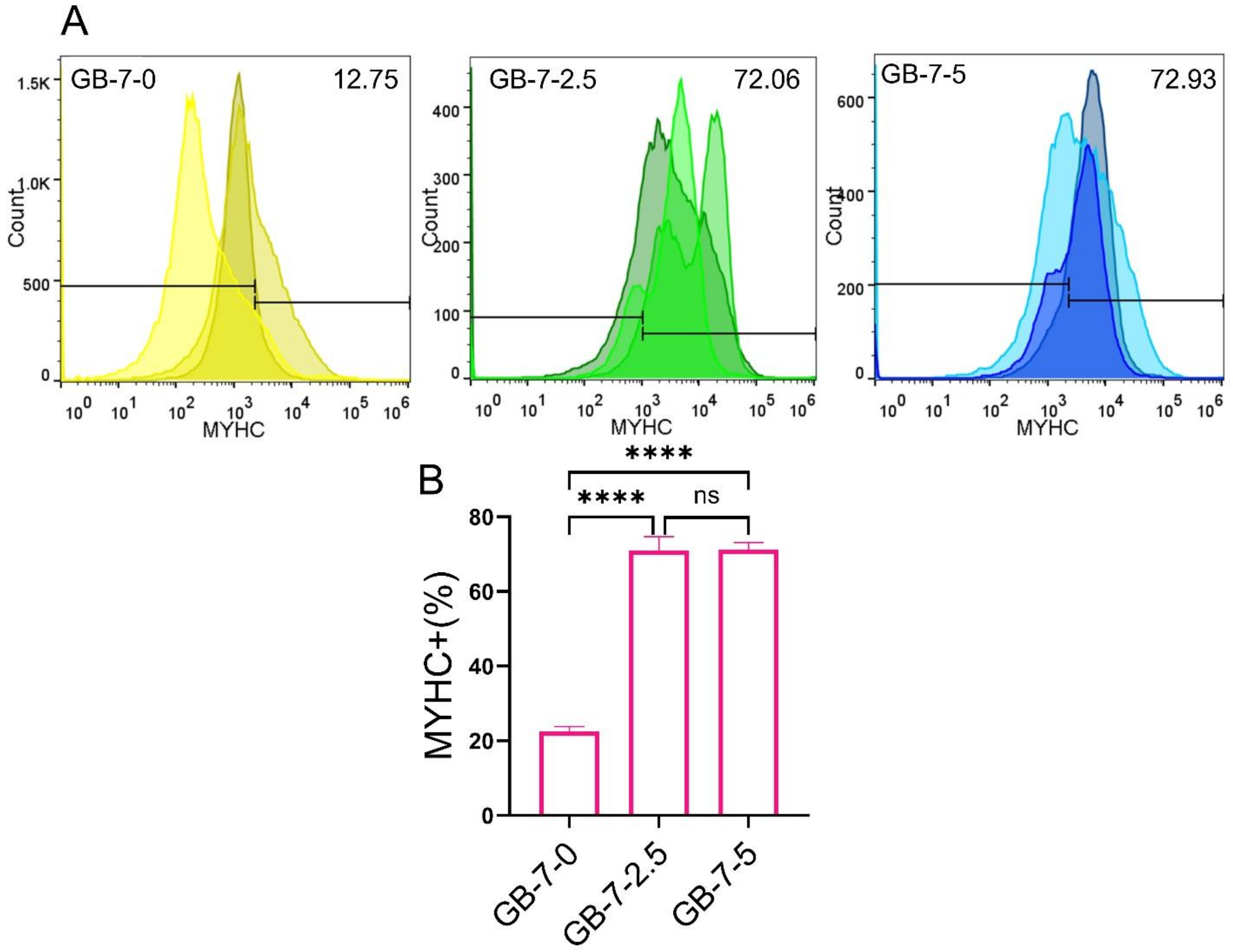

*Figure 15 Assessment of myogenic differentiation, represented by the percentage of MyHC+ cells, across varying BIL concentrations (0%, 2.5%, 5%). A) Flow cytometry plots showing the MyHC expression result for the three conditions. B) A significant increase in MyHC+ cells is observed with BIL incorporation. Number of replicates= 3. Statistical analysis was done by one-way ANOVA. (ns= not significant p>0.05, *p < 0.05, **p < 0.01, ***p < 0.001, and ****p < 0.0001)*

differentiation. Figure 15B, which a column plot demonstrating the results from Figure 15A, shows that the percentage of MyHC+ cells in GB-7-0 is significantly lower compared to GB-7-2.5 and GB-7-5. However, no significant difference (ns) was observed between GB-7-2.5 and GB-7-5, suggesting that a 2.5% BIL concentration is sufficient to induce differentiation, with no additional benefit at 5% BIL. Taken together, these results indicate that BIL-containing microcarriers enhance myogenic differentiation in C2C12 cells

The observed increase in nuclear elongation (Figure 14) and MyHC expression (Figure 15) with higher BIL concentrations suggests that BIL facilitates the transition from a proliferative to a differentiated state. However, the plateau effect in MyHC expression between GB-7-2.5 and GB-7-5 suggests that higher BIL concentrations beyond 2.5% may not further enhance differentiation. These findings highlight the potential of BIL-based biomaterials in muscle tissue engineering, where electrical conductivity may play a role in guiding myoblast differentiation and cytoskeletal organization.

2.4 Summary and Key Findings

This study successfully demonstrates the development and characterization of electroconductive GelMA-BIL microcarriers for skeletal muscle tissue engineering applications. Using a microfluidic flow focusing approach, we fabricated monodisperse, tunable microcarriers incorporating bio-ionic liquid (BIL) to enhance their electrical conductivity. Characterization of the microcarriers revealed a significant increase in conductivity with higher BIL concentrations, with values aligning within the range of native skeletal muscle tissue, highlighting their potential biomedical relevance.

Biocompatibility assessments confirmed that BIL integration does not impair cell adhesion or viability, as C2C12 myoblasts readily attached and remained viable on all microcarrier formulations. However, cell proliferation was significantly reduced in BIL-containing microcarriers, particularly at higher BIL concentrations, suggesting a shift toward early differentiation. This hypothesis was further supported by morphological and functional analyses, which demonstrated a notable increase in nuclear elongation and Myosin Heavy Chain (MyHC) expression in cells cultured on BIL-containing microcarriers. These findings indicate that BIL promotes myogenic differentiation, facilitating the transition of C2C12 cells from a proliferative state to a more mature myogenic phenotype.

In conclusion, our findings suggest that electroconductive GelMA-BIL microcarriers provide a dynamic microenvironment that supports myoblast differentiation. The ability of BIL to modulate cellular behavior through bioelectrical interactions presents a promising avenue for enhancing skeletal muscle regeneration and tissue engineering strategies. Future investigations should explore long-term functional assessments of these microcarriers, including their effects on myotube formation, contractility, and in vivo performance. By bridging the gap between biomaterial conductivity and muscle tissue engineering, this study establishes a versatile platform for scalable muscle cell manufacturing and regenerative medicine applications.

3 Chapter 3: Conductive Microcarriers for Tissue Engineering: A GelMA-PEDOT:PSS Platform

Note: Submission to a journal is in progress. Immunofluorescence imaging (Figure 27) was generated by Esfandyar Askari. Flow cytometry test and data analysis (Figure 29) was generated by Mahdieh Shokrollahi Barough. All other experiments and analysis were performed by the candidate.

3.1 Introduction

Producing large quantities of cells for tissue engineering, drug discovery, and therapeutic applications is a major challenge. Bioreactors are essential for scaling up cell production, as they provide a controlled environment for cell growth and expansion [109, 110]. To cultivate adherent cells at large scale, microcarriers are necessary as substrates, offering increased surface area for cell attachment and growth in suspension culture [109, 111-114]. However, existing microcarrier systems are limited in mimicking the natural cellular environment [110, 112-115]. Additionally, traditional microcarriers often require complex manufacturing processes and may face issues with scaling production capabilities [109, 114]. To address these limitations, hydrogel-based microcarriers have emerged as a promising alternative. These soft, porous, and often biodegradable substrates offer several benefits, such as improved cell attachment, enhanced nutrient diffusion, and easier cell harvesting [109, 110, 115]. Gel-based microcarriers can be designed to more closely resemble the extracellular matrix (ECM) more closely, potentially improving cell function and differentiation [110, 112-115]. Furthermore, some gel-based microcarriers are dissolvable which simplifies downstream processing by eliminating the need for microcarrier removal from the final product [109, 111, 115]. Although hydrogel-based MCs have demonstrated the ability to support improved cell attachment, function, and expansion, their application for tissues such as skeletal muscle where electrical activity plays a critical role remains limited due to their lack of electrical conductivity [66, 102].

Conductive materials have shown great promise in tissue engineering applications due to their ability to mimic the electrical properties of native tissues, enhance cell signaling and communication, and promote the regeneration of electrically responsive tissues such as cardiac, neural, and musculoskeletal systems [104, 116-119]. These materials can facilitate the integration of engineered constructs with the body's natural electrical environment, improving functional outcomes and advancing the development of more effective biomimetic tissue engineering solutions [104, 116, 120-123]. They also, at the cellular scale, contribute to maturation and synchronous contraction [44].

Various electroconductive materials have been explored for tissue engineering applications, including gold nanomaterials, graphene-based materials, and conductive polymers [104, 116, 124, 125]. Gold nanomaterials, particularly gold nanoparticles (AuNPs), have demonstrated excellent biocompatibility and the ability to regulate cell differentiation and promote tissue regeneration in bone and cartilage engineering [124, 125]. Graphene-based materials offer high electrical conductivity and mechanical strength, making them suitable for various tissue engineering applications [104, 116]. However, achieving conductivity with nanomaterials/particles in scaffolds often requires high concentrations, which may raise concerns about toxicity and degradation [126-128].

Conductive polymers offer tunable conductivity, allowing precise control over electrical stimulation to guide cell behavior and promote tissue regeneration. Additionally, these polymers provide mechanical flexibility and softness, closely mimicking the native ECM of soft tissues such as neural and cardiac tissues. This flexibility reduces the risk of mechanical mismatch with host tissues, which is particularly important for maintaining cell viability and function [129-131]. Among conductive polymers, poly(3,4-ethylenedioxythiophene):poly(styrene sulfonate) (PEDOT:PSS) has emerged as a promising material for tissue engineering scaffolds [63-66]. PEDOT:PSS exhibits several advantageous properties, including adjustable conductivity, good transparency to visible light, excellent thermal stability, and biocompatibility [63-66]. These characteristics make this material an ideal candidate for creating biomimetic environments that support cell growth and function [65, 66]. PEDOT:PSS is particularly well-suited for growing cells due to its ability to form stable hydrogels with high water content (80-87 w/v) and long-term stability in wet physiological environments [63, 65, 66]. The material has high electrical conductivity (approximately 20 S/cm in PBS and 40 S/cm in deionized water), which allows for efficient signal transmission and cell-cell communication [63, 65]. Additionally, PEDOT:PSS hydrogels exhibit low Young's modulus (~2 MPa) and high stretchability (>35% ductility), which closely mimic the mechanical properties of native tissues [63, 65, 66].

Microfluidic flow focusing for the production of microcarriers has emerged as a highly precise and efficient technique, enabling the generation of uniform, size-controlled microcarriers with tailored properties for applications in drug delivery, cell culture, and tissue engineering [132-134]. This method leverages the controlled manipulation of fluid dynamics to create monodisperse droplets or particles, offering advantages such as scalability, reproducibility, and the ability to incorporate functional materials or bioactive molecules [135, 136]. As a result, microfluidic flow focusing has become a pivotal tool in advancing the development of next-generation microcarriers for biomedical and therapeutic applications [132-134]. For example, studies have demonstrated the ability to generate microcarriers with diameters ranging from 100 to 450 μm with exceptional uniformity (Polydispersity index as low as 3.4%) [134]. This level of control is significantly superior to conventional methods, which often result in broader size distributions [134]. Several research groups [29-33], including ours [10, 21, 34], have successfully utilized microfluidic flow focusing technology to produce microcarriers for various biomedical applications.

In this work, we developed electroconductive microcarriers made of photocurable GelMA and PEDOT:PSS microcarriers for the first time. We used microfluidic flow focusing to produce microcarriers with high size uniformity, which is crucial for ensuring consistent cell growth [133, 134]. We evaluated the impact of PEDOT:PSS content on cell attachment and differentiation to ensure its suitability for large-scale production of skeletal muscle cells.

3.2 Experimental Section

3.2.1 Materials

A high-speed resin 3D printer (Photon Mono 2K, Anycubic, Shenzhen, China) was used to fabricate the 3D-printed microfluidic droplet generator. A clear photopolymer resin (Anycubic 405 nm UV-curing resin, Shenzhen, China) was used for the print. Key chemicals and reagents were sourced from Sigma-Aldrich (St. Louis, MO, USA), including lithium phenyl-2,4,6-trimethyl benzoyl phosphinate (LAP) (CAS# 85073-19-4), Span 80 (CAS# 1338-43-8), porcine-derived gelatin Type A (CAS# 9000-70-8), phosphate-buffered saline (PBS) tablets, and methacrylic anhydride (CAS# 760-93-0). PEDOT:PSS (PH 1000)

(CAS# 155090-83-8) was purchased from Ossila. Additional materials such as fetal bovine serum (FBS) (Cat#16000044), Dulbecco's Phosphate Buffered Saline (DPBS) (Cat#14190144), trypsin/EDTA (Cat#15400054), and Dulbecco's Modified Eagle Medium (DMEM) (Cat#11965118) were procured from Gibco (Grand Island, NY, USA). The Live/Dead viability/cytotoxicity kit for mammalian cells (Cat#L3224) was supplied by Invitrogen via ThermoFisher Scientific (Waltham, MA, USA). The PrestoBlue cell viability reagent was supplied by Invitrogen via ThermoFisher Scientific (Cat#A13261). In addition, heavy mineral oil (Cat# 8042-47-5) was obtained from Fisher Chemical (Waltham, MA, USA), and dialysis membranes with a molecular weight cutoff (MWCO) of 12–14,000 were sourced from Spectro/Por through Fisher Scientific.

3.2.2 GelMA Synthesis

GelMA was synthesized following a previously established protocol [137]. In brief, 10 g of porcine skin gelatin was dissolved in 200 mL of PBS at 60 °C to create a 5% gelatin solution. 8 mL of Methacrylic anhydride was added drop-wisely into the solution, which was then stirred at 300 rpm for 3 hours to generate GelMA with high degrees of methacrylation (DOM). To halt the reaction, 300 mL of preheated PBS (40-50 °C) was added, stirring for 15 minutes. The resulting GelMA solution was filtered, and then poured into dialysis membranes with a molecular weight cutoff (MWCO) of 12–14 kDa and dialyzed for two weeks at 40-50 °C. To ensure complete removal of unreacted methacrylic anhydride and other impurities, the membranes were immersed in distilled water, stirred at 50 rpm, and the water was changed twice daily, with the membranes reversed each time. Finally, the GelMA solution was filtered and lyophilized to obtain a solid GelMA product.

3.2.3 Microfluidic Device Fabrication Using 3D Printing

The microfluidic chip, featuring channel dimensions ranging from 500 to 750 μm, was designed using SOLIDWORKS™ software (Version 2025 SP0. University of Victoria academic license. Waltham) and fabricated using a 3D printer (Photon Mono 2K, Anycubic, Shenzhen, China). 3D printing was chosen for its high precision and ability to produce intricate microfluidic features with exceptional accuracy, ensuring reproducibility and fine control over channel dimensions.

Before each printing cycle, the printer and resin vat were carefully inspected to eliminate any potential contaminants that could affect the print quality. Dust particles were removed from the printer using compressed air, while any impurities in the resin vat were extracted using a pipette. Following the printing process, the fabricated components underwent a thorough cleaning procedure with isopropanol to remove any residual uncured resin, ensuring high fidelity of the printed structures. The cleaned components were then dried using compressed air and subjected to post-curing in a Kudo3D post-curing chamber for 30 minutes at room temperature to enhance the mechanical and chemical stability of the microfluidic chip.

3.2.4 Microcarriers Generation

Microcarriers were produced using the hydrogel solution going through a microfluidic flow focusing systems as previously described [10, 21]. To generate droplets, the continuous phase consisted of heavy mineral oil mixed with 10% (w/v) Span-80, a non-ionic surfactant. The dispersed (hydrogel) and continuous phases were loaded into plastic syringes and connected to the microfluidic device via Tygon tubing. A 50 mL syringe introduced the continuous phase, while a 3 mL syringe, mounted on a syringe pump (Harvard Apparatus PHD 2000, USA), delivered the dispersed phase. The flow rates for the continuous phase and the aqueous phase were 70 µL/min and 8 µL/min, respectively. Droplets formed at the chip's flow-focusing junction and passed through a crosslinking module, where exposure to visible light induced in situ photo-crosslinking. This module, equipped with 20 standard 405 nm LEDs, crosslinked the MCs as they flowed through.

The crosslinked MCs were washed via centrifugation to remove residual oil and surfactants. The washing process involved sequential washing: two rinses with PBS containing 1% dish soap, followed by two washes with a 50% ethanol/PBS solution, and three rinses with PBS. Finally, they were soaked in 70% ethanol overnight for sterilization. They were then washed twice using sterile PBS. Purified MCs were either lyophilized and stored at 5 °C for future use or soaked in cell culture medium for 72 hours before biological studies.

3.2.5 Microcarrier Size Characterizations

The formation of microcarriers was further analyzed by measuring their size using a Zeiss Axio Observer microscope (Germany). For this purpose, a drop of the microcarrier suspension was placed between two coverslips and observed under the microscope to capture bright field images. ImageJ software (version 1.54d, National Institutes of Health, USA) was used to determine the microcarrier sizes. The size distribution of the microcarriers was plotted with 5 um intervals and their monodispersity was quantified by calculating the polydispersity index (PDI) using Eq.1, where σ represents the standard deviation of microgel diameters and D_m is the mean diameter of the microgels [21].

$$PDI = \frac{\sigma}{D_m} \tag{1}$$

3.2.6 Swelling Capacity Measurement

To investigate the swelling dynamics of the fabricated microcarriers, they were lyophilized for 24 hours. Their average diameter when dried was measured. Then they were soaked in cell culture media, and their diameters were measured over a 70-hour period of incubation at 37 °C. At specific time intervals, optical microscope images were captured, and the diameters of the microcarriers were measured using the ImageJ (version 1.54d, National Institutes of Health, USA).The swelling capacity was determined by calculating the ratio of the measured diameter to the initial dry diameter, as defined by Eq.2 [98]. In this equation, D_0 represents the microcarrier's diameter in its dry state, while D_t corresponds to its diameter after swelling in the medium [98].

$$Swelling\ capacity\ (\%) = \left[\frac{D_t - D_0}{D_0}\right] \times 100 \tag{2}$$

The diameter of the microcarriers increases until it reaches D_{final}.This final diameter was used to calculate the swelling capacity percentage of each microcarrier group after 70 hours.

3.2.7 Resistance Measurement of Hydrogel Solutions

To evaluate the conductivity of the crosslinked hydrogel microcarriers, electrical resistance measurements were conducted using a four-point probe setup . A two mL aliquot of the hydrogel precursor solution was poured into a 35 mm petri dish and subsequently crosslinked using Kudo3D post curing chamber for 10 minutes to form a uniform hydrogel sheet with a height of approximately 2 mm. The four probes were carefully positioned on the surface of the crosslinked hydrogel to ensure consistent contact, and resistance measurements were done using a Keithley 6430 Sub-Femtoamp Remote Source Meter. In this measurement setup, the probes were positioned 2 mm apart, and the current was applied through the outer probes, and the voltage drop was measured across the inner probes. The four-point probe method is preferred for soft materials like hydrogels because it eliminates contact resistance errors.

3.2.8 Resistance Conversion to Conductivity

The measured resistance (R) was converted to electrical conductivity (σ, in S/m) using the following formula:

$$\sigma = \frac{1}{\rho} \tag{3}$$

Where resistivity (ρ) is calculated as:

$$\rho = R\frac{A}{L} \tag{4}$$

Where R is the measured resistance (Ω), L = 2 mm = 0.002 m (probe spacing), and A = w × t is the cross-sectional area, approximated based on the hydrogel volume and dish dimensions [138]. The average resistance values measured for GP-7-0, GP-7-1, and GP-7-2 were used to calculate the corresponding conductivity values at different applied currents (1 mA and 10 mA). The computed conductivity values were as follows:

Table 4 Conductivity values calculated based on the resistance values from the four-point probe measurement.

Sample	Conductivity (S/m) at 1 mA	Conductivity (S/m) at 10 mA
GP-7-0	0.14	1.15
GP-7-1	0.34	1.69
GP-7-2	0.90	3.63

3.2.9 In-vitro Cell Culture

To evaluate the biocompatibility of the conductive microcarriers, C2C12 murine skeletal muscle cells (American Type Culture Collection, Manassas, VA, USA) were seeded onto the microcarriers and cultured under controlled conditions. C2C12 cells were maintained in complete growth media consisting of Dulbecco's Modified Eagle Medium (DMEM) (Gibco) supplemented with 10% fetal bovine serum (FBS) (Gibco), 1% penicillin/streptomycin (Gibco), and 1% GlutaMAX (Gibco) at 37°C in a humidified incubator with 5% CO_2. Cells from passage 3 were used for the experiments.

Prior to seeding, sterile 96-well plates were prepared by coating the bottom of each well with a 2% agarose (Fisher BioReagents) solution dissolved in phosphate-buffered saline (PBS) under sterile conditions. These agarose-coated plates were then incubated with DMEM at 37°C for 24 hours before cell seeding. Meanwhile, the sterile microcarriers were pre-incubated in DMEM for 72 hours at 37°C to enhance their compatibility with the cells.

On the day of seeding, the DMEM was removed from the agarose-coated wells, and approximately 100 µL of pre-incubated microcarriers were added to each well, ensuring complete surface coverage. C2C12 cells were detached using 0.05% trypsin-EDTA (Gibco) for 5 minutes, counted, and seeded at a density of 40,000 cells per well onto the microcarriers. The plates were incubated at 37°C with 5% CO_2 for 4 hours, with gentle shaking every 15–20 minutes to facilitate uniform cell attachment. After this initial attachment phase, fresh culture media was added to each well, and the cells were allowed to grow on the microcarriers for seven days under standard incubation conditions. The cell culture media was changed every other day.

3.2.10 Live/Dead Assay

The viability of C2C12 cells cultured on conductive microcarriers was assessed using the Viability/Cytotoxicity Kit for Mammalian Cells (L3224, ThermoFisher), following the manufacturer's protocol. This assay utilizes Calcein AM to stain live cells and Ethidium homodimer-1 (EthD-1) to stain dead cells. To run live/dead assay, the culture MCs were removed from the incubator, and the culture media was discarded. 200 µL of the prepared live/dead staining solution was added to the MCs, ensuring complete coverage. The samples were incubated for 2 hours at room temperature in the dark to allow the dyes to penetrate the cells while minimizing light-induced degradation. Following incubation, the live/dead staining solution was removed, and the samples were washed by replacing it with DPBS to remove excess dye. Fluorescence imaging was performed using a Zeiss Axio Observer microscope (Germany). The captured images were then analyzed to determine the viability of C2C12 cells on the conductive MCs.

3.2.11 PrestoBlue Assay

To evaluate the cytotoxic effects of the released components from MCs with or without conductive material, extraction test was performed on the MCs. The extraction method involves incubating a test material in a biological fluid (e.g., culture medium with serum) under conditions that simulate clinical use, in order to isolate any leachable substances, which are then tested for their potential cytotoxic effects on mammalian cells [139]. In this method, the MCs were incubated under standard culture conditions in DMEM medium supplemented with 10% FBS and 1% antibiotic for a total of 14 days. The extracts of the MCs were collected at three different time points: Day 3, Day 5, and Day 14. These extracts were stored under sterile conditions until further use in the cytotoxicity and viability assays.

On Day 13, C2C12 cells were seeded in 2D culture at a density of 12,000 cells per well in a 96-well plate to allow for attachment and growth overnight. On Day 14, the MC extracts collected from different time points (Day 3, Day 5, and Day 14) were added to the designated wells containing C2C12 cells. Wells designated as control groups received fresh cell culture media instead of MC extracts. All wells were incubated at 37°C and 5% CO_2 for 24 hours.

After 24 hours of incubation with MC extracts, the media was removed from all wells. A 1/10 dilution of PrestoBlue reagent was prepared in fresh cell culture media (e.g., 1 mL PrestoBlue + 9 mL media), ensuring sufficient volume to treat all wells, including three additional blank wells without cells. The working solution was warmed to 37°C in an incubator prior to application. PrestoBlue working solution was then added to each well according to the recommended volume for a 96-well plate (110 µL per well). Three wells containing only PrestoBlue and media (no cells) were included as blanks. The plate was returned to the incubator for 30-40 minutes for wells with <50% confluency or 10-20 minutes for wells with >50% confluency to allow for optimal fluorescence development. After incubation, 100 µL of the supernatant from each well was transferred to a fresh 96-well plate for measurement. The fluorescence was recorded using a spectrophotometer plate reader (Tecan, Model: Infinite 200 PRO®, Switzerland) at an excitation wavelength of 560 nm and an emission wavelength of 590 nm. The scan was performed from the bottom of the plate. The fluorescence readings from the blank wells were subtracted from all experimental wells. The viability of the control condition, in which cells were incubated with fresh media, was set as 100%. The viability of cells exposed to MC extracts was determined relative to the control condition using the formula:

$$Cell\ Viability\ (\%) = \left(\frac{Fluorescence\ Intensity\ of\ Treated\ Wells}{Fluorescence\ Intensity\ of\ Control\ Wells}\right) \times 100 \qquad (5)$$

3.2.12 Cell Attachment and Proliferation Study on Conductive Microcarriers

To evaluate the attachment efficiency of C2C12 cells on conductive microcarriers, four random wells were selected after four hours of incubation [134]. The microcarriers were carefully washed with PBS to remove any unattached cells. To detach adhered cells, trypsin-EDTA (5x) was added to the wells, followed by incubation at 37°C for 5-10 minutes. After enzymatic detachment, cell culture media (DMEM) was added to the suspension to neutralize trypsin. Then, the cell suspension was passed through a cell strainer to separate the microcarriers from the detached cells. The collected filtrate was centrifuged at 300 × g for 5 minutes, and the cell pellet was resuspended in DMEM for counting. The number of attached cells was quantified using a hemocytometer under the microscope. The percentage of the attached cells were calculated using:

$$Attachment\ (\%) = \left(\frac{Number\ of\ counted\ cells\ after\ 24\ hours}{Number\ of\ seeded\ cells}\right) \times 100 \qquad (6)$$

To assess cell proliferation on the microcarriers over time, 50,000 C2C12 cells were seeded onto the microcarriers in agarose-coated 96-well plates under static culture conditions. The number of attached cells was quantified on days 1, 3, 5, and 7 using the same detachment and counting method described above. This allowed for the assessment of cell proliferation dynamics on the conductive microcarriers over a seven-day period.

3.2.13 Immunofluorescence Staining Assay

On day 7 of culture, immunofluorescence staining was used to visualize the cytoskeletal structure and nuclear shape of C2C12 cells grown on conductive microcarriers. F- Actin filaments were stained using fluorescently labeled phalloidin, while DAPI (4′,6-diamidino-2-phenylindole) was used to label the cell nuclei. MCs were first washed twice with PBS and then fixed in 4% paraformaldehyde (VWR) at 4°C overnight. The following day, the MCs were washed again with PBS and blocked with 5% (w/v) bovine serum albumin (BSA, VWR) in 0.3% Triton X-100 (BIO BASIC) dissolved in PBS, followed by overnight incubation at 4°C. On the next day, the blocking solution was discarded, and the samples were incubated overnight at 4°C with 4 μg/mL Alexa Fluor™ 488 Phalloidin (Thermo Fisher Scientific) diluted in blocking solution (1:5 dilution) to stain the actin cytoskeleton. After the antibody solution was removed, DAPI (4’,6-Diamidino-2-Phenylindole, Dihydrochloride, Thermo Fisher Scientific) was used to stain cell nuclei, with samples incubated for 30 minutes at room temperature in the dark. Following two additional washes with PBS, the MCs were transferred onto glass slides and analyzed using fluorescence microscopy to capture cell morphology.

During differentiation, C2C12 cells transition from a round shape to an elongated, tubular morphology, as they adhere, elongate, and fuse into multinucleated myotubes [21, 34]. To quantify these morphological changes, ImageJ software (version 1.54d, National Institutes of Health, USA). was used to analyze cell structure. Nuclei elongation was assessed by measuring the nuclear aspect ratio, defined as the ratio of the longest to the shortest nuclear diameter. Randomly selected nuclei from multiple images per condition were analyzed to quantify morphological changes.

3.2.14 Flow Cytometry Analysis

Flow cytometry was used to evaluate myosin heavy chain (MyHC) expression, a key late-stage myogenic marker, to determine the proportion of differentiated cells within the population. This technique enables precise quantification of protein expression at the single-cell level, allowing for an accurate assessment of differentiation status [99].

For sample preparation, cells were detached from the microcarriers by washing with PBS, followed by enzymatic dissociation using trypsin-EDTA (10x). The cell suspension was then filtered through a 0.07 mm cell strainer to remove microcarriers. A final cell concentration of 5000 cells/µL was prepared for staining. Cells were incubated for 30 minutes in PBS containing 2% BSA, with PE-conjugated anti-mouse MyHC antibody (MF20, BD-USA) and FITC-conjugated anti-mouse MyoD antibody to label myogenic markers. After incubation, cells were diluted in 500 µL PBS and analyzed using a flow cytometer (Attune NXT, Thermo Fisher, USA) to quantify MyHC+ cells and assess the extent of C2C12 differentiation [99]. Flow cytometry data analysis was done using FlowJo software (V X.0- BD USA).

3.2.15 Statistical Analysis

All experiments were conducted with a minimum of three independent replicates, and the results were expressed as mean ± standard deviation (SD). Statistical analyses were performed using one-way ANOVA followed by Tukey's multiple comparisons test in GraphPad Prism 7.0 (GraphPad Software, San Diego, CA, USA) to assess differences between groups. Statistical significance was defined as follows: ns (not significant) for $p > 0.05$, * for $p < 0.05$, ** for $p < 0.01$, *** for $p < 0.001$, and **** for $p < 0.0001$.

3.3 Results and Discussions

We employed a microfluidic emulsion system to fabricate monodisperse conductive microspheres (See Figure 17-i). This technique enables the continuous production of uniform microcarriers with precise size control [10, 21]. Additionally, it eliminates the need for downstream sieving typically required in traditional emulsion polymerization methods to achieve consistent microcarrier sizes. By adjusting the flow rate ratios, we can accurately regulate the size of the microcarriers, and the formulation can be easily modified to obtain the desired properties [21].

The conductive hydrogel precursor solution consisted of GelMA (7% w/v), PEDOT:PSS (1% and 2% w/v), and LAP (Lithium phenyl-2,4,6-trimethylbenzoylphosphinate) (0.3% w/v) as the dispersed phase (Figure 16). The specific formulations and their corresponding codes are outlined in Table 5.

Table 5 The details of the microcarriers compositions and their corresponding codes.

PEDOT:PSS concentration (w/v%)	Code
0	GP-7-0
1	GP-7-1
2	GP-7-2

GelMA provides a biocompatible hydrogel matrix, PEDOT:PSS imparts electrical conductivity, and LAP serves as a photoinitiator to enable photo-crosslinking of the hydrogel solution. LAP is a water-soluble, cytocompatibility Type I photoinitiator widely used in the polymerization of hydrogels and other polymeric materials for biomedical applications. Its popularity stems from its improved properties compared to alternatives like Irgacure 2959, including increased water solubility, faster polymerization rates with 365 nm light, and absorbance at 400 nm that allows for visible light polymerization. These characteristics enable cell encapsulation at lower initiator concentrations and longer wavelength light, reducing toxicity and increasing cell viability [100]. The conductive hydrogel solution (aqueous phase) was injected into a Mineral oil/Span 80 solution

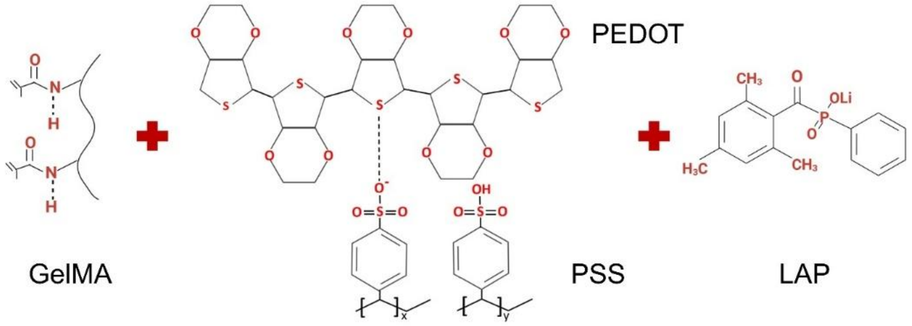

Figure 16 Chemical structure of the conductive hydrogel formulation composed of GelMA, PEDOT:PSS, and LAP. These components are dispersed in PBS for MC production. Reproduced with permission [1, 2]

(continuous phase) for microcarrier fabrication. Details of the formulations used in this process are provided in the experimental section (see Figure 17).

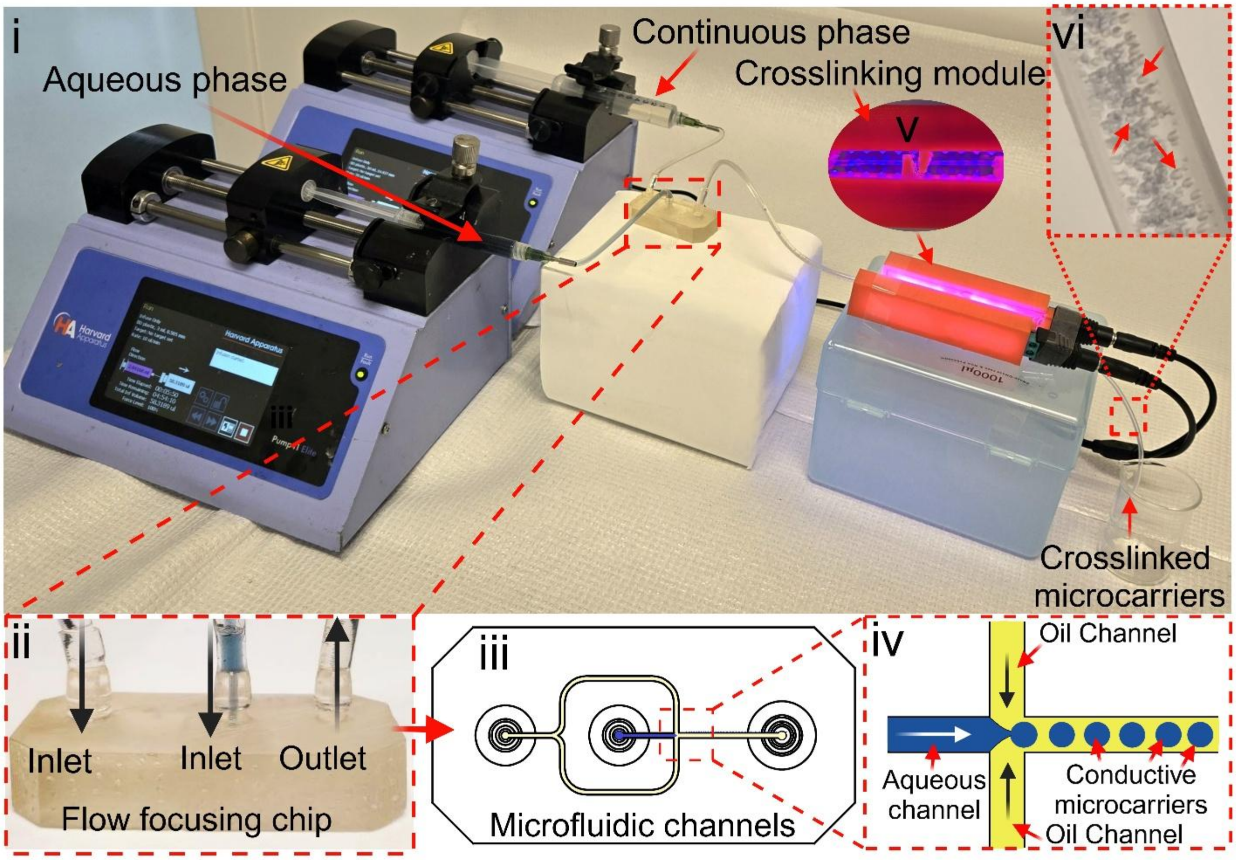

Figure 17 Fabrication and characterization of MCs using a microfluidic setup. (i) Schematic and experimental setup for microcarrier synthesis using a flow focusing microfluidic device. Droplets are generated from the conductive GelMA-PEDOT:PSS solution and crosslinked in situ using an LED array. (ii) Image of the flow focusing droplet generator, highlighting the separate inlets for the continuous and dispersed phases and the outlet for microcarrier collection. (iii) Schematic representation of the microfluidic chip, illustrating the internal microfluidic channels, inlets, and outlets. (iv) Detailed diagram of the droplet formation process within the microfluidic channels, showing the aqueous phase merging with the continuous oil phase to form microcarriers. (v) Photo-crosslinking module consisting of a 20-LED array at 405 nm, used to polymerize and solidify the microcarriers during formation. (vi) Image of the crosslinked microcarriers flowing through the tubing after fabrication

Microscopic images in Figure 18 display GelMA (7%) microcarriers produced with varying concentrations of PEDOT:PSS. The three images correspond to different PEDOT:PSS levels: GP-7-0, GP-7-1, and GP-7-2. As PEDOT:PSS concentration increases, the microcarriers appear slightly larger with minor variations in uniformity. The scale bar indicates their size ranges between 200–300 µm. To evaluate size distribution, microcarriers were generated at an oil flow rate of 70 µL/min and an aqueous flow rate of 10 µL/min.

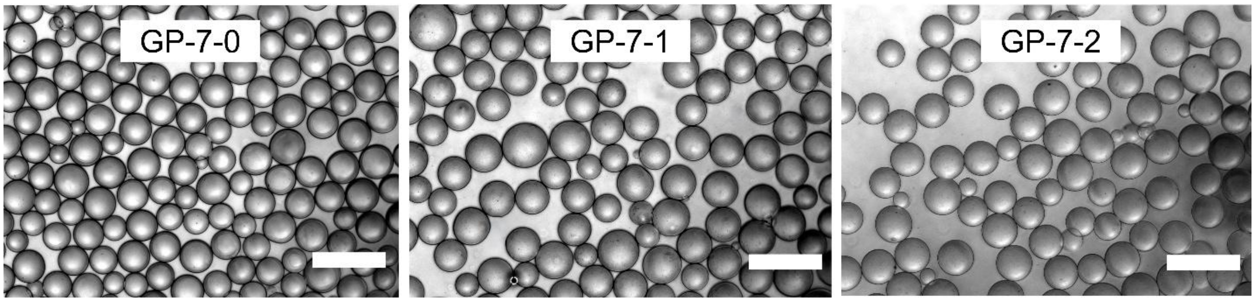

Figure 18 Microscopic analysis of the GelMA-based conductive microcarriers with different PEDOT:PSS concentrations (GP-7-0, GP-7-1, GP-7-2). The images show variations in microcarrier size and uniformity. Scale bar: 500 µm.

Figure 19A illustrates the size distribution (n > 100), where the red curve represents GP-7-0, with a mean size of 218.19 ± 12.33 µm. The blue curve, corresponding to GP-7-1, exhibits a slightly larger mean size of 241.54 ± 17.93 µm, while the green curve for GP-7-2 shows the largest average size of 243.73 ± 13.19 µm.

The polydispersity index (PDI) for the three groups, shown in Figure 19B, is 0.056 for GP-7-0, 0.074 for GP-7-1, and 0.054 for GP-7-2, all below 0.1, indicating size uniformity [101]. These findings suggest that incorporating PEDOT:PSS does not significantly impact the microcarrier generation process.

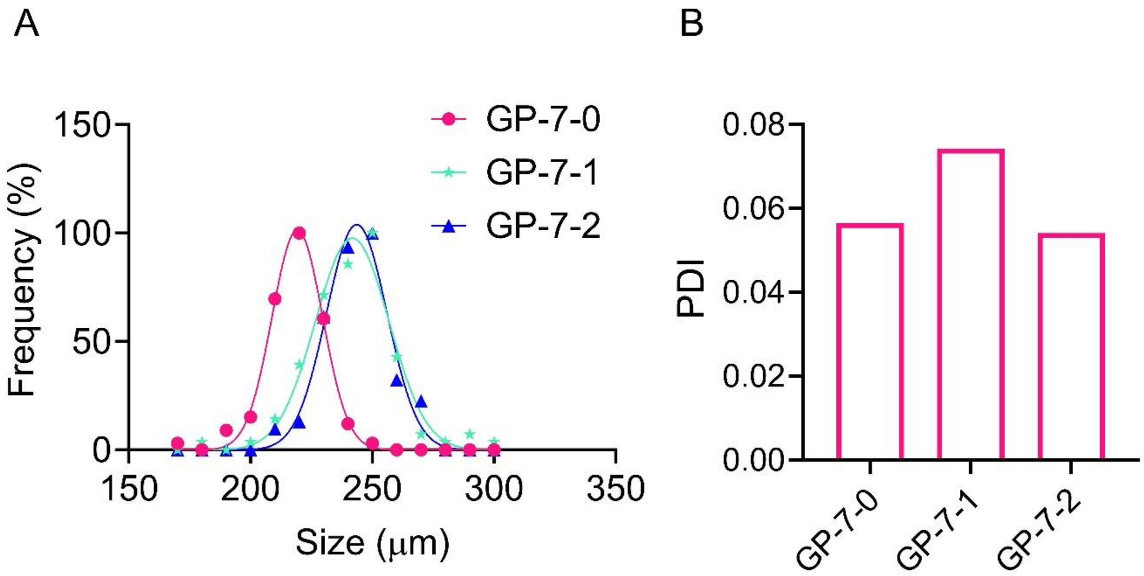

Figure 19(A) Size distribution of the fabricated microcarriers, illustrating frequency distributions for different PEDOT:PSS concentrations. A shift in size distribution is observed with increasing PEDOT:PSS content. (B) Polydispersity index (PDI) analysis, showing variations in size uniformity across different formulations. The microcarriers exhibit different degrees of polydispersity depending on PEDOT:PSS concentration (n>100).

3.4 Material Characterization

To evaluate the physicochemical and electrical properties of the fabricated GelMA-PEDOT:PSS microcarriers, a series of characterization experiments were conducted. In Figure 20(i), the swelling capacity of the microcarriers is shown over a 70-hour time frame. According to Eq. 2 and using D_{final} as D_t, GP-7-1 and GP-7-2 demonstrate significantly greater swelling capacities, both around 147.6%, whereas GP-7-0 exhibits a considerably lower value of 75.35%.

This suggests that GP-7-1 and GP-7-2 exhibit nearly twice the water absorption capacity of GP-7-0, which contrasts with the findings of several other studies which reported a decrease in swelling with the addition of PEDOT:PSS [1, 103]. However, in the study by

Wang et al. using 6% GelMA, a composition highly comparable to our own (7%), showed an increase in the swelling ratio when PEDOT:PSS content was increased from 0.15% to 0.2% (w/v) [102].

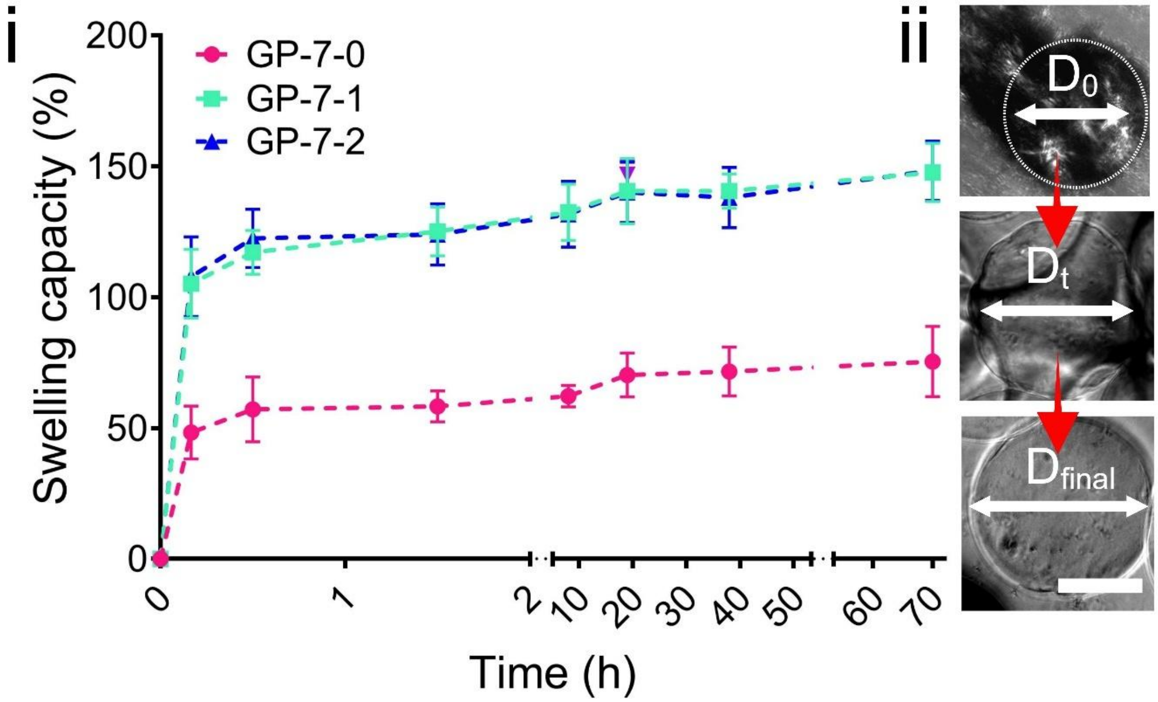

Figure 20 (i) Swelling dynamics of microcarriers with different PEDOT:PSS concentrations, measured over a 70-hour period to assess equilibrium swelling behavior. Number of replicates >4. (ii) Image of a dried GP-7-2 microcarrier with a diameter of D_0 , absorbing DMEM and swelling through time (D_t) and reach to the final diameter (D_{final}) after 70 hours. Scale bar: 100 µm.

To explain this, we need to explore PEDOT:PSS and GelMA interactions and structures. PEDOT:PSS affects GelMA crosslinking in several interconnected ways. Firstly, PEDOT:PSS imparts a darker hue to the prepolymer solution, which significantly increases light absorbance during photo-crosslinking. This can hinder light penetration to GelMA structure and thereby reduce the efficiency of GelMA crosslinking [1]. Secondly, PEDOT:PSS is an anionic polyelectrolyte that can electrostatically interact with positively charged groups (e.g., lysine residues) in the GelMA backbone. This interaction can inhibit the availability of methacryloyl groups for radical polymerization, leading to a less crosslinked network [102].

The combination of these effects- reduced photoinitiator efficiency due to higher light absorbance and chemical interference with crosslinkable groups, results in a more loosely crosslinked or diluted hydrogel structure. This structural change increases water uptake capacity, thereby enhancing the swelling ratio. Additionally, SEM imaging of PEDOT:PSS-laden GelMA hydrogels has shown a more porous network structure compared to pure GelMA, further confirming this dilution effect [102].

Moreover, our results are in line with broader trends in GelMA hydrogel behavior. It is well-documented that lower GelMA concentrations lead to higher swelling ratios due to reduced crosslinking density and increased hydrophilicity. Ghazali et al. confirms that decreasing GelMA concentration enhances swelling, which supports our interpretation that effective crosslinking density in our PEDOT:PSS-loaded GelMA was lowered, functionally behaving like a lower-concentration GelMA system [140].

In addition, the concentration of PEDOT:PSS used in our formulation was significantly higher than in many other studies, which typically explore concentrations up to 0.3% (w/v) [1, 102]. In contrast, we used a higher loading (1% (w/v) and 2% (w/v)), which may have amplified the aforementioned effects to an extent where the swelling ratio increased notably instead of decreasing. Together, these results underscore that while lower concentrations of PEDOT:PSS may tighten the hydrogel matrix through better dispersion and crosslinking interaction, higher concentrations- as used in our study- impede crosslinking and promote a more porous, hydrophilic, and ultimately more swellable network. We speculate that this effect arises from reduced crosslinking density at elevated PEDOT:PSS levels; however, the precise mechanism remains to be elucidated.

Figure 21 presents a visual comparison of crosslinked GelMA-PEDOT:PSS solutions containing varying concentrations of PEDOT:PSS, ranging from 0% to 2% (w/v). The increasing PEDOT:PSS concentration resulted in a more intense blue coloration, indicating successful incorporation of the conductive polymer within the hydrogel network. The distinct visual differences between samples reflect the tunability of hydrogel composition, which can influence both physical and electrical properties.

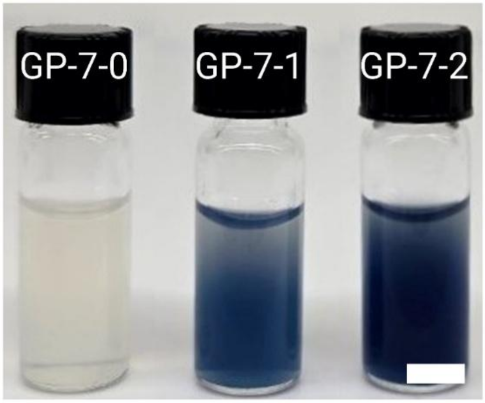

Figure 21 Visual representation of photocured GelMA-PEDOT:PSS solutions at varying PEDOT:PSS concentrations, ranging from 0% to 2%. Scale bar: 5 mm.

Figure 22 shows the four-point probe measurement setup used to determine the electrical resistance of the hydrogel sheet. The image displays four metallic probe tips in contact with the hydrogel surface, positioned under a microscope for precise alignment. In this configuration, the two outer probes are responsible for sourcing current, while the two inner probes measure the resulting voltage drop across the sample. This arrangement minimizes contact resistance and ensures accurate resistance measurements. Refer to the Experimental Section for detailed procedures and measurement parameters.

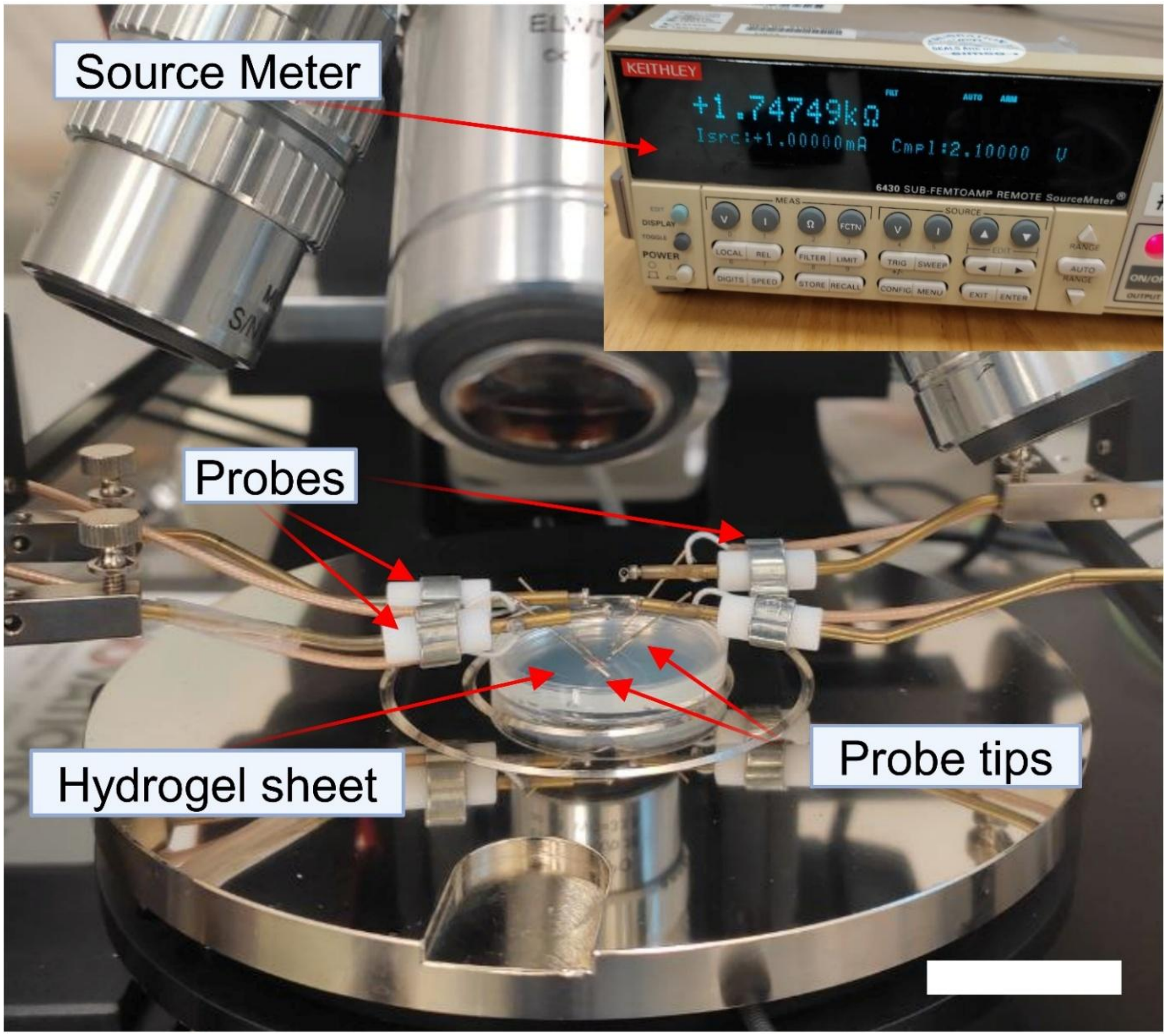

Figure 22 Image of the four-point probe measurement setup used to evaluate the resistance of crosslinked hydrogel sheets. Scale bar: 35 mm.

Figure 23 represents electrical resistance measurements of GelMA-based hydrogels with different concentrations of PEDOT:PSS, evaluated under two different applied currents: 1 mA and 10 mA. These two currents were chosen as research indicates that the optimal current range for four-point probe measurements of hydrogels was between 0.1 mA to 10 mA [141]. This range was determined based on studies showing that hydrogel conductance measurements conducted over a current range from 0.001 mA to 10 mA exhibited varying degrees of accuracy and structural integrity. At a current level of 0.01 mA, measurement repeatability was compromised due to detection noise, making it unreliable for precise conductance assessments. However, at currents above 0.1 mA, measurement consistency improved, and conductance values remained relatively stable up to 10 mA. Beyond this threshold, the hydrogel's conductivity exhibited gradual degradation, likely due to permanent structural damage caused by excessive current. Thus, the 0.1 mA to 10 mA range was identified as optimal, as it ensures repeatable conductance measurements while minimizing measurement artifacts and preventing hydrogel degradation [141]. The hydrogels tested include GelMA (7%) without PEDOT:PSS (GP-7-0), GelMA (7%) with 1% PEDOT:PSS (GP-7-1), and GelMA (7%) with 2% PEDOT:PSS (GP-7-2). In Figure 23, when the applied current was 1 mA, the resistance of GP-7-0 was the highest, measuring 13.84 ± 0.84 Ω, whereas GP-7-1 showed a significant decrease in resistance to 5.88 ± 1.17 Ω. The addition of 2% PEDOT:PSS (GP-7-2) further reduces the resistance to 2.22 ± 0.27 Ω, indicating an increase in conductivity with higher PEDOT:PSS content. When the applied current was 10 mA, a similar trend appears but with overall lower resistance values. GP-7-0 exhibits the highest resistance at 1.73 ± 0.13 Ω, while GP-7-1 shows a reduction to 1.18 ± 0.05 Ω, and GP-7-2 demonstrates the lowest resistance, 0.55 ± 0.16 Ω. The statistical comparisons confirm a significant reduction in resistance with increasing PEDOT:PSS concentration. These results demonstrate that PEDOT:PSS incorporation enhances the electrical conductivity of GelMA hydrogels, as evident from the decrease in resistance with increasing

PEDOT:PSS content. The effect is consistent at both low and high currents, though resistance values are naturally lower at higher currents [141].

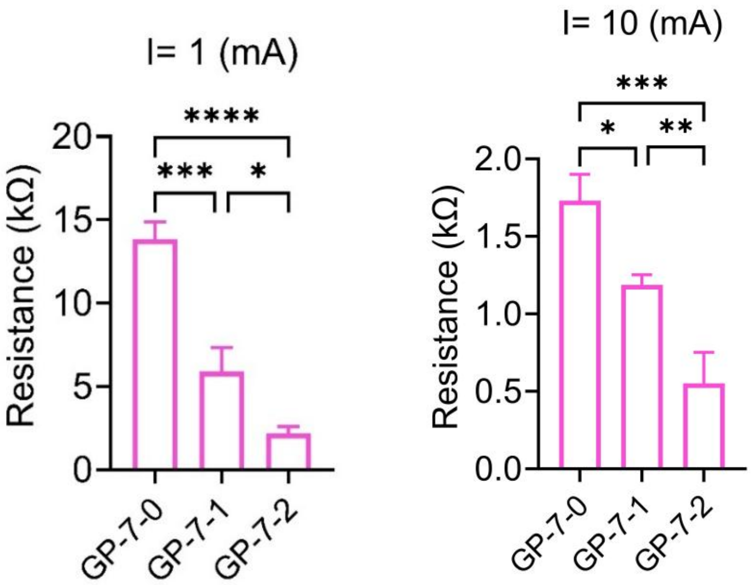

*Figure 23 Electrical resistance values of GP-7-0, GP-7-1, and GP-7-2 measured under two currents of 1 mA and 10 mA. Results presented as mean ± SD. Number of replicates= 3. Statistical analysis was done by one-way ANOVA. (*p < 0.05, **p < 0.01, ***p < 0.001, and ****p < 0.0001.)*

The electrical conductivity of skeletal muscle tissue typically ranges from 0.04 S/m to 0.5 S/m [104]. However, depending on the type of stimulation applied and the orientation of the measurement relative to muscle fibers (i.e., parallel or perpendicular), reported values can vary from 0.05 S/m up to 2.58 S/m [142, 143].

The average resistance values measured for GP-7-0, GP-7-1, and GP-7-2 were used to calculate the corresponding conductivity values at different applied currents (1 mA and 10 mA). The computed conductivity values were as follows (see Experimental Section for detailed formulations):

Table 6 Conductivity calculated from four-point probe resistance values.

Sample	Conductivity (S/m) at 1 mA	Conductivity (S/m) at 10 mA
GP-7-0	0.14	1.15
GP-7-1	0.34	1.69
GP-7-2	0.90	3.63

The conductivity values calculated for the hydrogel sheets using the four-point probe method fall within a similar range, indicating comparable conductive properties. As shown in Table 6, the electrical conductivity of the hydrogel samples increases with the addition of PEDOT:PSS. At both 1 mA and 10 mA applied currents, GP-7-0 (0% PEDOT:PSS) exhibited the lowest conductivity, while GP-7-2 (2% PEDOT:PSS) demonstrated the highest. Specifically, conductivity rose from 0.14 S/m in GP-7-0 to 0.90 S/m in GP-7-2 at 1 mA, and from 1.15 S/m to 3.63 S/m at 10 mA. These findings confirm that PEDOT:PSS effectively enhances the hydrogel's electrical performance.

3.4.1 Evaluating Viability, Attachment, and Proliferation of C2C12 Cells on Electroconductive Microcarriers

Assessing biocompatibility is crucial to ensure biomaterials support viability, cell adhesion, and proliferation. PrestoBlue viability test was performed to further investigate the cytotoxicity of the PEDOT:PSS (See Experimental Section). To evaluate initial adhesion efficiency, a cell attachment assay was performed on C2C12 cells, a key factor in biocompatibility and tissue engineering applications. Additionally, a proliferation study tracked cell growth over a 7-day period, examining whether PEDOT:PSS enhances expansion through bioelectrical interactions. A live/dead staining assay was conducted on day 7 of the cell culture process on the MCs to visualize viable (green) and non-viable (red) cells, providing insight into the cytotoxic effects of PEDOT:PSS.

First, we conducted an extraction assay to evaluate the potential cytotoxicity of PEDOT:PSS. As shown in Figure 24, the PrestoBlue assay assessed the effects of MC extracts on C2C12 cell viability over a 14-day period. Cell viability remained consistently high across all groups, with no significant differences observed at any time point.

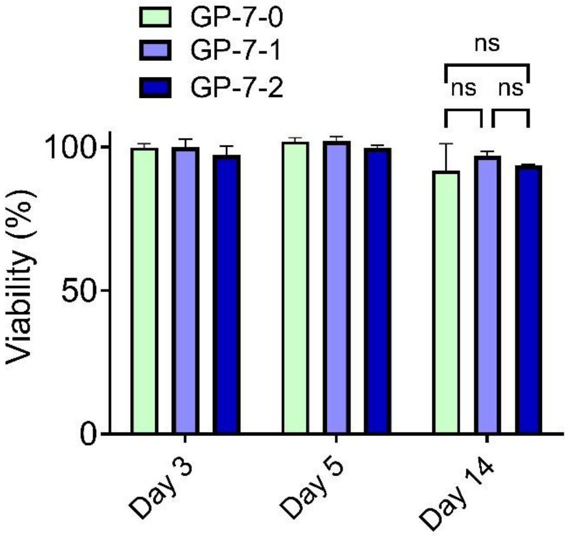

Figure 24 Cytotoxicity evaluation of the microcarriers using the PrestoBlue assay. the effect of the microcarriers' extract on C2C12 cells after 24 hours exposure. Number of replicates= 2.

Next, we investigated cell attachment efficiency, proliferation, and viability using a live/dead assay over a 7-day period with MCs seeded in a 96-well plate. Attachment efficiency was evaluated after four hours of incubation with C2C12 cells on MCs containing varying concentrations of PEDOT:PSS (Figure 25). The results indicate that attachment percentages were comparable among GP-7-0, GP-7-1, and GP-7-2 groups, with no statistically significant differences. This suggests that PEDOT:PSS, at the tested concentrations, does not significantly affect initial cell adhesion.

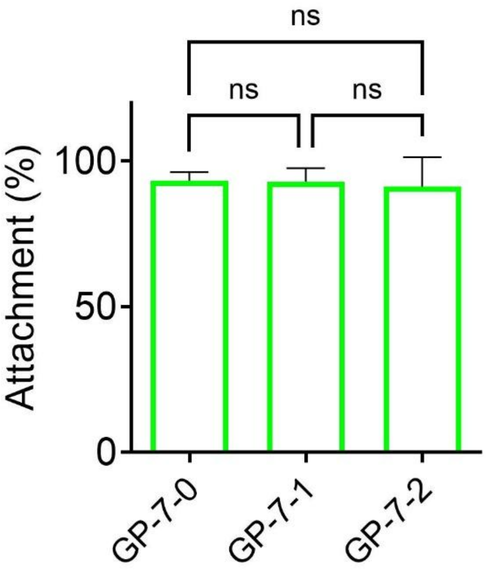

Figure 25 Cell attachment assay showing the percentage of C2C12 cells adhered to microcarriers with varying PEDOT:PSS concentrations (0%, 1%, 2%) after 4 hours of incubation. Number of replicates= 3.

Figure 26 presents the proliferation data over the 7-day period. All groups demonstrated increased proliferation over time; however, GP-7-0 exhibited significantly higher proliferation than GP-7-1 and GP-7-2 on day 7 (***p < 0.001). Proliferation rates between GP-7-1 and GP-7-2 were similar, indicating that higher concentrations of PEDOT:PSS may modestly reduce cell proliferation. This reduction correlates with an increased percentage of myogenically differentiated (MyHC+) cells, supporting the hypothesis that PEDOT:PSS promotes myoblast differentiation while limiting proliferation. This trend reflects the natural progression of muscle development, where proliferating myoblasts exit the cell cycle to undergo fusion and maturation [144-147].

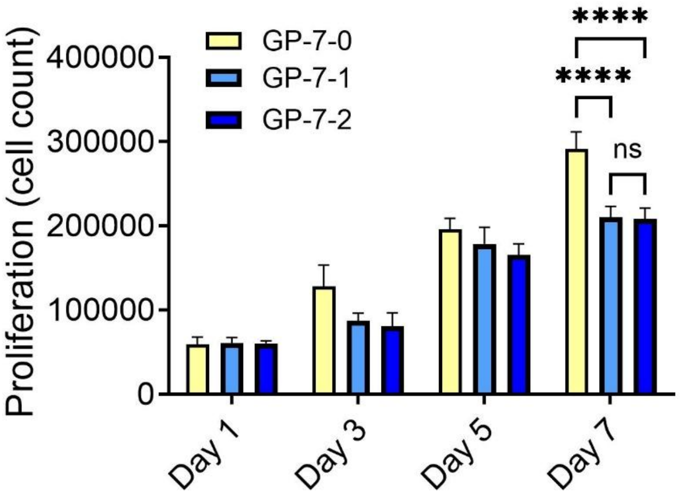

*Figure 26 Cell proliferation assay quantifying C2C12 cell growth on microcarriers with different PEDOT:PSS concentrations (0%, 1%, 2%) at days 1, 3, 5, and 7, highlighting the effect of conductivity on cell proliferation. Number of replicates= 4. Results presented as mean ± SD. Statistical analysis was done by ordinary one-way ANOVA.(ns: not significant p>0.05, ****p < 0.0001.)*

Figure 27 presents fluorescent live-dead staining images of C2C12 cells cultured on MCs with different PEDOT:PSS concentrations (GP-7-0, GP-7-1, and GP-7-2) at day 7. The green fluorescence indicates viable cells, while the merged images combine bright-field, live (green), and dead (red) staining for a comprehensive view of cell distribution and morphology. The images show high viability among all MC groups.

These findings confirm that PEDOT:PSS, at the tested concentrations, is non-cytotoxic to C2C12 cells and supports its biocompatibility. This study confirms that the integration of PEDOT:PSS does not impair C2C12 attachment; however, it negatively affects long-term cell expansion. One possible explanation is that, during muscle development, myoblasts initially proliferate before undergoing differentiation. Once committed to differentiation, they exit the cell cycle, fuse, and express myogenic markers [105, 106]. The decrease in proliferation in PEDOT:PSS-containing conditions may be directly related to the increase in differentiation, as cells shift from a growth phase to a maturation phase.

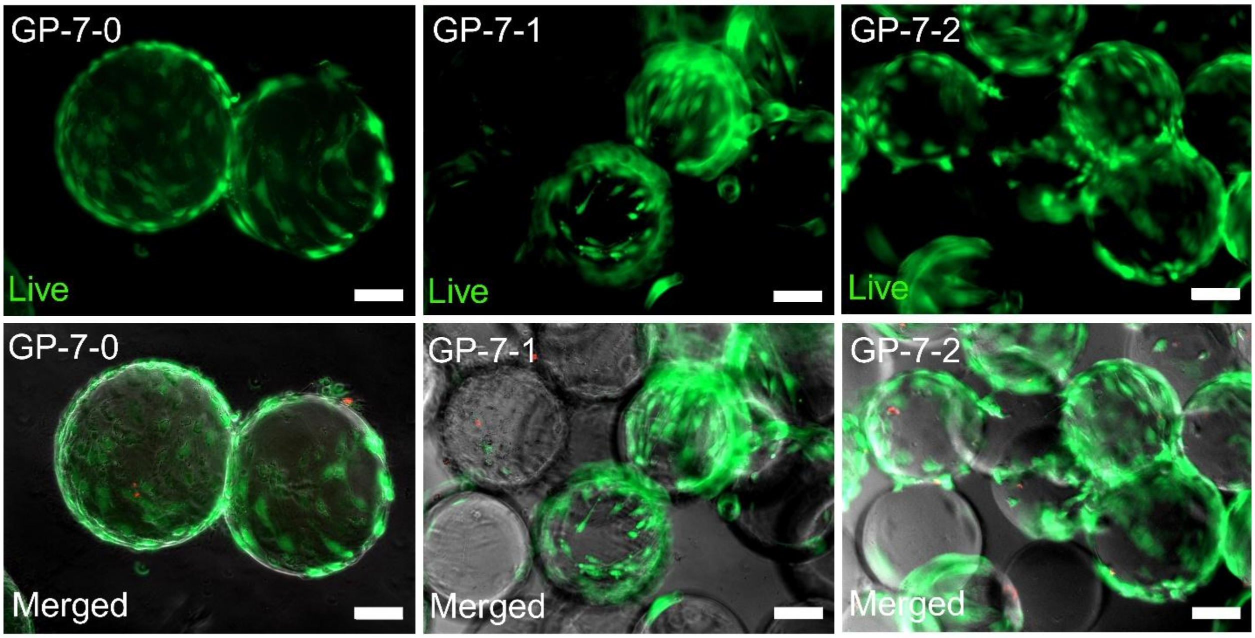

Figure 27 Fluorescent staining of C2C12 cells cultured on GP-7-0, GP-7-1, and GP-7-2 microcarriers at day 7: Live cell staining (green) and Combined Live/Dead/Bright-field imaging (live: green, dead: red, bright-field: gray). Scale bar: 100 µm.

3.4.2 Functional assessment: Impact of PEDOT:PSS on C2C12 cell morphology and myogenic differentiation

Based on the previous section, the use of PEDOT:PSS in microcarriers leads to a decrease in cell proliferation, which may be attributed to the differentiation of C2C12 cells. To investigate this hypothesis, we examined two key indicators of cell differentiation: nuclear elongation and MyHC expression. Nuclear elongation was assessed using the nuclear aspect ratio. Previous research by T. M. Watanabe et al. has demonstrated that the differentiation of C2C12 myoblasts into myotubes is associated with significant changes in nuclear morphology, particularly an increase in the nuclear aspect ratio. As C2C12 cells progress from rounded myoblasts to elongated myotubes, their nuclear aspect ratio increases [107].

This change in nuclear shape is attributed to forces acting on the nucleus during the differentiation process, indicating a reorganization of nuclear architecture [107]. The increase in nuclear aspect ratio serves as a useful morphological indicator of myogenic differentiation in C2C12 cells [108]. These alterations in nuclear morphology are part of a broader set of changes that occur during C2C12 differentiation, including chromatin remodeling and changes in histone dynamics, which collectively contribute to the determination of cell fate in muscle development [107].

To assess the impact of conductive MCs on C2C12 behavior, we conducted immunofluorescence staining of cells cultured on GelMA-PEDOT:PSS MCs with increasing concentrations of PEDOT:PSS (Figure 28). These images provide insight into cytoskeletal organization and nuclear morphology, which serve as critical markers of cellular alignment and differentiation. Actin (green) and DAPI (blue) staining revealed clear structural differences across conditions, with elongated nuclear shapes observed at higher PEDOT:PSS concentrations.

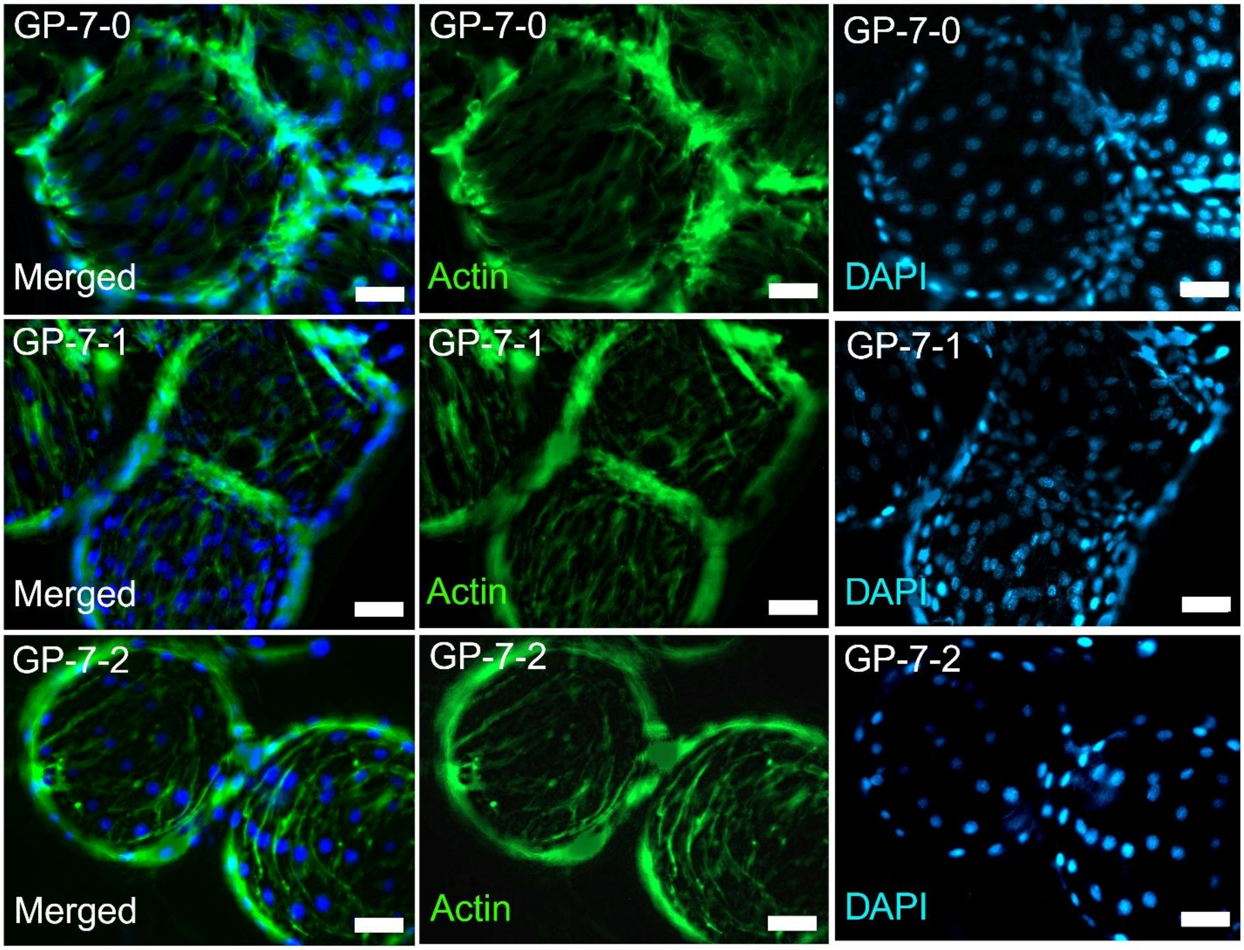

Figure 28 Immunofluorescence staining of C2C12 myoblasts cultured on GelMA-PEDOT:PSS microcarriers with varying PEDOT:PSS concentrations. On the left: Merged images of DAPI-stained nuclei (blue) and actin cytoskeleton (green), In the middle: actin staining, and on the right: DAPI staining. Scale bars: 50 μm.

Figure 29 presents a quantitative analysis of the nuclear aspect ratio, reflecting cellular elongation in response to substrate conductivity. The results demonstrate a significant increase in nuclear elongation between GP-7-0 (GelMA only, 1.41 ± 0.11) and GP-7-1 (GelMA with 1% PEDOT:PSS, 1.51 ± 0.03; $^*p < 0.05$). However, no further increase was observed at 2% PEDOT:PSS (GP-7-2, 1.51 ± 0.008), suggesting a plateau in the elongation response. Since nuclear elongation is considered a hallmark of early myogenic differentiation, these findings indicate that 1% PEDOT:PSS is sufficient to promote this phenotype, while higher concentrations do not confer additional morphological benefits.

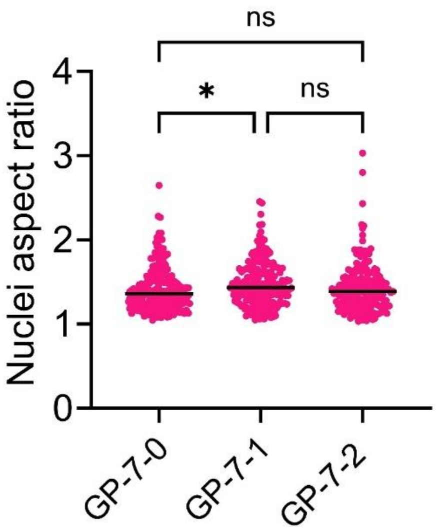

Figure 29 Results of image processing of the nuclei aspect ratio across groups done by ImageJ threshold processing (Number of replicates > 230).

In addition to morphological indicators, we assessed a molecular marker of differentiation, MyHC, as previously discussed in Section 3.3 [105, 106]. C2C12 cells were cultured on MCs for seven days at 37°C in a 5% CO_2 atmosphere. On day seven, cells were enzymatically detached and MyHC expression was analyzed via flow cytometry (Figure 30). The percentage of $MyHC^+$ cells was significantly higher in groups containing PEDOT:PSS: 24.93% ± 2.36 for GP-7-0, 52.56% ± 2.06 for GP-7-1, and 59.93% ± 6.27 for GP-7-2.

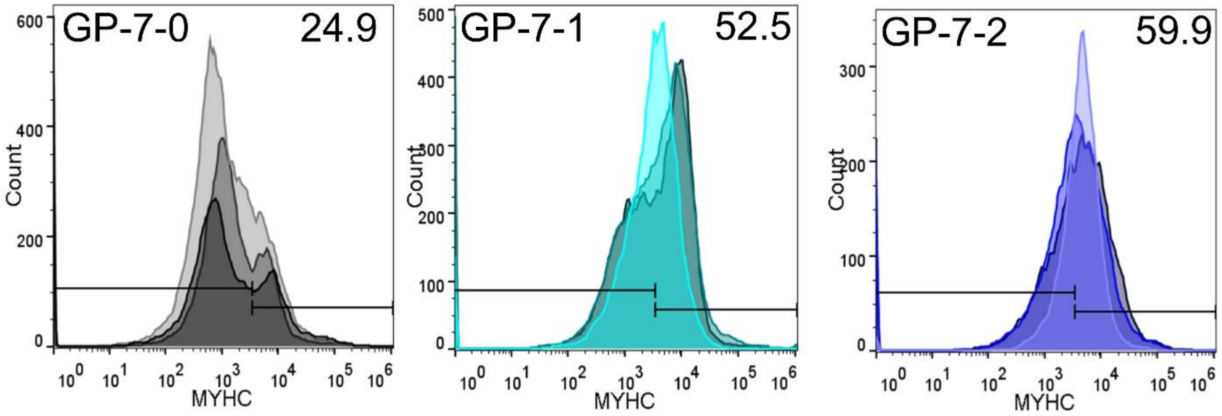

Figure 30 Flow cytometry histograms showing MyHC expression in C2C12 cells after 7 days of culture on MCs with 0% (GP-7-0), 1% (GP-7-1), and 2% (GP-7-2) PEDOT:PSS (Number of replicates = 3).

These results are summarized in the column graph in Figure 31. One-way ANOVA confirmed a statistically significant increase in MyHC$^+$ cells between 0% and 1% PEDOT:PSS (**p < 0.01), and between 0% and 2% (***p<0.001).

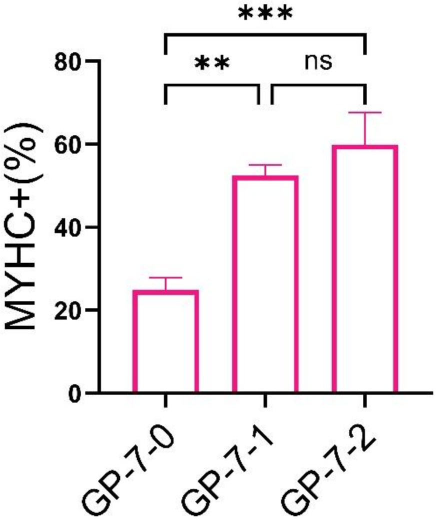

*Figure 31 Quantification of MyHC-positive (MyHC$^+$) cells from flow cytometry. A significant increase in MyHC$^+$ cells is seen with increasing the conductive material (Number of replicates = 3). Data are presented as mean ± SD. Statistical analysis was performed using one-way ANOVA. (ns = not significant $p > 0.05$, *$p < 0.05$, **$p < 0.01$, ***$p < 0.001$, ****$p < 0.0001$).*

Together, these results suggest that conductive MCs provide a favorable microenvironment for myogenic commitment by enhancing both cellular morphology and MyHC expression. Additionally, applying external electrical stimulation could further enhance myogenic differentiation and counteract the proliferation decline. Previous studies have shown that electrical stimulation synergizes with conductive biomaterials to promote muscle cell alignment, fusion, and functionality [148, 149]. These findings are consistent with previous proliferation results (Figure 26), which showed that C2C12 proliferation was significantly lower on PEDOT:PSS-containing MCs compared to the 0% PEDOT:PSS condition. The relationship between reduced proliferation and increased differentiation follows a well-documented trend in myogenic biology [105, 106], and our results confirm this relationship.

In conclusion, MCs containing PEDOT:PSS promote nuclear elongation and MyHC expression, both key indicators of myogenic differentiation. The increased nuclear aspect ratio suggests that PEDOT:PSS enhances cytoskeletal remodeling by improving conductivity and mechanical properties, thereby serving as a bioelectronic cue for myoblast differentiation. This finding aligns with previous studies demonstrating that conductive materials mimic the native muscle environment, thereby promoting cell maturation [144-147]. The findings indicate that both 1% and 2% PEDOT:PSS optimally promotes differentiation. Future research should investigate the effects of dynamic electrical stimulation to further optimize its application in muscle regeneration.

3.5 Summary and Key Findings

This study introduces a novel electroconductive microcarrier system composed of GelMA and PEDOT:PSS, engineered to support cell adhesion, differentiation, and electrical conductivity for tissue engineering applications. Using microfluidic flow focusing, monodisperse microcarriers with precise size control and tunable properties were fabricated, offering a scalable and reproducible platform for regenerative medicine.

Material analysis confirmed structural stability and enhanced conductivity, with the 2% PEDOT:PSS formulation (GP-7-2) exhibiting the lowest electrical resistance. Biocompatibility assays demonstrated high cell viability (>90%), minimal cytotoxicity, and efficient cell attachment across all formulations, with PEDOT:PSS showing no adverse impact on adhesion.

Proliferation studies revealed that GelMA-only microcarriers (GP-7-0) supported higher cell growth, while PEDOT:PSS-containing variants (GP-7-1 and GP-7-2) showed reduced proliferation over time. This decline corresponded with a higher percentage of MyHC$^+$ cells, indicating that PEDOT:PSS promotes myogenic differentiation at the expense of continued cell expansion- paralleling natural muscle development where cells exit the cycle to fuse and mature.

Differentiation assays confirmed a significant increase in MyHC expression with PEDOT:PSS, although no notable difference was observed between 1% and 2% concentrations. Immunofluorescence analysis further supported these findings, showing increased nuclear elongation in PEDOT:PSS groups-an indicator of myogenic differentiation- without significant differences between concentrations.

While PEDOT:PSS limits proliferation, it enhances differentiation. External electrical stimulation could further promote differentiation and mitigate reduced proliferation. Prior studies suggest that electrical cues synergize with conductive materials to improve muscle cell alignment, fusion, and function.

Future work should explore the impact of dynamic electrical stimulation on myotube formation, contractility, and gene expression, along with in vivo assessments to validate biocompatibility, degradation, and integration within living tissues.

Overall, GelMA-PEDOT:PSS MCs represent a promising platform for conductive tissue engineering, particularly in skeletal muscle, cardiac, and neural regeneration. This work contributes to the advancement of bioelectronic medicine and next-generation biomaterials designed to guide functional tissue repair and regeneration.

4 Chapter 4: Conclusion and Future Work

4.1 Conclusion

This thesis explored the development of electroconductive microcarriers designed for skeletal muscle tissue engineering using two complementary conductive strategies- ionic conductivity via bio-ionic liquids (BILs) and electrical conductivity via PEDOT:PSS. The study aimed to fabricate monodisperse, biocompatible microcarriers using a microfluidic flow focusing technique and to assess their physical, electrical, and biological properties in the context of supporting C2C12 myoblast adhesion, proliferation, and differentiation. The research contributes to addressing a major gap in traditional microcarrier systems, which typically lack electrical functionality and therefore fail to replicate the electrophysiological environment of excitable tissues.

In Sections 2.1 and 3.1, the rationale for selecting Gelatin Methacryloyl (GelMA) as the base material was established. GelMA offers several advantages, including tunable mechanical properties, excellent biocompatibility, enzymatic degradability, and functional groups for chemical modification. These properties make GelMA ideal for constructing injectable, photo-crosslinkable microcarriers that can support dynamic cell–material interactions. The incorporation of choline-based BILs and PEDOT:PSS into GelMA was introduced to provide ionic and electronic conductivity, respectively, mimicking the natural ionic flux and membrane potentials found in muscle and nerve tissues.

Sections 2.2 and 3.2 detailed the fabrication of microcarriers using a microfluidic flow focusing platform, which enabled the generation of monodisperse hydrogel particles with consistent geometry. The advantage of this method over conventional emulsification techniques lies in its high reproducibility, tunability, and scalability. Droplets were photo-crosslinked downstream to form hydrogel microcarriers, and their sizes were characterized by brightfield microscopy, confirming the successful formation of spherical particles in the 200–300 µm range. This section also introduced the different formulations tested, ranging from 1% to 5% BIL and 0.1% to 2% PEDOT:PSS.

In Sections 2.2.6 and 3.2.6, the physical properties of the microcarriers were characterized, while Sections 2.2.7 and 3.2.7–3.2.8 focused on their electrical characterization. Swelling tests revealed that increasing concentrations of BIL and PEDOT:PSS reduced the swelling capacity, indicating increased crosslinking density and stability of the hydrogel networks. Conductivity measurements showed a clear trend of enhanced electrical performance with increasing conductive additive concentrations. Specifically, GelMA-BIL hydrogels containing 5% BIL (GB-7-5) reached a conductivity of 0.663 S/m (Section 2.3.2), while the GelMA-PEDOT:PSS microcarriers with 2% polymer (GP-7-2) exhibited a maximum conductivity of 0.90 S/m at 1 mA and 3.63 S/m at 10 mA, with the lowest electrical resistance measured at 0.55 ± 0.16 KΩ (Section 3.4.1). These results confirmed that both BIL and PEDOT:PSS significantly enhanced the electroactive properties of the GelMA matrix, though through distinct conduction mechanisms—ionic vs. electronic.

Section 2.2.9 and 3.2.10 reported the biocompatibility and cytotoxicity results. Both the BIL and PEDOT:PSS microcarriers demonstrated excellent cell viability, with trypan blue and live/dead staining indicating over 85% viability across all tested formulations. Importantly, there was no statistical evidence of cytotoxicity, confirming that both conductive additives were safely integrated into the GelMA matrix. Section 2.2.11 and 3.2.12 discussed cell adhesion and proliferation, showing that higher conductivity correlated with enhanced C2C12 attachment within 4 hours post-seeding. Proliferation assays further supported this finding, as conductive microcarriers demonstrated a consistent increase in cell number over 7 days, with the PEDOT:PSS 2% and BIL 5% groups showing the highest proliferation rates.

Cell morphology was addressed in Section 2.2.12 and 3.2.13. Immunofluorescence imaging of F-actin and nuclei revealed that cells cultured on conductive microcarriers exhibited more elongated nuclei compared to the non-conductive control. These structural changes are characteristic of early myogenic commitment and reflect the role of conductivity in directing cell morphology. In Section 2.2.13 and 3.2.14, functional differentiation was assessed through Myosin Heavy Chain (MyHC) expression, a marker of mature muscle phenotype. Flow cytometry results showed a significant upregulation of MyHC in conductive microcarriers, with the GP-7-2 and GB-7-5 groups exhibiting up to a 1.5-fold increase in MyHC+ cells relative to controls, validating the hypothesis that electroconductive environments promote myogenic differentiation.

Collectively, this thesis demonstrates the successful development and validation of a dual-platform electroconductive microcarrier system. Both ionic and electronic conductive strategies yielded functional benefits, but each offered unique advantages. The BIL-based microcarriers provided softness, transparency, and ionic signaling aligned with natural physiological processes, without the need for solid conductive fillers. This system is ideal for interfacing with soft tissues where ion-mediated bioelectrical activity is dominant. In contrast, PEDOT:PSS-based microcarriers offered stable, robust electronic conductivity, structural integrity, and compatibility with external bioelectronic systems, making them well-suited for applications involving electrical stimulation or device integration.

The fabrication approach using microfluidic flow focusing was central to the success of this study. As shown throughout Chapters 2 and 3, the method enabled precise control over size, composition, and geometry, all of which contributed to reproducible results and reliable biological performance. This platform is highly adaptable and can be extended to a variety of biomaterial systems and cell types.

From a biological perspective, the findings underscore the critical role of electrical cues in regulating cell behavior in tissue engineering. By demonstrating that microcarrier conductivity enhances not just viability and proliferation but also myogenic differentiation, this work lays the foundation for the use of conductive microcarriers as scalable platforms for cell therapy, tissue regeneration, and bioelectronic interfaces. The modularity of the system makes it well-suited for injection-based delivery, dynamic stimulation, and integration into 3D bioreactor systems.

In conclusion, this thesis provides a robust, reproducible, and biologically effective approach for engineering electroconductive microcarriers using GelMA, BIL, and PEDOT:PSS. The dual-mode conductive strategy allows for tailoring materials to specific tissue engineering needs-whether favoring soft ionic communication or robust electronic signal transmission. The work presents a significant advancement in microcarrier-based platforms and opens new directions for future studies in electroactive tissue engineering, especially when combined with in vitro electrical stimulation or in vivo delivery in muscle regeneration models.

4.1.1 Comparative Insights: Ionic- vs. Electrical-Conductive Microcarriers

The two studies presented in Chapters 2 (GelMA-BIL) and 3 (GelMA-PEDOT:PSS) collectively demonstrate that both ionic and electronic strategies can be seamlessly integrated into a monodisperse GelMA microcarrier platform, yet they modulate the cell/material interface in distinct, sometimes complementary, ways.

4.1.1.1 Material architecture and baseline physicochemical properties

Neither additive compromised droplet formation: both GelMA-BIL and GelMA-PEDOT:PSS spheres retained tight size distributions with PDI < 0.1, confirming that microfluidic flow-focusing is tolerant to either solute chemistry. Interestingly, the additives produced opposite water-handling behaviours. BIL suppressed swelling to <7 % (vs. 23 % for GelMA alone), whereas PEDOT:PSS nearly doubled water uptake to ~148 % , a divergence that could be exploited to match tissue hydration needs.

4.1.1.2 Electrical performance

As expected, PEDOT:PSS delivered the higher absolute conductivity (0.90 $\mathrm{S\,m^{-1}}$ at 1 mA; 3.63 $\mathrm{S\,m^{-1}}$ at 10 mA for 2 % w/v), while BIL provided a gentler ionic window topping at 0.663 $\mathrm{S\,m^{-1}}$ for 5 % w/v. Notably, the BIL range already overlaps native skeletal-muscle conductivity (0.04–0.5 $\mathrm{S\,m^{-1}}$), whereas the PEDOT:PSS range extends into values useful for low-impedance bioelectronic readouts. Thus, ionic GelMA-BIL carriers may suit low-voltage physiological signalling, whereas electronic GelMA-PEDOT:PSS carriers can support higher-fidelity stimulation or sensing.

4.1.1.3 Biocompatibility trends

Live/dead, PrestoBlue and extract tests confirmed > 85 % viability for both systems, with no leachable-toxicity detected for PEDOT:PSS over 14 days. Early adhesion was comparable across all formulations, but growth kinetics diverged: Both BIL and PEDOT:PSS MCs showed a modest proliferation slowdown by day 7. This suggests that electroconductive MCs bias cells toward exit from cycle and maturation.

4.1.1.4 Myogenic differentiation and functional read-outs

Both additives promoted hallmark cues of myogenesis, nuclear elongation and MyHC expression, but with different dose-response ceilings. BIL raised the nuclear aspect ratio from 1.30 → 1.49 and lifted MyHC$^+$ cells ~1.5-fold, plateauing beyond 2.5 % w/v. PEDOT:PSS induced a sharper jump: MyHC$^+$ cells rose from 25 % (0 %) to 53 % (1 %) and 60 % (2 %), again with a plateau above 1 % w/v, while nuclear elongation stabilised at ~1.51. Taken together, ionic conduction was sufficient to trigger early differentiation cues, but electronic conduction delivered a larger absolute pool of mature (MyHC$^+$) myotubes, albeit at the expense of proliferation.

4.1.1.5 Design implications

These findings position the two microcarrier chemistries as complementary tools along the myogenic pipeline. GelMA-BIL spheres are well-matched to bioreactor expansion stages where high viability and moderate conductivity guide early lineage commitment without throttling growth. GelMA-PEDOT:PSS spheres excel as “maturation boosters,” providing higher conductivity and electronic coupling for late-stage fusion or integration with exogenous pacing electrodes.

By juxtaposing the ionic and electronic routes, this work underscores how tuning the nature—not just the magnitude—of conductivity unlocks orthogonal levers over muscle-cell fate, offering a rational framework for selecting (or stacking) conductive additives to meet specific manufacturing or therapeutic endpoints.

4.2 Future Work

This study has laid the groundwork for using electroconductive GelMA-based microcarriers to enhance skeletal muscle tissue engineering. The incorporation of BILs and PEDOT:PSS showed promising results in improving cell adhesion and myogenic differentiation. Building on this, several future directions are proposed to explore the full potential of these materials and further optimize their application in scalable tissue engineering systems.

4.2.1 Refining Conductivity Levels and Cellular Response

Although the results clearly indicated a positive correlation between conductivity and cell performance, future studies should determine the optimal conductivity range for specific biological outcomes. Microcarriers with finer gradations of BIL or PEDOT:PSS concentrations can be fabricated and tested to better understand the relationship between electrical environment and cell behavior. Key areas of investigation include:

- Determining the threshold conductivity required to trigger enhanced myogenic differentiation.
- Mapping dose-response relationships between conductivity and cell morphology using live-cell imaging.

- Using impedance spectroscopy and electrical modeling to predict in vitro performance.

4.2.2 Coupling with Electrical Stimulation Platforms

To mimic physiological environments more closely, the next logical step is to integrate these conductive microcarriers with dynamic electrical stimulation systems. This could significantly enhance the functional maturation of excitable tissues like skeletal muscle and heart. Future work could include:

- Designing custom bioreactor setups for uniform electrical field exposure.
- Testing stimulation frequencies and voltages that mimic muscle contraction or cardiac pacing.
- Assessing downstream effects such as contractile force generation and alignment of myotubes.

4.2.3 Expanding to Other Cell Types and Co-Culture Models

The current study focused on C2C12 myoblasts, but the conductive microcarriers could benefit a broader range of cell types and tissues. Future research can explore:

- Seeding neural stem cells or cardiomyocytes to evaluate cross-platform compatibility.
- Developing co-culture systems (e.g., muscle + endothelial cells) to model vascularized muscle tissue.
- Investigating electrical influence on intercellular communication and ECM deposition.

4.2.4 In Vivo Validation and Degradation Analysis

To support clinical translation, in vivo studies are necessary to assess safety, bio-integration, and degradation behavior. Suggested steps include:

- Implanting microcarriers into skeletal muscle injury models.
- Using imaging (MRI, ultrasound) and histology to evaluate tissue regeneration and immune response.
- Monitoring degradation rate and metabolite clearance over time.

4.2.5 Smart Harvesting and Delivery Approaches

Conductive microcarriers may provide novel methods for cell harvesting or delivery due to their electroactive nature. Future directions:

- Explore electrophoretic harvesting as a gentle, enzyme-free method for detaching cells.
- Test injectability and retention of microcarriers in soft tissue.
- Evaluate the ability of microcarriers to act as both scaffolds and delivery vehicles in regenerative applications.

4.2.6 Real-Time Biosensing Integration

Lastly, incorporating biosensing features could elevate these microcarriers into smart platforms. By enabling real-time feedback on culture conditions, they could enhance quality control and consistency in manufacturing environments. Future possibilities include:

- Embedding sensing modules to detect pH, oxygen, or glucose changes.
- Using conductivity shifts to infer cell density or viability.
- Building automated feedback loops for adaptive cell culture control in bioreactors.

References

[1] A. R. Spencer, A. Primbetova, A. N. Koppes, R. A. Koppes, H. Fenniri, and N. Annabi, "Electroconductive Gelatin Methacryloyl-PEDOT:PSS Composite Hydrogels: Design, Synthesis, and Properties," ACS Biomaterials Science & Engineering, vol. 4, no. 5, pp. 1558-1567, 2018/05/14 2018, doi: 10.1021/acsbiomaterials.8b00135.

[2] V. Krishnadoss et al., "Programmable bio-ionic liquid functionalized hydrogels for in situ 3D bioprinting of electronics at the tissue interface," Materials Today Advances, vol. 17, p. 100352, 2023.

[3] L. Huang, A. M. E. Abdalla, L. A.-O. Xiao, and G. Yang, "Biopolymer-Based Microcarriers for Three-Dimensional Cell Culture and Engineered Tissue Formation. LID - 10.3390/ijms21051895 [doi] LID - 1895," (in eng), no. 1422-0067 (Electronic), 2020.

[4] L. Y. Sun, Y.-S. Lin Sz Fau - Li, H.-J. Li Ys Fau - Harn, T.-W. Harn Hj Fau - Chiou, and T. W. Chiou, "Functional cells cultured on microcarriers for use in regenerative medicine research," (in eng), no. 1555-3892 (Electronic), 2011.

[5] S.-L. Ding et al., "Microcarriers in application for cartilage tissue engineering: Recent progress and challenges," Bioactive Materials, vol. 17, pp. 81-108, 2022/11/01/ 2022, doi: https://doi.org/10.1016/j.bioactmat.2022.01.033.

[6] X.-Y. Chen, J.-Y. Chen, X.-M. Tong, J.-G. Mei, Y.-F. Chen, and X.-Z. Mou, "Recent advances in the use of microcarriers for cell cultures and their ex vivo and in vivo applications," Biotechnology Letters, vol. 42, no. 1, pp. 1-10, 2020/01/01 2020, doi: 10.1007/s10529-019-02738-7.

[7] H. K. Handral, T. A. Wyrobnik, and A. T.-L. Lam, "Emerging Trends in Biodegradable Microcarriers for Therapeutic Applications," Polymers, vol. 15, no. 6, p. 1487, 2023.

[8] W. O. Twal et al., "Cellularized microcarriers as adhesive building blocks for fabrication of tubular tissue constructs," (in eng), no. 1573-9686 (Electronic), 2014.

[9] J. Wang et al., "Microfluidic generation of porous microcarriers for three-dimensional cell culture," ACS applied materials & interfaces, vol. 7, no. 49, pp. 27035-27039, 2015.

[10] A. Seyfoori, E. Askari, M. Razzaghi, M. H. Karimi, and M. Akbari, "High-density culturing of the dermal fibroblast cells on hydrogel-based soft microcarriers for cell therapy application," Chemical Engineering Journal, vol. 494, p. 152784, 2024/08/15/ 2024, doi: https://doi.org/10.1016/j.cej.2024.152784.

[11] O. A.-O. X. Kochetkova, T. A.-O. Demina, and O. A.-O. Antonova, "Universal Microcarriers Based on Natural and Synthetic Polymers for Co-Delivery of Hydrophilic and Hydrophobic Compounds. LID - 10.3390/polym14050931 [doi] LID - 931," (in eng), no. 2073-4360 (Electronic), 2022.

[12] Y. Liu, Z. Chen, and J. Xu, "Recent advances in the microfluidic generation of shape-controllable hydrogel microparticles and their applications," Green Chemical Engineering, vol. 5, no. 1, pp. 16-30, 2024/03/01/ 2024, doi: https://doi.org/10.1016/j.gce.2023.02.002.

[13] A. S. Caldwell, B. A. Aguado, and K. S. Anseth, "Designing Microgels for Cell Culture and Controlled Assembly of Tissue Microenvironments," Advanced Functional Materials, vol. 30, no. 37, p. 1907670, 2020, doi: https://doi.org/10.1002/adfm.201907670.

[14] D.-Y. Kim, S. H. Jin, S.-G. Jeong, B. Lee, K.-K. Kang, and C.-S. Lee, "Microfluidic preparation of monodisperse polymeric microspheres coated with silica nanoparticles," Scientific Reports, vol. 8, no. 1, p. 8525, 2018/06/04 2018, doi: 10.1038/s41598-018-26829-z.

[15] X. Yuan, A.-C. Tsai, I. Farrance, J. A. Rowley, and T. Ma, "Aggregation of culture expanded human mesenchymal stem cells in microcarrier-based bioreactor," Biochemical Engineering Journal, vol. 131, pp. 39-46, 2018/03/15/ 2018, doi: https://doi.org/10.1016/j.bej.2017.12.011.

[16] B. Koh et al., "Three dimensional microcarrier system in mesenchymal stem cell culture: a systematic review," Cell & Bioscience, vol. 10, no. 1, p. 75, 2020/06/03 2020, doi: 10.1186/s13578-020-00438-8.

[17] A. W. Nienow, Q. A. Rafiq, K. Coopman, and C. J. Hewitt, "A potentially scalable method for the harvesting of hMSCs from microcarriers," Biochemical Engineering Journal, vol. 85, pp. 79-88, 2014/04/15/ 2014, doi: https://doi.org/10.1016/j.bej.2014.02.005.

[18] H. Tavassoli, S. N. Alhosseini, A. Tay, P. P. Y. Chan, S. K. Weng Oh, and M. E. Warkiani, "Large-scale production of stem cells utilizing microcarriers: A biomaterials engineering perspective from academic research to commercialized products," Biomaterials, vol. 181, pp. 333-346, 2018/10/01/ 2018, doi: https://doi.org/10.1016/j.biomaterials.2018.07.016.

[19] E. A.-O. Ng, M. Wang, S. H. Neo, C. A. Tee, C. H. Chen, and K. J. Van Vliet, "Dissolvable Gelatin-Based Microcarriers Generated through Droplet Microfluidics for Expansion and Culture of Mesenchymal Stromal Cells," (in eng), no. 1860-7314 (Electronic), 2021.

[20] T. Gao et al., "A scalable culture system incorporating microcarrier for specialised mesenchymal stem cells from human embryonic stem cells," (in eng), no. 2590-0064 (Electronic), 2023.

[21] S. M. H. Dabiri et al., "Multifunctional Thermoresponsive Microcarriers for High-Throughput Cell Culture and Enzyme-Free Cell Harvesting," Small, Article vol. 17, no. 44, 2021, Art no. 2103192, doi: 10.1002/smll.202103192.

[22] P. H. Jakob et al., "A 3-D cell culture system to study epithelia functions using microcarriers," Cytotechnology, vol. 68, pp. 1813-1825, 2016.

[23] S. C. P. Norris, N. S. Kawecki, A. R. Davis, K. K. Chen, and A. C. Rowat, "Emulsion-templated microparticles with tunable stiffness and topology: Applications as edible microcarriers for cultured meat," Biomaterials, vol. 287, p. 121669, 2022/08/01/ 2022, doi: https://doi.org/10.1016/j.biomaterials.2022.121669.

[24] C. Shao, J. Chi, L. Shang, Q. Fan, and F. Ye, "Droplet microfluidics-based biomedical microcarriers," Acta Biomaterialia, vol. 138, pp. 21-33, 2022/01/15/ 2022, doi: https://doi.org/10.1016/j.actbio.2021.10.037.

[25] T. Alkayyali, T. Cameron, B. Haltli, R. G. Kerr, and A. Ahmadi, "Microfluidic and cross-linking methods for encapsulation of living cells and bacteria - A review," Analytica Chimica Acta, vol. 1053, pp. 1-21, 2019/04/11/ 2019, doi: https://doi.org/10.1016/j.aca.2018.12.056.

[26] G. M. Whitesides, "The origins and the future of microfluidics," nature, vol. 442, no. 7101, pp. 368-373, 2006.

[27] Z. Mahmoudi et al., "Promoted chondrogenesis of hMCSs with controlled release of TGF-β3 via microfluidics synthesized alginate nanogels," Carbohydrate Polymers, vol. 229, p. 115551, 2020/02/01/ 2020, doi: https://doi.org/10.1016/j.carbpol.2019.115551.

[28] S. Battat, D. A. Weitz, and G. M. Whitesides, "An outlook on microfluidics: the promise and the challenge," Lab on a Chip, 10.1039/D1LC00731A vol. 22, no. 3, pp. 530-536, 2022, doi: 10.1039/D1LC00731A.

[29] H. Shieh, M. Saadatmand, M. Eskandari, and D. Bastani, "Microfluidic on-chip production of microgels using combined geometries," Scientific Reports, vol. 11, no. 1, p. 1565, 2021/01/15 2021, doi: 10.1038/s41598-021-81214-7.

[30] Z. Chen et al., "Advanced microfluidic devices for fabricating multi-structural hydrogel microsphere," Exploration, vol. 1, no. 3, p. 20210036, 2021, doi: https://doi.org/10.1002/EXP.20210036.

[31] Z. Wei, S. Wang, J. Hirvonen, H. A.-O. Santos, and W. Li, "Microfluidics Fabrication of Micrometer-Sized Hydrogels with Precisely Controlled Geometries for Biomedical Applications," (in eng), no. 2192-2659 (Electronic), 2022.

[32] W. A.-O. Lai and W. T. Wong, "Property-Tuneable Microgels Fabricated by Using Flow-Focusing Microfluidic Geometry for Bioactive Agent Delivery. LID - 10.3390/pharmaceutics13060787 [doi] LID - 787," (in eng), no. 1999-4923 (Print), 2021.

[33] K. O. Rojek, M. Ćwiklińska, J. Kuczak, and J. Guzowski, "Microfluidic Formulation of Topological Hydrogels for Microtissue Engineering," Chemical Reviews, vol. 122, no. 22, pp. 16839-16909, 2022/11/23 2022, doi: 10.1021/acs.chemrev.1c00798.

[34] R. D. Pedde, H. Li, C. H. Borchers, and M. Akbari, "Microfluidic-Mass Spectrometry Interfaces for Translational Proteomics," Trends in Biotechnology, vol. 35, no. 10, pp. 954-970, 2017/10/01/ 2017, doi: https://doi.org/10.1016/j.tibtech.2017.06.006.

[35] A. V. Nielsen, M. J. Beauchamp, G. P. Nordin, and A. T. Woolley, "3D printed microfluidics," Annual Review of Analytical Chemistry, vol. 13, no. 1, pp. 45-65, 2020.

[36] X. Guo et al., "Application of conductive polymer hydrogels in flexible electronics," Journal of Polymer Science, vol. 60, no. 18, pp. 2635-2662, 2022.

[37] B. Guo, Z. Ma, L. Pan, and Y. Shi, "Properties of conductive polymer hydrogels and their application in sensors," Journal of Polymer Science Part B: Polymer Physics, vol. 57, no. 23, pp. 1606-1621, 2019, doi: https://doi.org/10.1002/polb.24899.

[38] R. Eivazzadeh-Keihan et al., "Applications of carbon-based conductive nanomaterials in biosensors," Chemical Engineering Journal, vol. 442, p. 136183, 2022/08/15/ 2022, doi: https://doi.org/10.1016/j.cej.2022.136183.

[39] L. Wang, Y. Wu, T. Hu, B. Guo, and P. X. Ma, "Electrospun conductive nanofibrous scaffolds for engineering cardiac tissue and 3D bioactuators," Acta biomaterialia, vol. 59, pp. 68-81, 2017.

[40] M.-C. Chen, Y.-C. Sun, and Y.-H. Chen, "Electrically conductive nanofibers with highly oriented structures and their potential application in skeletal muscle tissue engineering," Acta biomaterialia, vol. 9, no. 3, pp. 5562-5572, 2013.

[41] E. Holt, P. Lunde, O. Sejersted, and G. Christensen, "Electrical stimulation of adult rat cardiomyocytes in culture improves contractile properties and is associated with altered calcium handling," Basic research in cardiology, vol. 92, pp. 289-298, 1997.

[42] P. Baei, S. Jalili-Firoozinezhad, S. Rajabi-Zeleti, M. Tafazzoli-Shadpour, H. Baharvand, and N. Aghdami, "Electrically conductive gold nanoparticle-chitosan thermosensitive hydrogels for cardiac tissue engineering," Materials Science and Engineering: C, vol. 63, pp. 131-141, 2016/06/01/ 2016, doi: https://doi.org/10.1016/j.msec.2016.02.056.

[43] A. Navaei, H. Saini, W. Christenson, R. T. Sullivan, R. Ros, and M. Nikkhah, "Gold nanorod-incorporated gelatin-based conductive hydrogels for engineering cardiac tissue constructs," Acta Biomaterialia, vol. 41, pp. 133-146, 2016/09/01/ 2016, doi: https://doi.org/10.1016/j.actbio.2016.05.027.

[44] R. Dong, P. X. Ma, and B. Guo, "Conductive biomaterials for muscle tissue engineering," Biomaterials, vol. 229, p. 119584, 2020/01/01/ 2020, doi: https://doi.org/10.1016/j.biomaterials.2019.119584.

[45] T. Hu et al., "Micropatterned, electroactive, and biodegradable poly (glycerol sebacate)-aniline trimer elastomer for cardiac tissue engineering," Chemical Engineering Journal, vol. 366, pp. 208-222, 2019.

[46] R. Dong, X. Zhao, B. Guo, and P. X. Ma, "Biocompatible Elastic Conductive Films Significantly Enhanced Myogenic Differentiation of Myoblast for Skeletal Muscle Regeneration," Biomacromolecules, vol. 18, no. 9, pp. 2808-2819, 2017/09/11 2017, doi: 10.1021/acs.biomac.7b00749.

[47] Z. Zhang, X. Zhao, C. Wang, Y. Huang, Y. Han, and B. Guo, "Injectable conductive micro-cryogel as a muscle stem cell carrier improves myogenic proliferation, differentiation and in situ skeletal muscle regeneration," Acta Biomaterialia, vol. 151, pp. 197-209, 2022/10/01/ 2022, doi: https://doi.org/10.1016/j.actbio.2022.08.036.

[48] S. Ostrovidov et al., "Gelatin–polyaniline composite nanofibers enhanced excitation–contraction coupling system maturation in myotubes," ACS applied materials & interfaces, vol. 9, no. 49, pp. 42444-42458, 2017.

[49] Z. Deng et al., "Stretchable degradable and electroactive shape memory copolymers with tunable recovery temperature enhance myogenic differentiation," Acta biomaterialia, vol. 46, pp. 234-244, 2016.

[50] Y. Wu, L. Wang, B. Guo, Y. Shao, and P. X. Ma, "Electroactive biodegradable polyurethane significantly enhanced Schwann cells myelin gene expression and neurotrophin secretion for peripheral nerve tissue engineering," Biomaterials, vol. 87, pp. 18-31, 2016.

[51] M. Kabiri et al., "Cytocompatibility of a conductive nanofibrous carbon nanotube/poly (L-Lactic acid) composite scaffold intended for nerve tissue engineering," EXCLI journal, vol. 14, p. 851, 2015.

[52] R. Guo et al., "Accelerating bioelectric functional development of neural stem cells by graphene coupling: implications for neural interfacing with conductive materials," Biomaterials, vol. 106, pp. 193-204, 2016.

[53] M. Tang, Q. Song, N. Li, Z. Jiang, R. Huang, and G. Cheng, "Enhancement of electrical signaling in neural networks on graphene films," Biomaterials, vol. 34, no. 27, pp. 6402-6411, 2013.

[54] M. Ma et al., "Injectable biomimetic shellfish macromolecule conductive microcarriers loaded with adipose-derived stem cells for nerve repair in vivo," Applied Materials Today, vol. 25, p. 101195, 2021/12/01/ 2021, doi: https://doi.org/10.1016/j.apmt.2021.101195.

[55] J. W. Nichol, S. T. Koshy, H. Bae, C. M. Hwang, S. Yamanlar, and A. Khademhosseini, "Cell-laden microengineered gelatin methacrylate hydrogels," Biomaterials, vol. 31, no. 21, pp. 5536-5544, 2010/07/01/ 2010, doi: https://doi.org/10.1016/j.biomaterials.2010.03.064.

[56] K. Yue, G. Trujillo-de Santiago, M. M. Alvarez, A. Tamayol, N. Annabi, and A. Khademhosseini, "Synthesis, properties, and biomedical applications of gelatin methacryloyl (GelMA) hydrogels," Biomaterials, vol. 73, pp. 254-271, 2015/12/01/ 2015, doi: https://doi.org/10.1016/j.biomaterials.2015.08.045.

[57] B. Lv et al., "Recent advances in GelMA hydrogel transplantation for musculoskeletal disorders and related disease treatment," (in eng), no. 1838-7640 (Electronic), 2015.

[58] J. Ramón-Azcón et al., "Gelatin methacrylate as a promising hydrogel for 3D microscale organization and proliferation of dielectrophoretically patterned cells," Lab on a Chip, 10.1039/C2LC40213K vol. 12, no. 16, pp. 2959-2969, 2012, doi: 10.1039/C2LC40213K.

[59] S. Ghosh, N. Kumar, and S. Chattopadhyay, "Electrically conductive “SMART” hydrogels for on-demand drug delivery," Asian Journal of Pharmaceutical Sciences, vol. 20, no. 1, p. 101007, 2025/02/01/ 2025, doi: https://doi.org/10.1016/j.ajps.2024.101007.

[60] I. Y. Kuo and B. E. Ehrlich, "Signaling in muscle contraction," (in eng), no. 1943-0264 (Electronic), 2015.

[61] M. X. Li and P. M. Hwang, "Structure and function of cardiac troponin C (TNNC1): Implications for heart failure, cardiomyopathies, and troponin modulating drugs," (in eng), no. 1879-0038 (Electronic), 2015.

[62] M. W. Berchtold, H. Brinkmeier, and M. Müntener, "Calcium Ion in Skeletal Muscle: Its Crucial Role for Muscle Function, Plasticity, and Disease," Physiological Reviews, vol. 80, no. 3, pp. 1215-1265, 2000, doi: 10.1152/physrev.2000.80.3.1215.

[63] B. Lu et al., "Pure PEDOT:PSS hydrogels," Nature Communications, vol. 10, no. 1, p. 1043, 2019/03/05 2019, doi: 10.1038/s41467-019-09003-5.

[64] X. Zhang, W. Yang, H. Zhang, M. Xie, and X. Duan, "PEDOT:PSS: From conductive polymers to sensors," Nanotechnology and Precision Engineering, vol. 4, no. 4, 2021, doi: 10.1063/10.0006866.

[65] A. Pisciotta et al., "PEDOT: PSS promotes neurogenic commitment of neural crest-derived stem cells," (in eng), no. 1664-042X (Print), 2022.

[66] K. A.-O. Roshanbinfar et al., "Electrically Conductive Collagen-PEDOT:PSS Hydrogel Prevents Post-Infarct Cardiac Arrhythmia and Supports hiPSC-Cardiomyocyte Function," (in eng), no. 1521-4095 (Electronic), 2024.

[67] S. B. Rauer et al., "Porous PEDOT:PSS Particles and their Application as Tunable Cell Culture Substrate," Advanced Materials Technologies, vol. 7, no. 1, p. 2100836, 2022, doi: https://doi.org/10.1002/admt.202100836.

[68] H. Baniasadi, A. R. SA, and S. Mashayekhan, "Fabrication and characterization of conductive chitosan/gelatin-based scaffolds for nerve tissue engineering," International journal of biological macromolecules, vol. 74, pp. 360-366, 2015.

[69] C. E. Nweke and J. A.-O. Stegemann, "Modular microcarrier technologies for cell-based bone regeneration," (in eng), no. 2050-7518 (Electronic), 2020.

[70] M. Yu et al., "Microfluidics for Formulation and Scale-Up Production of Nanoparticles for Biopharma Industry," in Microfluidics in Pharmaceutical Sciences: Formulation, Drug Delivery, Screening, and Diagnostics, D. A. Lamprou and E. Weaver Eds. Cham: Springer Nature Switzerland, 2024, pp. 395-420.

[71] S.-Y. Teh, R. Lin, L.-H. Hung, and A. P. Lee, "Droplet microfluidics," Lab on a Chip, vol. 8, no. 2, pp. 198-220, 2008.

[72] Y.-C. Tan, K. Hettiarachchi, M. Siu, Y.-R. Pan, and A. P. Lee, "Controlled Microfluidic Encapsulation of Cells, Proteins, and Microbeads in Lipid Vesicles," Journal of the American Chemical Society, vol. 128, no. 17, pp. 5656-5658, 2006/05/01 2006, doi: 10.1021/ja056641h.

[73] F. He et al., "Designable Polymeric Microparticles from Droplet Microfluidics for Controlled Drug Release," Advanced Materials Technologies, vol. 4, no. 6, p. 1800687, 2019, doi: https://doi.org/10.1002/admt.201800687.

[74] M. Gajendiran et al., "Conductive biomaterials for tissue engineering applications," Journal of Industrial and Engineering Chemistry, vol. 51, pp. 12-26, 2017/07/25/ 2017, doi: https://doi.org/10.1016/j.jiec.2017.02.031.

[75] H. Kaji, T. Ishibashi, K. Nagamine, M. Kanzaki, and M. Nishizawa, "Electrically induced contraction of C2C12 myotubes cultured on a porous membrane-based substrate with muscle tissue-like stiffness," Biomaterials, vol. 31, no. 27, pp. 6981-6986, 2010/09/01/ 2010, doi: https://doi.org/10.1016/j.biomaterials.2010.05.071.

[76] J. Anjali, V. K. Jose, and J.-M. Lee, "Carbon-based hydrogels: synthesis and their recent energy applications," Journal of Materials Chemistry A, 10.1039/C9TA02525A vol. 7, no. 26, pp. 15491-15518, 2019, doi: 10.1039/C9TA02525A.

[77] S. Ahadian et al., "Hybrid hydrogel-aligned carbon nanotube scaffolds to enhance cardiac differentiation of embryoid bodies," Acta biomaterialia, vol. 31, pp. 134-143, 2016.

[78] M. Mohamadali, S. Irani, M. Soleimani, and S. Hosseinzadeh, "PANi/PAN copolymer as scaffolds for the muscle cell-like differentiation of mesenchymal stem cells," Polymers for Advanced Technologies, vol. 28, no. 9, pp. 1078-1087, 2017.

[79] L. Tung, N. Sliz, and M. R. Mulligan, "Influence of electrical axis of stimulation on excitation of cardiac muscle cells," Circulation research, vol. 69, no. 3, pp. 722-730, 1991.

[80] S. W. Crowder et al., "Poly (ε-caprolactone)–carbon nanotube composite scaffolds for enhanced cardiac differentiation of human mesenchymal stem cells," Nanomedicine, vol. 8, no. 11, pp. 1763-1776, 2013.

[81] M. A. Khan, E. Cantù, S. Tonello, M. Serpelloni, N. F. Lopomo, and E. Sardini, "A Review on Biomaterials for 3D Conductive Scaffolds for Stimulating and Monitoring Cellular Activities," Applied Sciences, vol. 9, no. 5, p. 961, 2019.

[82] R. Dong, X. Zhao, B. Guo, and P. X. Ma, "Self-healing conductive injectable hydrogels with antibacterial activity as cell delivery carrier for cardiac cell therapy," ACS applied materials & interfaces, vol. 8, no. 27, pp. 17138-17150, 2016.

[83] X. Zhao, R. Dong, B. Guo, and P. X. Ma, "Dopamine-incorporated dual bioactive electroactive shape memory polyurethane elastomers with physiological shape

recovery temperature, high stretchability, and enhanced C2C12 myogenic differentiation," ACS applied materials & interfaces, vol. 9, no. 35, pp. 29595-29611, 2017.

[84] M. Xie, L. Wang, B. Guo, Z. Wang, Y. E. Chen, and P. X. Ma, "Ductile electroactive biodegradable hyperbranched polylactide copolymers enhancing myoblast differentiation," Biomaterials, vol. 71, pp. 158-167, 2015.

[85] J. Ren et al., "Superaligned carbon nanotubes guide oriented cell growth and promote electrophysiological homogeneity for synthetic cardiac tissues," Advanced Materials, vol. 29, no. 44, p. 1702713, 2017.

[86] L. Wang et al., "Mussel-inspired conductive cryogel as cardiac tissue patch to repair myocardial infarction by migration of conductive nanoparticles," Advanced Functional Materials, vol. 26, no. 24, pp. 4293-4305, 2016.

[87] R. Breukers et al., "Creating conductive structures for cell growth: Growth and alignment of myogenic cell types on polythiophenes," Journal of Biomedical Materials Research Part A, vol. 95, no. 1, pp. 256-268, 2010.

[88] S. Ahadian et al., "Hydrogels containing metallic glass sub-micron wires for regulating skeletal muscle cell behaviour," Biomaterials science, vol. 3, no. 11, pp. 1449-1458, 2015.

[89] L. Zhang, M. Ma, J. Li, K. Qiao, Y. Xie, and Y. Zheng, "Stimuli-responsive microcarriers and their application in tissue repair: A review of magnetic and electroactive microcarrier," Bioactive Materials, vol. 39, pp. 147-162, 2024/09/01/ 2024, doi: https://doi.org/10.1016/j.bioactmat.2024.05.018.

[90] B. S. Spearman et al., "Conductive interpenetrating networks of polypyrrole and polycaprolactone encourage electrophysiological development of cardiac cells," Acta biomaterialia, vol. 28, pp. 109-120, 2015.

[91] C. E. Schmidt, V. R. Shastri, J. P. Vacanti, and R. Langer, "Stimulation of neurite outgrowth using an electrically conducting polymer," Proceedings of the National Academy of Sciences, vol. 94, no. 17, pp. 8948-8953, 1997.

[92] S. Wang et al., "3D culture of neural stem cells within conductive PEDOT layer-assembled chitosan/gelatin scaffolds for neural tissue engineering," Materials Science and Engineering: C, vol. 93, pp. 890-901, 2018.

[93] S. Wang et al., "Neural stem cell proliferation and differentiation in the conductive PEDOT-HA/Cs/Gel scaffold for neural tissue engineering," Biomaterials science, vol. 5, no. 10, pp. 2024-2034, 2017.

[94] Y. Zhang, H. Chen, and J. Li, "Recent advances on gelatin methacrylate hydrogels with controlled microstructures for tissue engineering," International Journal of Biological Macromolecules, vol. 221, pp. 91-107, 2022/11/30/ 2022, doi: https://doi.org/10.1016/j.ijbiomac.2022.08.171.

[95] Z. Xuan et al., "Tailoring Hydrogel Composition and Stiffness to Control Smooth Muscle Cell Differentiation in Bioprinted Constructs," Tissue Engineering and

Regenerative Medicine, vol. 20, no. 2, pp. 199-212, 2023/04/01 2023, doi: 10.1007/s13770-022-00500-1.

[96] F. L. Ronzoni et al., "Myoblast 3D bioprinting to burst in vitro skeletal muscle differentiation," Journal of Tissue Engineering and Regenerative Medicine, vol. 16, no. 5, pp. 484-495, 2022/05/01 2022, doi: https://doi.org/10.1002/term.3293.

[97] I. Noshadi et al., "Engineering Biodegradable and Biocompatible Bio-ionic Liquid Conjugated Hydrogels with Tunable Conductivity and Mechanical Properties," Scientific Reports, vol. 7, no. 1, p. 4345, 2017/06/28 2017, doi: 10.1038/s41598-017-04280-w.

[98] S. Koç and M. Gümüşderelioğlu, "Versatile cell cultivation on injectable poly(butylene adipate-co-terephthalate) microcarriers: Impact of surface properties across different cell types," Journal of Biomedical Materials Research Part B: Applied Biomaterials, vol. 112, no. 9, p. e35464, 2024, doi: https://doi.org/10.1002/jbm.b.35464.

[99] P. S. Zammit, T. A. Partridge, and Z. Yablonka-Reuveni, "The Skeletal Muscle Satellite Cell: The Stem Cell That Came in From the Cold," Journal of Histochemistry & Cytochemistry, vol. 54, no. 11, pp. 1177-1191, 2006, doi: 10.1369/jhc.6R6995.2006.

[100] A. A.-O. Nguyen, P. L. Goering, R. K. Elespuru, S. Sarkar Das, and R. J. Narayan, "The Photoinitiator Lithium Phenyl (2,4,6-Trimethylbenzoyl) Phosphinate with Exposure to 405 nm Light Is Cytotoxic to Mammalian Cells but Not Mutagenic in Bacterial Reverse Mutation Assays. LID - 10.3390/polym12071489 [doi] LID - 1489," (in eng), no. 2073-4360 (Electronic), 2020.

[101] W. Szczęsna-Górniak et al., "Physicochemical Features and Applicability of Newly Fabricated Phytopharmaceutical-Loaded Hydrogel Alginate Microcarriers with Viscoelastic Polyelectrolyte Coatings," ChemPhysChem, vol. 25, no. 4, p. e202300758, 2024, doi: https://doi.org/10.1002/cphc.202300758.

[102] Y. Wang et al., "3D bioprinting of conductive hydrogel for enhanced myogenic differentiation," Regenerative Biomaterials, vol. 8, no. 5, 2021, doi: 10.1093/rb/rbab035.

[103] F. Tan, X. Li, X. Li, M. Xu, K. A. Shahzad, and L. Hou, "GelMA/PEDOT:PSS Composite Conductive Hydrogel-Based Generation and Protection of Cochlear Hair Cells through Multiple Signaling Pathways," Biomolecules, vol. 14, no. 1, p. 95, 2024.

[104] E. Mostafavi, D. Medina-Cruz, K. Kalantari, A. Taymoori, P. Soltantabar, and T. J. Webster, "Electroconductive Nanobiomaterials for Tissue Engineering and Regenerative Medicine," (in eng), no. 2576-3113 (Electronic), 2020.

[105] V. K. Rao et al., "G9a promotes proliferation and inhibits cell cycle exit during myogenic differentiation," Nucleic Acids Research, vol. 44, no. 17, pp. 8129-8143, 2016, doi: 10.1093/nar/gkw483.

[106] Y. Nihashi et al., "Distinct cell proliferation, myogenic differentiation, and gene expression in skeletal muscle myoblasts of layer and broiler chickens," Scientific Reports, vol. 9, no. 1, p. 16527, 2019/11/11 2019, doi: 10.1038/s41598-019-52946-4.

[107] T. M. Watanabe, K. Higuchi S Fau - Kawauchi, Y. Kawauchi K Fau - Tsukasaki, T. Tsukasaki Y Fau - Ichimura, H. Ichimura T Fau - Fujita, and H. Fujita, "Chromatin plasticity as a differentiation index during muscle differentiation of C2C12 myoblasts," (in eng), no. 1090-2104 (Electronic), 2012.

[108] Y. C. Shin et al., "Stimulating effect of graphene oxide on myogenesis of C2C12 myoblasts on RGD peptide-decorated PLGA nanofiber matrices," Journal of Biological Engineering, vol. 9, no. 1, p. 22, 2015/11/25 2015, doi: 10.1186/s13036-015-0020-1.

[109] Y. Chen et al., "Large-Scale Cell Production Based on GMP-Grade Dissolvable Porous Microcarriers. LID - 10.3791/65469 [doi]," (in eng), no. 1940-087X (Electronic), 2023.

[110] A. S. Khalil, R. Jaenisch, and D. J. Mooney, "Engineered tissues and strategies to overcome challenges in drug development," (in eng), no. 1872-8294 (Electronic), 2020.

[111] B. G. Widell A Fau - Hansson, E. Hansson Bg Fau - Nordenfelt, and E. Nordenfelt, "A microcarrier cell culture system for large scale production of hepatitis A virus," (in eng), no. 0166-0934 (Print), 1984.

[112] B. P. Dodson and A. D. Levine, "Challenges in the translation and commercialization of cell therapies," (in eng), no. 1472-6750 (Electronic), 2015.

[113] Y. S. Kim, M. M. Smoak, A. J. Melchiorri, and A. G. Mikos, "An Overview of the Tissue Engineering Market in the United States from 2011 to 2018," (in eng), no. 1937-335X (Electronic), 2019.

[114] N. Pangarkar, A. Pharoah M Fau - Nigam, D. W. Nigam A Fau - Hutmacher, S. Hutmacher Dw Fau - Champ, and S. Champ, "Advanced Tissue Sciences Inc.: learning from the past, a case study for regenerative medicine," (in eng), no. 1746-076X (Electronic), 2010.

[115] Y. Ikada, "Challenges in tissue engineering," (in eng), no. 1742-5689 (Print), 2006.

[116] A. Saberi, F. Jabbari, P. A.-O. Zarrintaj, M. A.-O. Saeb, and M. A.-O. X. Mozafari, "Electrically Conductive Materials: Opportunities and Challenges in Tissue Engineering. LID - 10.3390/biom9090448 [doi] LID - 448," (in eng), no. 2218-273X (Electronic), 2019.

[117] M. Ghovvati et al., "Harnessing the Power of Electroconductive Polymers for Breakthroughs in Tissue Engineering and Regenerative Medicine," Materials Chemistry Horizons, vol. 2, no. 3, pp. 195-206, 2023, doi: 10.22128/mch.2023.693.1042.

[118] A. Casella, A. Panitch, and J. K. Leach, "Endogenous Electric Signaling as a Blueprint for Conductive Materials in Tissue Engineering," (in eng), no. 2576-3113 (Electronic), 2021.

[119] R. Arambula-Maldonado and K. Mequanint, "Carbon-based electrically conductive materials for bone repair and regeneration," Materials Advances, 10.1039/D2MA00001F vol. 3, no. 13, pp. 5186-5206, 2022, doi: 10.1039/D2MA00001F.

[120] P. Alizadeh et al., "Use of electroconductive biomaterials for engineering tissues by 3D printing and 3D bioprinting," Essays in Biochemistry, vol. 65, no. 3, pp. 441-466, 2021, doi: 10.1042/ebc20210003.

[121] S. Por Hajrezaei, M. Haghbin Nazarpak, S. Hojjati Emami, and E. Shahryari, "Biocompatible and Electroconductive Nanocomposite Scaffolds with Improved Piezoelectric Response for Bone Tissue Engineering," International Journal of Polymer Science, vol. 2022, no. 1, p. 4521937, 2022, doi: https://doi.org/10.1155/2022/4521937.

[122] P. Sikorski, "Electroconductive scaffolds for tissue engineering applications," Biomaterials Science, 10.1039/D0BM01176B vol. 8, no. 20, pp. 5583-5588, 2020, doi: 10.1039/D0BM01176B.

[123] Z. J. Rogers, M. P. Zeevi, R. Koppes, and S. A. Bencherif, "Electroconductive Hydrogels for Tissue Engineering: Current Status and Future Perspectives," (in eng), no. 2576-3113 (Electronic), 2020.

[124] Y. Shi et al., "Gold Nanomaterials and Bone/Cartilage Tissue Engineering: Biomedical Applications and Molecular Mechanisms," (in English), Frontiers in Chemistry, Mini Review vol. 9, 2021-July-09 2021, doi: 10.3389/fchem.2021.724188.

[125] A. Gupta and S. Singh, "Multimodal Potentials of Gold Nanoparticles for Bone Tissue Engineering and Regenerative Medicine: Avenues and Prospects," Small, vol. 18, no. 29, p. 2201462, 2022, doi: https://doi.org/10.1002/smll.202201462.

[126] A. Hasan, M. Morshed, A. Memic, S. Hassan, T. J. Webster, and H. E. Marei, "Nanoparticles in tissue engineering: applications, challenges and prospects," (in eng), no. 1178-2013 (Electronic), 2018.

[127] G. Kandhola et al., "Nanomaterial-Based Scaffolds for Tissue Engineering Applications: A Review on Graphene, Carbon Nanotubes and Nanocellulose," (in eng), no. 2212-5469 (Electronic), 2023.

[128] R. Abbasi, G. Shineh, M. Mobaraki, S. Doughty, and L. A.-O. Tayebi, "Structural parameters of nanoparticles affecting their toxicity for biomedical applications: a review," (in eng), no. 1388-0764 (Print), 2023.

[129] C. Ning, Z. Zhou, G. Tan, Y. Zhu, and C. Mao, "Electroactive polymers for tissue regeneration: Developments and perspectives," (in eng), no. 0079-6700 (Print), 2018.

[130] I. Rocha, G. Cerqueira, F. Varella Penteado, and S. I. Córdoba de Torresi, "Electrical Stimulation and Conductive Polymers as a Powerful Toolbox for Tailoring Cell Behaviour in vitro," (in eng), no. 2673-3129 (Electronic), 2021.

[131] M. A. Marsudi et al., "Conductive Polymeric-Based Electroactive Scaffolds for Tissue Engineering Applications: Current Progress and Challenges from Biomaterials and Manufacturing Perspectives," International Journal of Molecular Sciences, vol. 22, no. 21, p. 11543, 2021.

[132] E. Dashtimoghadam, F. Fahimipour, N. Tongas, and L. Tayebi, "Microfluidic fabrication of microcarriers with sequential delivery of VEGF and BMP-2 for bone regeneration," Scientific Reports, vol. 10, no. 1, p. 11764, 2020/07/16 2020, doi: 10.1038/s41598-020-68221-w.

[133] F. Kamar et al., "A simple, cost-effective microfluidic device using a 3D cross-flow T-junction for producing decellularized extracellular matrix-derived microcarriers," bioRxiv, p. 2024.10.30.621138, 2024, doi: 10.1101/2024.10.30.621138.

[134] Z. Wang et al., "A controllable gelatin-based microcarriers fabrication system for the whole procedures of MSCs amplification and tissue engineering," (in eng), no. 2056-3418 (Print), 2023.

[135] M. Lu et al., "Microfluidic Hydrodynamic Focusing for Synthesis of Nanomaterials," (in eng), no. 1748-0132 (Print), 2016.

[136] C. Siltanen et al., "Microfluidic fabrication of bioactive microgels for rapid formation and enhanced differentiation of stem cell spheroids," (in eng), no. 1878-7568 (Electronic), 2016.

[137] A. I. Van Den Bulcke, B. Bogdanov, N. De Rooze, E. H. Schacht, M. Cornelissen, and H. Berghmans, "Structural and Rheological Properties of Methacrylamide Modified Gelatin Hydrogels," Biomacromolecules, vol. 1, no. 1, pp. 31-38, 2000/03/14 2000, doi: 10.1021/bm990017d.

[138] W. Lowrie, Fundamentals of Geophysics. Cambridge University Press, 2007.

[139] S. Gruber and A. Nickel, "Toxic or not toxic? The specifications of the standard ISO 10993-5 are not explicit enough to yield comparable results in the cytotoxicity assessment of an identical medical device," (in eng), no. 2673-3129 (Electronic), 2023.

[140] H. S. Ghazali, E. Askari, A. Seyfoori, and S. M. Naghib, "A high-absorbance water-soluble photoinitiator nanoparticle for hydrogel 3D printing: synthesis, characterization and in vitro cytotoxicity study," Scientific Reports, Article vol. 13, no. 1, 2023, Art no. 8577, doi: 10.1038/s41598-023-35865-3.

[141] G. Kaklamani, D. Kazaryan, J. Bowen, F. Iacovella, S. H. Anastasiadis, and G. Deligeorgis, "On the electrical conductivity of alginate hydrogels," (in eng), no. 2056-3418 (Print), 2018.

[142] O. A.-O. Kangasmaa, I. Laakso, and G. Schmid, "Estimating Human Fat and Muscle Conductivity From 100 Hz to 1 MHz Using Measurements and Modelling," (in eng), no. 1521-186X (Electronic), 2025.

[143] J. H. Lee et al., "In vivo electrical conductivity measurement of muscle, cartilage, and peripheral nerve around knee joint using MR-electrical properties tomography," Scientific Reports, vol. 12, no. 1, p. 73, 2022/01/07 2022, doi: 10.1038/s41598-021-03928-y.

[144] M. Kitzmann, G. Carnac, M. Vandromme, M. Primig, N. J. C. Lamb, and A. Fernandez, "The Muscle Regulatory Factors MyoD and Myf-5 Undergo Distinct Cell Cycle–specific Expression in Muscle Cells," Journal of Cell Biology, vol. 142, no. 6, pp. 1447-1459, 1998, doi: 10.1083/jcb.142.6.1447.

[145] L. M. André, C. R. M. Ausems, D. G. Wansink, and B. Wieringa, "Abnormalities in Skeletal Muscle Myogenesis, Growth, and Regeneration in Myotonic Dystrophy," (in English), Frontiers in Neurology, Review vol. 9, 2018-May-28 2018, doi: 10.3389/fneur.2018.00368.

[146] V. Flamini, R. S. Ghadiali, P. Antczak, A. Rothwell, J. E. Turnbull, and A. Pisconti, "The Satellite Cell Niche Regulates the Balance between Myoblast Differentiation and Self-Renewal via p53," (in eng), no. 2213-6711 (Electronic), 2018.

[147] F. Girardi et al., "TGFβ signaling curbs cell fusion and muscle regeneration," (in eng), no. 2041-1723 (Electronic), 2021.

[148] S. Ahadian et al., "Electrical stimulation as a biomimicry tool for regulating muscle cell behavior," Organogenesis, vol. 9, no. 2, pp. 87-92, 2013/04/01 2013, doi: 10.4161/org.25121.

[149] T. Tanaka et al., "Alignment of Skeletal Muscle Cells Cultured in Collagen Gel by Mechanical and Electrical Stimulation," International Journal of Tissue Engineering, vol. 2014, no. 1, p. 621529, 2014, doi: https://doi.org/10.1155/2014/621529.

Software citations

[1] GraphPad Software. GraphPad Prism Version 7.0; GraphPad Software: San Diego, CA, USA, 2016. Available online: https://www.graphpad.com (accessed on November 18, 2024).

[2] Schneider, C.A., Rasband, W.S., & Eliceiri, K.W. (2012). "NIH Image to ImageJ: 25 years of image analysis." Nature Methods, 9(7), 671-675. DOI: 10.1038/nmeth.2089

[3] All figures created with BioRender.com. (Student plan)

[4] Dassault Systèmes. SolidWorks [Computer software]. Version 2025 SP0. University of Victoria academic license. Waltham, MA: Dassault Systèmes, 2025 SP0.

[5] BD Biosciences. (2012). FlowJo (Version X.0) [Computer software]. https://www.flowjo.com